ABSTRACT

Title of Thesis: FLOW INDUCED CAVITY RESONANCE FOR TURBULENT COMPRESSIBLE MIXING ENHANCEMENT IN SCRAMJETS

Degree Candidate: Vijay Anand Raghavendran Nenmeni

Degree and year: Master of Science, 2002

Thesis directed by: Associate Professor Dr. Kenneth H. Yu
Department of Aerospace Engineering

In a Scramjet combustor, flow residence time is very short and fuel-air mixing can be adversely affected by compressibility effect. Thus, it is important to study mixing enhancement techniques for reducing the characteristic mixing time. It is also important to examine the feasibility of using them in practical settings. One of the promising mixing enhancement techniques is based on flow-induced cavity resonance, which generates large-scale coherent structures in the shear layer for faster mixing. Of particular interest is whether this technique, which is passive in nature, can be used over a wide range of flow conditions, expected in Scramjet operation. In this thesis, physical mechanisms governing the use of flow-induced cavity resonance were examined experimentally using Schlieren visualization of the flowfield and spectral analysis of resulting pressure oscillations. Various cavities with the length between 0.125 and 1.25 inch and the depth between 0.125 and 0.25 inch were placed inside a Mach 2 flow tunnel, which simulated the Scramjet internal flowfield. The properties of supersonic flow were further modified in the inlet, upstream of the cavity section, by changing the upstream stagnation pressure between 35 psig and 120 psig, which resulted in inlet shock trains of different strength. The objective was to characterize and compare the enhancement mechanism under various off-design conditions. In all, nine different cavity cases were tested under six different stagnation pressure settings. For each case, spark Schlieren images were taken and pressure oscillations inside the cavity were measured. The Schlieren images provided qualitative understanding of the physics while the pressure measurements were used to quantify the amplitude and frequency of dominant oscillations. Also from the images, inlet Mach number was deduced by measuring the Mach wave angles. The data were summarized to shed more light on reliability of the mixing enhancement mechanism under off-design inlet conditions. The results indicated that flow-induced cavity resonance mechanism was robust over a wide range of flow conditions. Also, mode-switching behavior of the cavities was observed, which could modify the mixing enhancement rate. Further, helium injection studies were conducted to gain qualitative assessment of the effect of cavity resonance on mixing.

FLOW INDUCED CAVITY RESONANCE FOR TURBULENT COMPRESSIBLE MIXING ENHANCEMENT IN SCRAMJETS

By

Vijay Anand Raghavendran Nenmeni

Thesis submitted to the Faculty of the Graduate School of the
University of Maryland, College Park in partial fulfillment
of the requirements for the degree of
Master of Science
2002

Advisory Committee:

Dr. Kenneth Yu, Associate Professor, Advisor
Dr. James Baeder, Associate Professor
Dr. Mark Lewis, Professor

ACKNOWLEDGEMENTS

At the outset, I would like to thank my advisor, Dr. Kenneth Yu, for his support and guidance through out my stay here as a Graduate student and also for his inputs into the writing of this thesis. I am also thankful to the other committee members, Dr. Mark Lewis and Dr. James Baeder for agreeing to be on my thesis committee and for their cooperation and guidance.

I would also like to acknowledge the support and encouragement of the various faculty members and staff of the department. Special thanks to Dr. Steve Buckley, Dr. Jewel Barlow and our department Graduate Director, Dr. Mary Bowden for their guidance at various stages of my graduate study. The interaction and support of my fellow graduate students has made my graduate study a rich educational experience. I would like to thank all my friends who have been supportive and who have helped me, supported me and motivated me in my thesis work and in my stay here. Though they are numerous to explicitly mention here, I am indebted to Manikandan, Jayakumar, Paramita and Dipan for being with me through thick and thin.

Finally, I would like to dedicate my thesis to my family and my best friend, Senthil, who have been a source of constant support and motivation through out my life. I owe to them everything that I am and I hope to be.

TABLE OF CONTENTS

LIST OF FIGURES

LIST OF TABLES

TABLE OF NOMENCLATURE

u_c	Convective velocity of shear layer structures.
u_1	Velocity of the faster stream.
u_2	Velocity of the slower stream.
H	Inlet height of the duct.
L_m	Mixing length.
D_{FA}	Molecular diffisivity.
r	Velocity ratio.
Δu	Velocity differential.
x	Downstream distance.
M_{c1}	Convective Mach number with respect to the first stream.
M_{c2}	Convective Mach number with respect to the second stream.
a_1	Speed of sound in the first stream.
a_2	Speed of sound in the second stream.
s	Density ratio.
C_δ	Shear layer growth rate parameter.
L	Length of the cavity.
D	Depth of the cavity.
W	Width of the cavity.
L/D	Aspect ratio of the cavity.
f_m	Instability wave frequency.
U_∞	Freestream velocity.
C_p	Phase speed of disturbances.
C_∞	Freestream speed of sound.
M_∞	Freestream Mach number.
T	Fundamental time period of oscillations.
St_∞	Strouhal number.
m	Empirical constant in Rossiter’s formula.
P_o	Stagnation pressure of air entering test section.
T_o	Stagnation temperature of air entering test section.
L_1	First collimating lens in the Schlieren apparatus.
F_1	Focal length of the first lens.
L_2	Second lens in the Schlieren apparatus.
F_2	Focal length of the second lens.
L0D0	Baseline case.
L2D1	Shallow cavity with aspect ratio of 2.
L3D1	Shallow cavity with aspect ratio of 3.
L4D1	Shallow cavity with aspect ratio of 4.
L5D1	Shallow cavity with aspect ratio of 5.
L4D2	Deep cavity with aspect ratio of 2.
L6D2	Deep cavity with aspect ratio of 3.
L8D2	Deep cavity with aspect ratio of 4.
L10D2	Deep cavity with aspect ratio of 5.
Re_x	Local Reynolds number.
SPL	Sound pressure level.

TABLE OF NOMENCLATURE (contd.)

P	Dynamic pressure.
f_{exp}	Experimental frequency.
M	Mach number estimates from wave angle.
T_2	Temperature in the duct.
U	Velocity calculated from Mach number.
m	Oscillation mode.
f_{pred}	Predicted frequency.

Greek Symbols:

Φ	Equivalence ratio.
τ_{mixing}	Fluid mechanical mixing time.
τ_{chem}	Chemical reaction time.
δ, δ_m	Shear layer transverse thickness.
ν	Kinematic viscosity.
μ	Absolute viscosity.
ρ	Density of fluid.
ρ_1	Density of the first stream.
ρ_1	Density of the second stream.
δ_m	Vorticity thickness.
κ	Ratio of convective Mach number to freestream Mach number.
τ_{conv}	Convection time of the disturbance in the shear layer.
$\tau_{acoustic}$	Time for the acoustic wave to travel upstream inside the cavity.
$\tau_{phasedelay}$	Phase delay associated the acoustic processes.
α	Empirical constant in Rossiter’s formula.
λ	Wavelength of disturbance.
θ	Angle of the pressure wave with the cavity leading edge.

1. Introduction

1.1. Background and motivation.

For more than four decades, Scramjet engines have been regarded as the engine of choice for hypersonic air breathing propulsion systems, both for high-speed cruise missiles and for single stage to orbit (SSTO) systems (Swithenbank et al. [41]). Though the pioneering work of Ferri ([18],[19]) very much defined the problems associated with supersonic combustion (Curran et al. [8]), the presence of mixed supersonic-subsonic flowfields, along with shock-shear layer interactions and compressibility effects have made the issue of supersonic combustion one of the most enigmatic, yet challenging pursuits (Curran [9]). Among other issues, the key component identified in the development of such an engine has been the combustor design, where the fuel-air mixture is expected to coalesce, mix at both the macro and micro levels and burn efficiently, all at supersonic speeds. At these high Mach numbers, molecular level mixing of fuel and air becomes retarded due to the stabilizing influence of compressibility on the turbulent mixing layer (Seiner et al. [35]). This becomes particularly troublesome with a small-size Scramjet, where the skin friction drag becomes a substantial part of the total drag. Thus, an efficient device is required to enhance the turbulent mixing at the high Mach numbers of interest so as to maximize combustion efficiency and thrust while minimizing weight and length of the combustor (Burnes et al. [6]). An appropriately sized cavity placed inside the combustor has been seen to produce coherent structures or vortices due to flow-induced resonance of the shear layer spanning the cavity. As it will be discussed in the next section, these large scale coherent structures are very important for entrainment and macro-level mixing (Gutmark et al. [21]).

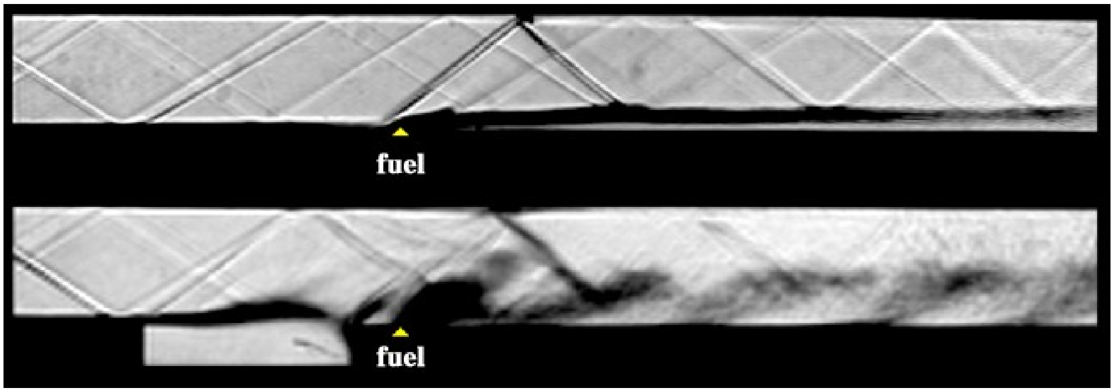

Figure 1. Schlieren images of simulated fuel injection in a supersonic airflow with and without cavity.

Figure 1 from Burnes et al. [6] shows the increase in mixing efficiency due to a combustor wall cavity placed in a Mach 2.0 airstream, when simulated fuel, namely Helium, is injected in the wake of the cavity. By comparing the figures with and without the cavity, it can seen that there is a marked increase in the spreading rate of the Helium simulated fuel jet into the supersonic crossflow when coherent structures are shed from the cavity. The resonance mechanism by which these coherent structures are formed in this highly compressible flow will be discussed in detail in the next section.

In addition, certain cavities have been proposed for flameholding in Scramjets due to the large recirculating zones and relatively lower pressure drop associated with these cavities (Burnes et al. [6], Mathur & Billig [26]). Thus an integrated flameholder-fuel injection scheme has been proposed in a Scramjet engine to improve the combustion efficiency and thus reduce combustor lengths and weight (Gruber et al. [20], Ben-Yakar & Hanson [1]). In this study, the effect of variations in inflow conditions on flow-induced resonance characteristics of cavities is analyzed. The stagnation pressure upstream was varied, which simulated the conditions that the combustor would experience in actual flight at different altitudes. Also, the robustness of the cavity resonance mechanism was analyzed under off-design conditions. Finally, a qualitative study of the effect of helium injection in the wake of the cavity was studied. The rest of this section would be devoted to gain an understanding of the problems associated with Supersonic combustion systems. The next section is a review of past work in the area of compressible mixing layer/shear layer studies and a brief review mixing augmentation techniques that have been adopted. Also, an understanding of the cavity acoustics and the pertinent models is attempted.

1.1.1. Ramjet and Scramjet combustion.

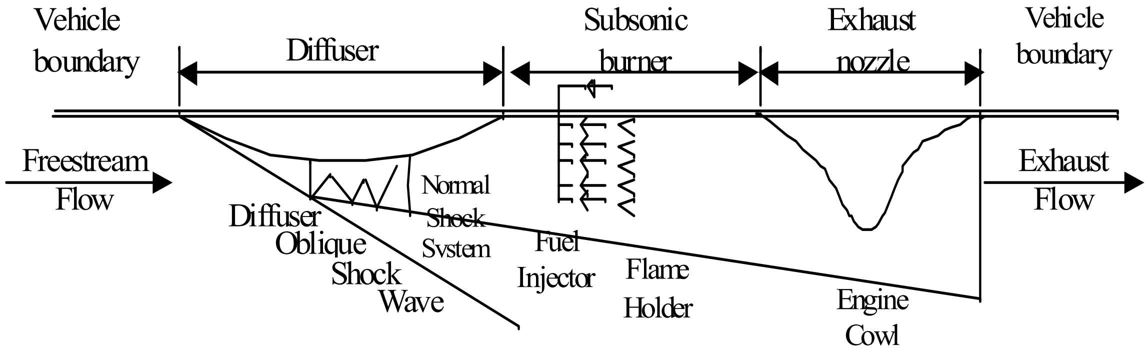

Figure 2. Schematic of two-dimensional or planar geometry Ramjet engine. (Heiser et al. [7])

A conventional Ramjet engine, as shown in Figure 2, usually operates in a flight regime of Mach 3-6. Here, the incoming airflow is compressed to subsonic speeds by a series of oblique shocks followed by a normal shock wave and further decelerated by a diverging diffuser. Fuel, which is then injected in the burner, mixes and burns, and the resulting high-pressure exhaust is led through a converging-diverging nozzle so that the resulting flow is supersonic. Thrust is thus generated as a momentum difference between the air inflow and the high-energy exhaust (Heiser et al. [23]).

When the flight Mach number increases beyond Mach 6, it becomes infeasible to decelerate the flow to subsonic speeds due to excessive performance losses due to the normal shock system, excessive stagnation pressures and temperatures, and thrust loss due to dissociation of the exhaust products due to excessive temperatures (Murthy & Curran [28], Ben-Yakar & Hanson [2]). Thus the complex phenomenon of supersonic combustion was sought for flight regimes in the range of Mach 6 - 20, where the flow is slowed down in the diffuser, but essentially maintained supersonic, avoiding the normal shock system.

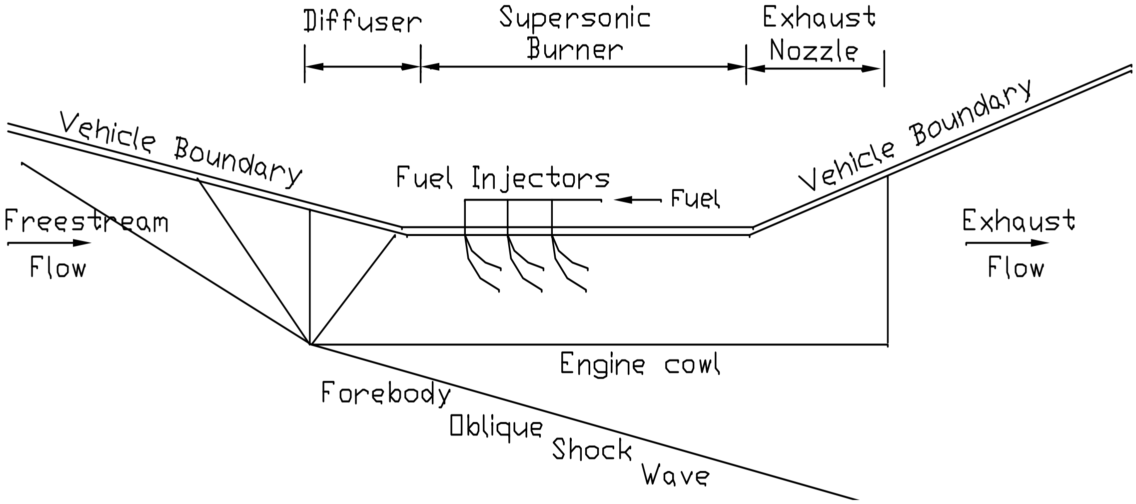

Figure 3. Schematic of two-dimensional or planar geometry Scramjet engine. (Heiser et al. [23])

Figure 3 shows the schematic of a two-dimensional Scramjet geometry that would be integrated with the underside of the vehicle; so as to minimize the external drag and also to maximize the captured airflow required to produce thrust (Heiser et al. [23]). From Figure 3, it can be seen that the required flow compression is achieved not only by the diffuser section, but also by the oblique shock wave from the vehicle forebody, thus reducing the length of the diffuser. Also, a convergent section is adopted for diffuser because the exit flow required is still supersonic. A diverging combustor exit section integrated with the vehicle afterbody avoids potential thermal choking after heat release occurs.

1.1.2. Supersonic combustion – key issues.

For the flight regimes of interest for the Scramjet engines, which is in the range of Mach 6-20, the combustor flow inlet Mach number is expected to be about one-third of the flight Mach number (Bogdanoff [3]). Thus, supersonic combustion/mixing studies for the Mach number of about 2-3 would be a good starting point for an understanding of the underlying problems. Hydrogen, which is usually the fuel of choice in such an application, would be injected into this supersonic airflow and has to mix and burn in minimum possible combustor lengths (Murthy & Curran [28], Tischkoff [42]). The choice of Hydrogen over hydrocarbons has been due to its higher heating value while allowing larger cooling capacity (Ferri [19], Swithenbank [41]).

For a reasonable combustor length, and for the combustor Mach number in the range discussed above, the flow residence times are extremely short, of the order of milliseconds (Drummond et al. [15]). Heat has to be added to the supersonic airstream within this short residence time. The exothermic reactions inside the combustor require that the fuel and air be initially mixed at a macro-level and then molecular level collisions are required for chemical reactions and heat release to occur (Fernando et al. [17]). Thus, the time required for heat release can be considered as a sum of the time required for complete molecular level mixing and the chemical reaction time (Swithenbank [41], Yu [52]). Thus, mathematically,

$$\tau_{HeatAddition} = \tau_{mixing} + \tau_{chem}$$

where τ_{mixing} is the fluid-mechanical molecular mixing time (Dimotakis [39]) and τ_{chem} is the chemical reaction time. The chemical reactions can be regarded to occur in two phases, the first of which is an induction phase where intermediate radicals are produced, and the second in which exothermic reactions occur (Ferri [19]). The major component of the chemical reaction time comes from the induction phase which can be associated with an ignition delay time. This in turn is stipulated by the combustion chemistry and depends on the fuel-air equivalence ratio, ϕ.

In a typical Scramjet, the static temperatures at the combustor entry are higher than 1000 K, so that spontaneous ignition is possible (Swithenbank [41]) and thus the chemical reaction times are extremely short. Then, the limiting factor in the heat addition process is the fluid mechanical mixing time. It has thus been regarded that the supersonic combustion process is largely mixing controlled (Ferri [19]) so that reduction in mixing time would be the prime factor in reduced length and weight of the combustor.

2. Theoretical & Experimental Background

2.1. Compressible mixing studies.

The following paragraph extracted from Drummond et al. [15] gives the basis for including a chapter on compressible mixing studies in this thesis.

> "*Although the geometric configuration of a Scramjet is relatively simple compared to a turbomachinery design, the flow physics associated with the simultaneous injection of fuel from multiple injector configurations, and the mixing and combustion of that fuel downstream of the injector is quite complex. For this reason many researchers have considered the more tractable problem of a spatially developing, primarily supersonic, chemically reacting mixing layer or jet that relaxes only the complexities introduced by the engine geometry. All the difficulties introduced by the fluid mechanics, combustion chemistry and interactions between these phenomena can be retained in the reacting mixing later, making it an ideal problem for the detailed study of supersonic reacting flow in a Scramjet. With a good understanding of the physics of the Scramjet internal flowfield, the designer can then return to the actual Scramjet geometry with this knowledge and apply engineering design tools that more properly account for the complex physics.*"

Thus, it would be prudent to understand the physics of the mixing process, identify the various mixing regimes and try to quantify the effect of compressibility on the mixing rate and lengths, before discussing the schemes for improving mixing, and thus combustion efficiencies. The initial physical models of the mixing process were developed for incompressible flows and later extended to include compressibility effects (Yu et al. [51]).

2.1.1. Physics of the mixing process.

As stated earlier, in a typical Scramjet combustor, the fuel-air mixture has to be mixed at a molecular level before chemical reactions can occur. Mixing is regarded as a transport of fluid properties, such as momentum, species concentration, temperature, etc between two dissimilar fluids or two streams of the same fluid with different properties when they come in contact (Dimotakis [12]). The region where the transport of the properties occurs is often termed as the "mixing layer", also often known as "shear layer", because most often fluid shear is the predominant factor. The mixing layer is characterized by flow instabilities created due to the gradients in fluid properties. Without going into the distinction between compressible or incompressible mixing layer, the mixing process can be summarized to be composed of the following regimes (Vuillermoz et al.[43], Heiser et al.[23])

Unstable laminar regime: Growth of the flow structures from the initial small perturbation and their orderly appearance.

Convective Mixing regime: The initial vortices grow and amalgamate as they are convected downstream, causing the mixing layer to spread linearly. In this stage entrainment and pairing occurs, i.e. the fluids are brought together but essentially unmixed at the molecular level. This is defined as *macro-mixing* or *stirring* or *near field mixing*.

Diffusive Mixing regime: As sufficient amount of fluids are entrained and paired into large flow structures, large-scale instabilities cause these structures to eventually break down to smaller scales, paving the way for molecular level or *micro-mixing*. This is also known as *far-field mixing*.

2.1.1.1. Parallel shear/mixing layer.

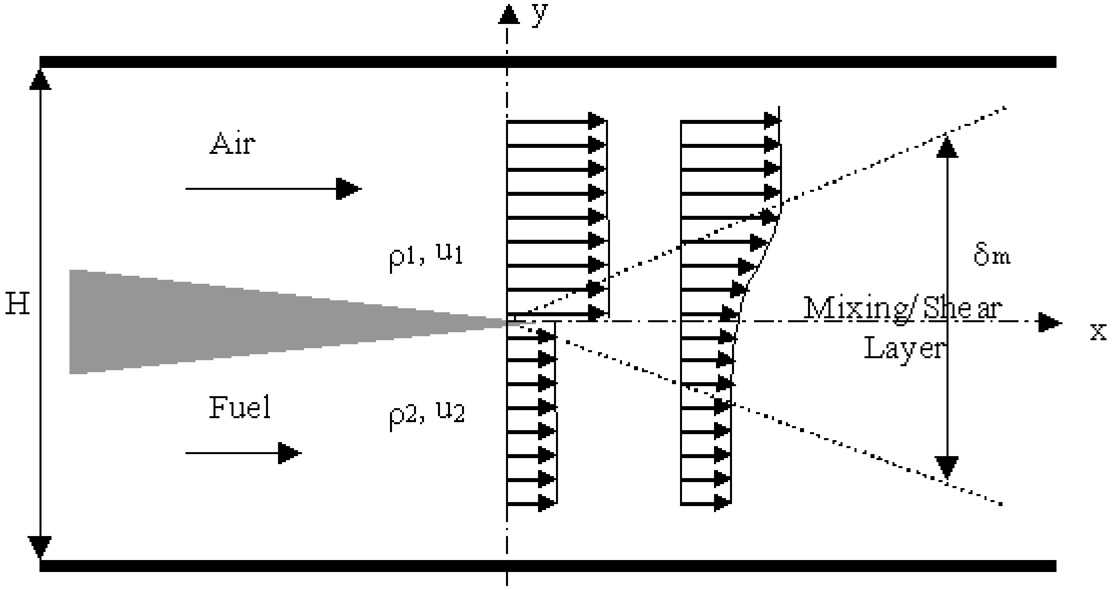

Figure 4. Mixing of parallel streams of fuel and air in a constant area duct (Heiser et al. [23])

Historically, the most convenient and efficient way of studying the mixing layer physics has been the use of a splitter plate with fluids of different properties flowing above and below the plate as shown in Figure 4 (Brown & Roshko [4], Papamoschou & Roshko [31]). Here, the two streams across the splitter plate are assumed to be air and fuel with fluid properties ρ_1, u_1 and ρ_2, u_2 respectively. Heiser et al. [23] made the distinction between different types of mixing layers based on the velocity differential between the two streams and discussed the effectiveness of mixing in each case. Before going into the distinction, it is important to point out that a *convective velocity*, u_c, to be defined in detail later, is used to non-dimensionalize the individual stream velocities. The mean velocity of the two flow streams is a rather obvious choice for the value of this convective velocity. Usually, the shear/mixing layer thickness is defined in a boundary layer sense (Dimotakis [11]).

Zero-shear mixing layer: When the velocities of the species across the splitter plate have the same velocity, i.e., $u_c = u_1 = u_2$, there is no shear between the two streams, and thus species transport occurs mainly as a result of molecular diffusion, rather than momentum flux or vorticity. The growth of mixing layer thickness, δ_m, as shown in Figure 4, is given as a function of downstream distance x as,

$$\delta_m(x) \approx 8\sqrt{\frac{D_{FA}\,x}{u_c}}$$

where D_{FA} is the molecular diffusivity of the mixture given by Fick's law of diffusion. Further, the mixing length required is given as

$$L_m = \frac{u_c H^2}{16 D_{FA}}$$

Laminar shear/mixing layer: When the velocities of the streams are changed such that $u_1 > u_2$, the shear stress caused due to the velocity differential creates flow instabilities in the mixing layer whose convective velocity is $u_c = (u_1 + u_2)/2$. It is pertinent to also define two additional quantities, namely *velocity ratio r* = u_2/u_1 and *velocity differential,* $\Delta u \equiv u_1 - u_2$. Δu in this case has a finite value in the laminar regime and thus the mixing process is rather slow, as the transport is again due to a molecular process, here that of kinematic viscosity. The mixing layer growth rate is thus given as,

$$\delta = 8\sqrt{\frac{\nu x}{u_c}}$$

where ν is the Kinematic viscosity given as $\nu = \mu / \rho$. It is seen that this growth rate is very small so as to be neglible and the mixing length required given by $L_m \approx \frac{u_c H^2}{64\nu}$ is too long for practical purposes. Thus, we need to resort to turbulent mixing layers.

Turbulent shear/mixing layer: Further increase of the *velocity differential,* Δu, induces a transition in the mixing layer from laminar flow. During this transition, the mixing layer becomes highly unstable resulting in the formation of periodic vortices that are convected downstream. This is famously known as the “Kelvin-Helmholtz instability” and the vortices shed assume the shape of rollers and were also observed by Brown & Roshko [4] in their studies and so are also known as “Brown-Roshko rollers”(Rossman [34]). The development of these flow instabilities then leads to the various mixing regimes as described in the previous subsection.

2.1.1.2. Factors affecting shear layer growth.

Shear layer growth (denoted by δ/x) is an important parameter in assessing the level of mixing achieved. δ is considered to denote the local transverse extent of the sheared region that contains the molecularly mixed fluid (Dimotakis [12]). Various research efforts have been aimed at investigating the effects of the density ratio($s=\rho_2/\rho_1$), velocity ratio ($r=u_2/u_1$: subscripts 1,2 refer to faster & slower streams respectively), velocity differential (Δu=u1-u2), compressibility effects (convective Mach number M_c), heat release, inflow conditions (boundary layer characteristics, acoustic fluctuations, etc), pressure and temperature gradients on the shear layer growth. This would be a good point to define the convective Mach number and convective velocity of the large-scale structures in the mixing layer in order to define a parameter for compressibility in the shear layer.

Convective Mach number: The discovery of large-scale structures in incompressible shear was the basis of evolving a frame of reference moving with the large-scale structures in the flow (Papamoschou & Roshko [32]). This idea was extended to compressible shear layers, as they also tend to exhibit large-scale structures. A characteristic velocity of the shear layers structures is defined, denoted as u_c, and the convective Mach numbers with reference each of the fluid streams is defined as

$$M_{c1} = \frac{u_1 - u_c}{a_1} \ \& \ M_{c2} = \frac{u_c - u_2}{a_2}$$

where a_1 and a_2 are the speeds of sound in each of the fluid streams. Describing the large-scale structures in this manner, it has been seen that there exists a stagnation point common to both the fluid streams. Thus allows us to quantify the convection velocity u_c, using the equality of stagnation pressure at this point. Thus, the convection velocity can be defined as (Papamoschou & Roshko [32]),

$$\frac{u_c}{u_1} = \frac{1 + \frac{u_2}{u_1}\sqrt{\frac{\rho_2}{\rho_1}}}{1 + \sqrt{\frac{\rho_2}{\rho_1}}}$$

For equal specific heat, γ, this expression becomes transforms into a weighed average

$$u_c = \frac{a_2 u_1 + a_1 u_2}{a_1 + a_2}$$

2.1.1.2.1. Effect of velocity differential (Δu)

For low compressibility, the time rate of shear layer growth is shown to be proportional to ΔU, and can be expressed as: $\frac{\mathrm{d}\delta}{\mathrm{dt}} \propto \Delta \mathrm{u}$ and thus the spatial shear layer growth is $\frac{d\delta}{dx} \propto \frac{\Delta u}{u_c}$ (Brown & Roshko [4]) Another parameter to account for the shear layer growth rate used in literature is in terms of vorticity thickness: $\delta_w = \Delta u / (\partial u / \partial y)_{max}$ (Brown

& Roshko[4], Dimotakis[11]). It is obvious from these relations that decrease in ΔU has a favorable effect on the shear layer growth by increasing the vortical structure.

2.1.1.2.2. Density ratio (*s*) and velocity ratio(*r*).

The velocity ratio has a direct influence on the shear layer structures, because of its influence in the creation of the coherent structures. Thus, at least for incompressible shear layers, a reduction in velocity ratio has a direct positive effect on increase in mixing. A relation that has been proposed for the effect of velocity ratio (*r*) in incompressible shear layers (Dimotakis [11])

$$\frac{\delta}{x} \approx C_{\delta} \frac{1-r}{1+r}$$

where C_{δ} is the growth rate parameter. The dependence of the shear layer growth on density variations has been extensively studied (Brown & Roshko [4], Papamoschou & Roshko [32]). It is seen that as the density ratio is increased from 0.1 to about 8, the shear layer growth rate is seen to increase significantly (Brown & Roshko [4]). An incompressible growth rate incorporating both velocity and density gradients has been proposed by Brown & Roshko [4].

$$\frac{d\delta}{dx} = C_{\delta} \frac{(1-r)(1+\sqrt{s})}{1+r\sqrt{s}}$$

The density ratio, *s* may also play a significant role in mixing in highly compressible mixing layers with pressure gradients, by the creation of baroclinic torque that arises out of misalignment of the pressure and density gradients in the flow field.

For compressible shear layers, the effect of velocity ratio would be accounted by the compressibility effects. The density effect has been accounted for in the definition above for convective velocity of shear layer structures, which is reiterated here.

$$\frac{u_c}{u_1} = \frac{1 + \frac{u_2}{u_1}\sqrt{\frac{\rho_2}{\rho_1}}}{1 + \sqrt{\frac{\rho_2}{\rho_1}}}$$

2.1.1.3. Compressibility effects.

The benchmark study by Brown & Roshko [4] showed that the effect of compressibility was uncoupled from the effects of density ratio and velocity ratio. Their experiments showed that, for the same values of *r* and *s*, the departure in mixing from the uniform density case in the supersonic mixing layer case is almost 10 orders of magnitude greater than that of the incompressible case (Dimotakis [12]). Most of the shear layer experiments have tried to quantify the compressibility effects through the convective Mach number and have regarded a normalized shear layer growth rate, which incorporates the growth rate of the compressible shear layer as a function of the incompressible growth rate. It has been observed that when the convective Mach number is increased, there is a drastic reduction in the normalized growth rate, with reductions upto 20% for Mach numbers in the range of 2.0 (Seiner et al. [35]). This can be seen in Figure 6. It has been observed that compressibility has the most severe effect on the shear layer growth rate. Though the reasons for decreased mixing efficiency for high convective Mach numbers have not been proved conclusively, one possible explanation could be that compressibility effects tend to decrease the energy available in the large-scale structures thus suppressing their growth (Dimotakis [12]).

2.2. Mixing enhancement techniques.

The need for mixing enhancement techniques at the high Mach numbers of interest arises due to the effects of compressibility as discussed in the previous section. Several excellent reviews of various mixing enhancement techniques adopted for compressible shear layers are available in literature (Seiner et al. [35], Gutmark et al. [21], Drummond et al. [15]). Most of the mixing enhancement techniques aim at excitation of the compressible shear layer to produce coherent structures discussed in the previous section (Yu et al. [51]). In addition to their application in Scramjets, these techniques are also found useful in diverse applications such as jet noise reduction, thrust augmentation ejectors, thrust vector control, metal deposition and gas dynamic lasers (Gutmark et al. [21]). Various mixing augmentation techniques have been broadly classified based on the means of excitation as passive and active techniques (Seiner et al. [35]). Passive methods aim at generating large-scale structures in the shear layer by geometric modifications in the flowfield. Excitation is achieved by any of the means such as acoustic excitation (Cavities), streamwise vorticity (Ramps, Tabs, Lobe mixers, Chevrons) or self-excited resonance (counterflow, rearward facing step) (Seiner et al. [35], Gutmark et al. [21]).

Two traditional means of fuel injection used in these methods are normal and parallel injection schemes. Figure 5 shows the schematic of a normal fuel injection into a supersonic crossflow. As the fuel jet enters the supersonic airstream, a very strong bow shock is created. This bow shock causes a significant total pressure loss, but helps in creating subsonic recirculation zones upstream of the injection point which is useful for mixing and flame holding (Ben-Yakar & Hanson [2]). Also, the normal injection of the fuel ensures sufficient penetration of the fuel into the airstream which increases the

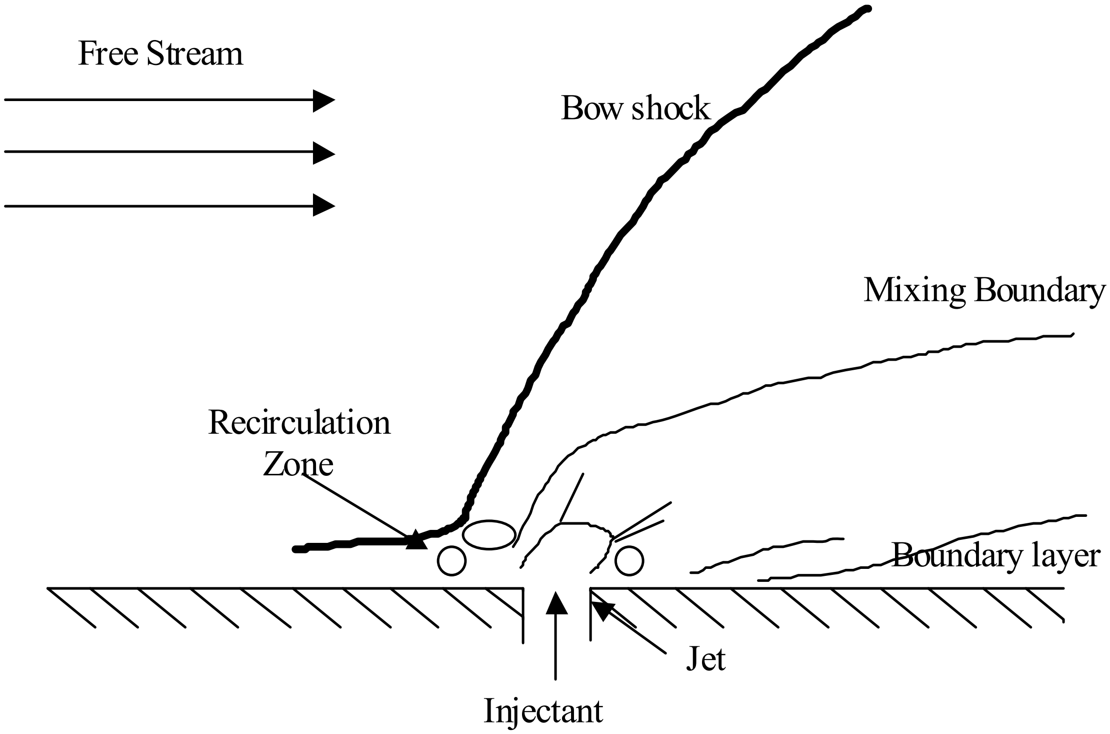

Figure 5. Schematic of transverse injection (Seiner et al [35])

interfacial contact area between the air and fuel stream, which in turn aids in entrainment and mixing (Drummond et al [16]). On the other hand, parallel or streamwise injection is governed by parallel shear layers of the type discussed in the previous section. The compressibility effect discussed has an adverse effect on parallel mixing. The advantages gained by parallel injection, such as reduced performances losses and thrust enhancement may be offset by the reduced mixing rates. But Dimotakis [12] and Drummond et al [15] suggest that parallel injection coupled with geometrical means, such as ramps and tabs, used to create axial vorticity might be effective in mixing augmentation. Such methods utilize the baroclinic vorticity produced due to misalignment of the density and pressure gradients in the flowfield to aid mixing (Seiner et al [35], Yu [52]). Other injection methods involving angled injection (Ben-Yakar & Hanson [2]) and a combination of transverse and parallel injection (Drummond et al [16]) have also been proposed.

On the other hand, Active means of mixing enhancement aim at forced excitation of shear layer structures either by mechanical means or otherwise (Seriner et al [35]). But, in the range of Reynolds number that are typically encountered in a Scramjet, the energy requirements make it infeasible to have active means of flow excitation (Yu & Schadow [51]). Thus, flow induced cavity resonance has been an efficient passive mixing enhancement method that has evolved into a prime candidate for Scramjets due to its attractive features.

2.2.1. Mixing enhancement by cavity resonance.

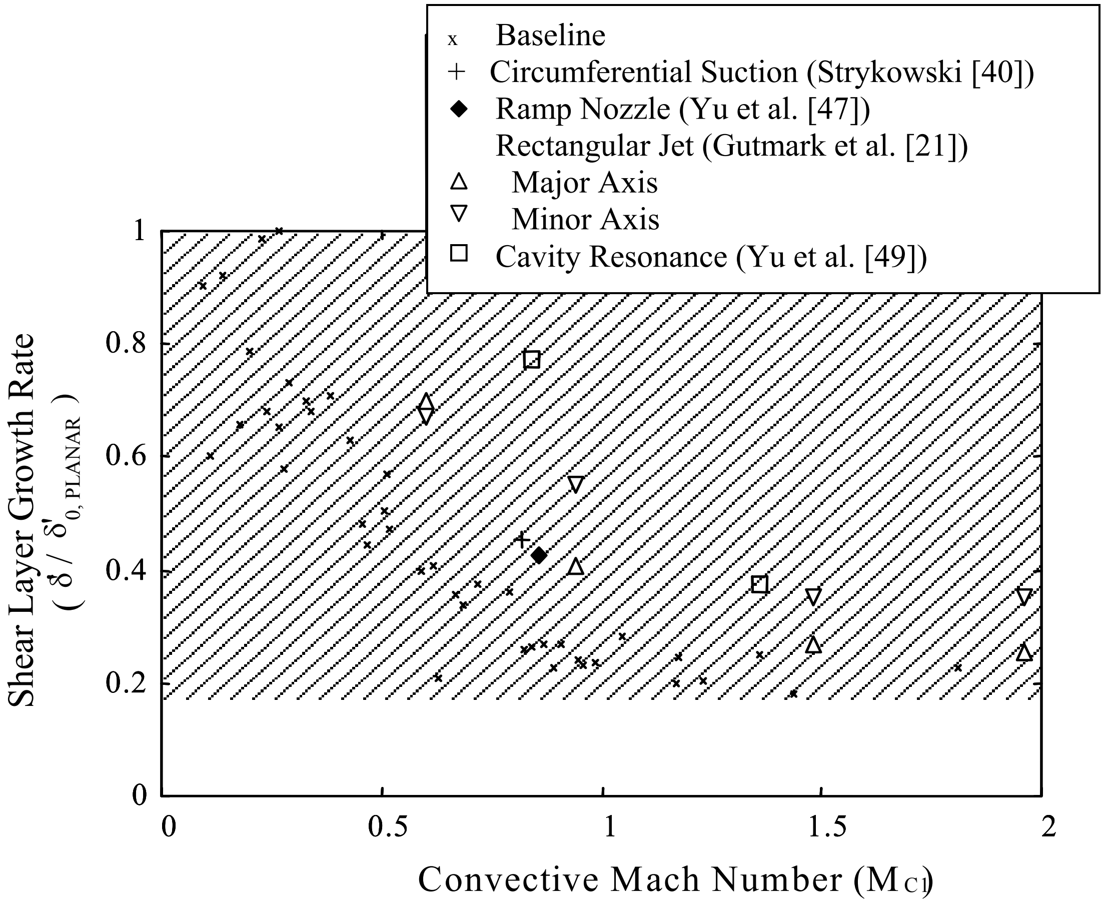

Figure 6. Effect of compressibility on shear layer growth rate (Gutmark et al. [22])

As seen in the previous section, mixing enhancement using cavities is attractive for Scramjets due to its effectiveness and relatively small pressure losses associated with cavities (Burnes et al. [6]). Figure 6 shows the influence of compressibility on the shear layer growth rate. The shear layer growth rate of the compressible shear layer normalized by the incompressible growth rate is plotted as a function of the convective Mach number of the shear layer structures. The normalized growth rate observed using various mixing enhancement techniques are plotted along with the baseline case (hatched area), showing their effectiveness in mixing. As was noted in the earlier section, for the baseline case, the shear layer growth is reduced almost to 20% of the incompressible value as the convective Mach numbers is increased to 2.0. It can be seen that the cavity induced resonance mechanism provides drastic increase in shear layer growth rate for these flow conditions, indicating that this mechanism could be used in Scramjets.

2.3. Cavity flow field characteristics:

The study of flow field in cavities has been given importance due to its relevance and importance in various aerodynamic configurations (Kegerise [25]). As mentioned earlier, combustor wall cavities have been studied by the supersonic combustion community as potential fuel-air mixing enhancement devices and also to achieve flame holding and stabilization. The flow field acoustics of cavities have been the subject of several detail studies (Ben-Yakar & Hanson [2], Heller & Bliss [24], Murray & Elliot [27], Rockwell & Naudascher [31]). The objectives of such studies have been either to encourage the instabilities associated with the shear layer over the cavity flow field in order to enhance mixing or in finding methods to suppress the cavity flow instabilities. This has been largely due to diverse applications such as gear wheel wells on commercial aircraft and weapons bay in military aircraft, where the cavities are employed to enhance in-flight performance (Rockwell & Naudascher [31]). In such cases, the instabilities of the flow over cavities are highly undesirable as they lead to increased jet noise level and significant increase in drag. The tone levels of the pressure fluctuations could be such magnitude as to affect the integrity of the nearby structural components or sensitive instrumentation. While most of these studies have been for subsonic flow over the cavity, supersonic flow over cavities has been of interest to the Scramjet community for flameholding and mixing enhancement.

***Cavity nomenclature*:**

The cavity geometry in literature has been usually parameterized with length L, depth D, width H and inlet height H in the case of confined flows. Various parameters such as length-to-depth ratio or the aspect ratio (L/D), width-to-depth (W/D) ratio, depth-to-height (D/H) ratio have been used to characterize the flow field in the cavity.

2.3.1. Shear layer characteristics over cavities:

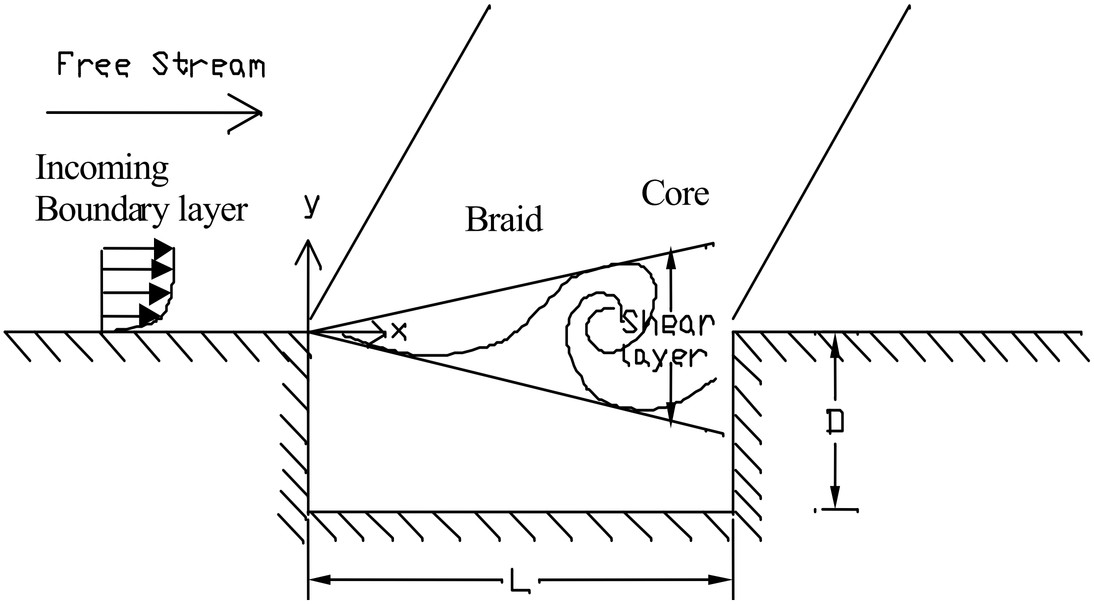

Figure 7. Cavity flow field characteristics (Murray and Elliot [27])

Figure 7 shows supersonic flow over a cavity, where the shear layer detaches from the upstream lip of the cavity, spans over the cavity, and reattaches itself somewhere downstream. The large-scale structures expected to be present in the shear layer are also shown in the figure. An expansion wave is generated at the leading edge of the cavity, while a compression wave forms at the trailing edge. Depending on the impingement location of the shear layer downstream of the leading edge, the acoustic characteristics over the cavity are modified. This allows a classification based on the aspect ratio (L/D) of the cavities.

2.3.2. Type of cavities:

The classification of cavities has been based on acoustic characteristics observed for different aspect ratios (L/D) and it depends on various factors, like the Mach number of the flow approaching the cavity, boundary layer thickness approaching the cavity, placement of the cavity (whether in confined or unconfined flow) and the width of the cavity (Rockwell & Naudascher [31]). Based on the L/D ratio, one of the basic classification has been that of "deep" and "shallow" cavities for L/D<1 and L/D>1 respectively (Ben-Yakar & Hanson [1]). The shallow cavities are further classified as "open" and "closed" based on their acoustic characteristics. Typically, open cavities have L/D < 7-10 and closed cavities have L/D >10-13. Further classifications have been proposed such as transitionally open and transitionally closed which lie between the open and closed cavities (Tracy and Plentovich [43]).

A typical acoustically open cavity flow field is characterized by a turbulent shear layer that separates at the leading edge of the cavity, spans the entire length of the cavity, and reattaches downstream of the cavity. Such a cavity often exhibits self-sustained oscillations. The mechanism for the oscillation process is triggered by the unsteady motion of the shear layer above the cavity (Ben-Yakar & Hanson [1]). The interaction of the high energy flow over the cavity, which is traveling at the convective velocity of shear layer structures, with that inside the cavity creates a pressure rise at the trailing edge of the cavity. This pressure rise creates an upstream traveling acoustic wave which travels inside the cavity at the local speed of sound. The feedback look is complete when this wave induces vortices from the leading edge of the cavity.

2.3.3. Rossiter model and it modifications.

A model developed by Rossiter [33] and later modified by Heller & Bliss [24] is used to predict the dominant frequencies of the oscillations. The model considers the two wave fields discussed earlier: 1) a downstream propagating instability wave of frequency f_m and phase speed equal to κU_∞, and 2) an upstream propagating acoustic disturbance of the same frequency and a phase speed equal to c_p. Since the flow inside the cavity is subsonic in Rossiter's [33] analysis, the phase speed of the acoustic wave propagating upstream was taken to be the freestream speed of sound. Heller et al. [24] suggested that it is required to consider the temperature difference outside and inside the cavity and replaced the phase speed with freestream speed of sound at the stagnation temperature,

$\mathrm{c_p} = \mathrm{c}_\infty \sqrt{(1+\frac{\gamma - 1}{2} M_\infty^2)}$ A mathematical treatment of the Cavity acoustics in order to derive Rossiter's model has been discussed (Yu et al. [51]). The fundamental time period of the resonance structures can be considered to be made of three parts,

$$T = \tau_{conv} + \tau_{acoustic} + \tau_{phasedelay}$$

τ_{conv} is the convection time of the disturbance created at the leading edge. This occurs at the convective Mach number of the shear layer structures.

$\tau_{acoustic}$ is the time taken for the pressure wave created at the downstream edge to travel upstream.

$\tau_{phasedelay}$ is the phase delay associated with the impingement of the shear layer on the downstream lip and the creation of the pressure waves

Thus,
$$T = \frac{L}{kU_{\infty}} + \frac{L}{c_p} + \varphi$$

Where κ represents the ratio of the convective Mach number and the freestream Mach number and ϕ is the phase delay factor. Since the time period of the oscillation is inversely proportional to the frequency, the above equation for the time period can be transformed to a frequency domain and expressed in terms of the Strouhal number as follows. Strouhal number is a dimensionless frequency term that is often used to characterize flow oscillations.

$$St_{\infty} = \frac{f_m L}{U_{\infty}} = \frac{m - \alpha}{\frac{1}{\kappa} + M_{\infty}}$$

This is the original model developed by Rossiter [33]. The modified equation of Heller et al. [24] is obtained by taking c_p to be equal to the stagnation speed of sound:

$$St_{\infty} = \frac{f_m L}{U_{\infty}} = \frac{m - \alpha}{\frac{1}{\kappa} + \frac{M_{\infty}}{\sqrt{1 + \frac{\gamma - 1}{2} M_{\infty}^2}}}$$

This equation can be used to develop an expression for the wavelength of the downstream propagating disturbance in the Rossiter model. The wavelength of the disturbance is defined as:

$$\lambda = \frac{\kappa U_\infty}{f_m}$$

Substituting the frequency, f_m, from the above equation into the expression for the wavelength yields:

$$\frac{\lambda}{L} = \frac{1}{m-\alpha}\left[1+\frac{\kappa M_\infty}{\sqrt{1+\frac{\gamma-1}{2}M_\infty^2}}\right]$$

In earlier studies (Murray & Elliot [27]), the value of κ has been either assumed to be a constant empirical value, or has been proposed to be the ratio of convective velocity of the vortical structures in the shear layer to the freestream velocity (u_c / U_e). Also, the value of α, the phase delay between the interaction of the pressure wave with the leading edge and the subsequent formation of the new shear layer structure, has been taken on the basis of curve fits and experimental data. The values of these parameters are usually taken as 0.66 and 0.25 respectively. Though the frequency and mode of oscillation can be predicted by Rossiter's modified formula, it is still difficult to determine which modes will dominate and what their amplitudes will be.

The alternative method to determine the value of κ on the basis of the convective velocity of the shear layer over the cavity leading edge is undertaken as in (Murray & Elliot [27]). As discussed earlier, the convective Mach number can be defined in the frame of reference of the large-scale structures in the shear layer as

$$M_c = \frac{(u_1 - u_c)}{a_1} = M_1(1 - \kappa_c)$$

where the convective velocity, U_c is give by

$$U_c = \frac{a_1 u_2 + a_2 u_1}{a_1 + a_2}$$

where u_1 and u_2 are the velocities of the high and low speed streams, and a_1 and a_2 are the respective speeds of sound. Rossiter [33] and Heller and Bliss [24], by their assumption that the pressure wave in the cavity travels upstream at the local speed of sound, imply that the velocity of the fluid in the cavity is negligible. Assuming the above equation for u_c to be a valid measure of the convective velocity, the value of κ, taken as the convective velocity ratio for the cavity flow can be given by

$$\kappa = \frac{1}{\frac{a_1}{a_2} + 1} = \left\{ \frac{1}{\sqrt{1 + \frac{\gamma - 1}{2} M^2}} + 1 \right\}^{-1}$$

The value of κ obtained from the above equation has been used here to compare the experimental results with the predicted results obtained using the modified Rossiter model.

3. Experimental setup and Approach

3.1. Flow facility and test setup.

High-pressure air for the supersonic studies is fed from an Atlas Copco compressor. It is a stationary, single-stage, oil-injected screw type compressor driven by an electric motor. Compressed air from the compressor is fed into a dryer that removes moisture by cooling the air to near freezing point and draining the condensate. A gas/air filter is used to remove the oil before it is fed through supply lines into the laboratory. The maximum volume flow rate achievable at the outlet of the compressor is 358 cfm. The ducted jet experiment and helium injection studies were performed in a supersonic rig designed for this purpose, to be described later.

3.1.1. Ducted jet experiments.

A 2” diameter circular pipe at the entrance of the test facility collects the air from the supply line and feeds it into the test section. An orifice meter installed in the circular pipe section was used to estimate the maximum mass flow rate achievable in the setup. The stagnation pressure of the flow was measured by placing a pressure transducer in the circular pipe section, 2 meters upstream of the nozzle throat. The inlet pipe was transitioned from a circular section to a square section 1.5 meters upstream of the nozzle throat. This was then led into a connector block, as shown in Figure 9, which connected the square section with the test setup.

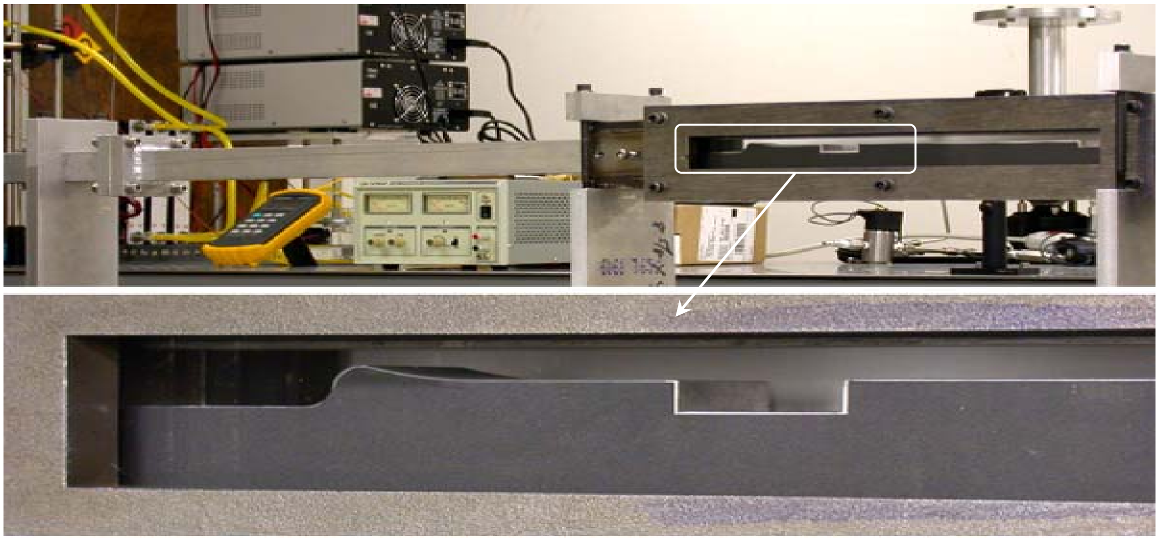

Figure 8. Picture of experimental setup (inset shows the supersonic nozzle).

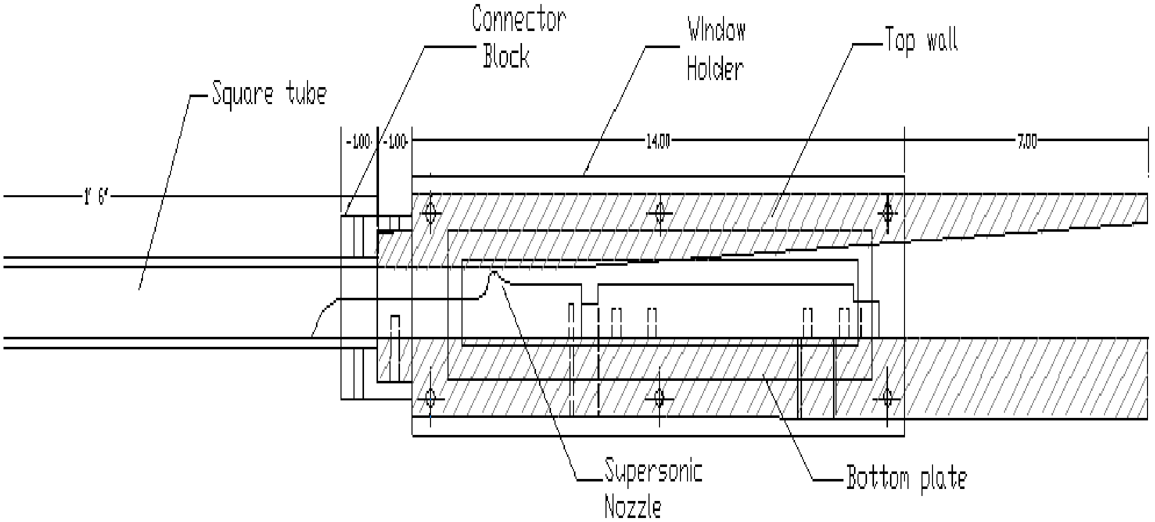

Figure 9. Detailed sketch of experimental setup.

Figure 8 shows the picture of the test section along with a blown up view of the supersonic nozzle while Figure 9 shows a sketch of the test setup. It can be seen from the figure that the top and bottom plates along with the window holders made up the four walls of the setup, while square inlet tube and the connector block acted as the upstream connections. The supersonic nozzle piece and the cavity plates were attached to the bottom plate. Most of the test section was made of stainless steel, with exceptions being the square inlet tube, the nozzle and cavity plates. Pressure sensitive adhesive backed gasket material was used in the glass-metal interfaces and also in the regions of potential leakages. Detailed sketch of each of the parts have been included here.

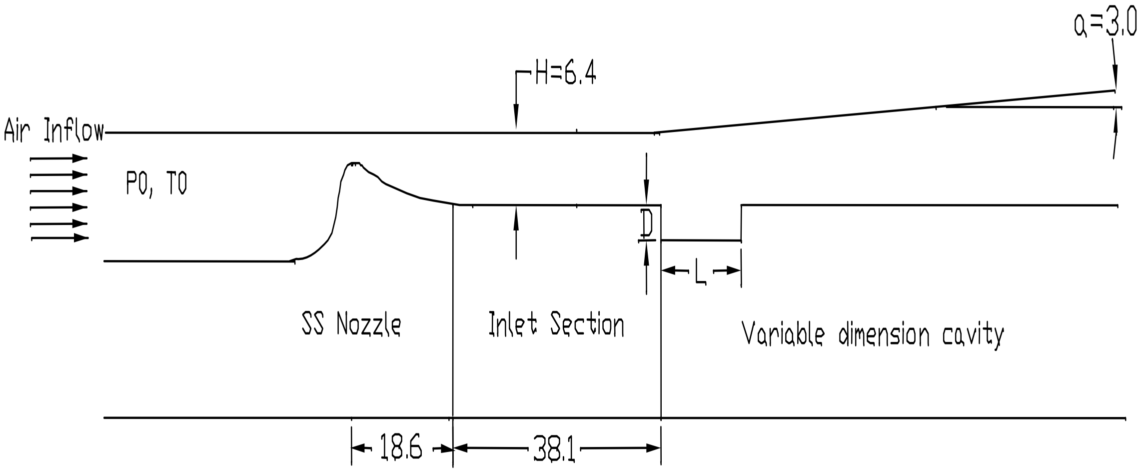

Figure 10. Detailed view of test section. (All dimensions are in mm)

Figure 10 shows a sketch of the test section portion of the overall setup depicted in Figure 9. The nomenclature for the dimensions of the cavity characteristics, namely the variable depth D, variable length L and the fixed inlet height, H, is indicated. The figure also shows that the cavity plate was separate from the nozzle piece so as to enable interchanging of various sized cavity plates. The top plate modified with a 3^0 expansion is also shown. This was done in order to prevent potential choking due to friction. Parallel airflow from the compressor is fed into the test section at a stagnation pressure P_0 and temperature T_0 as indicated. A detailed sketch of each of the parts indicated here follows.

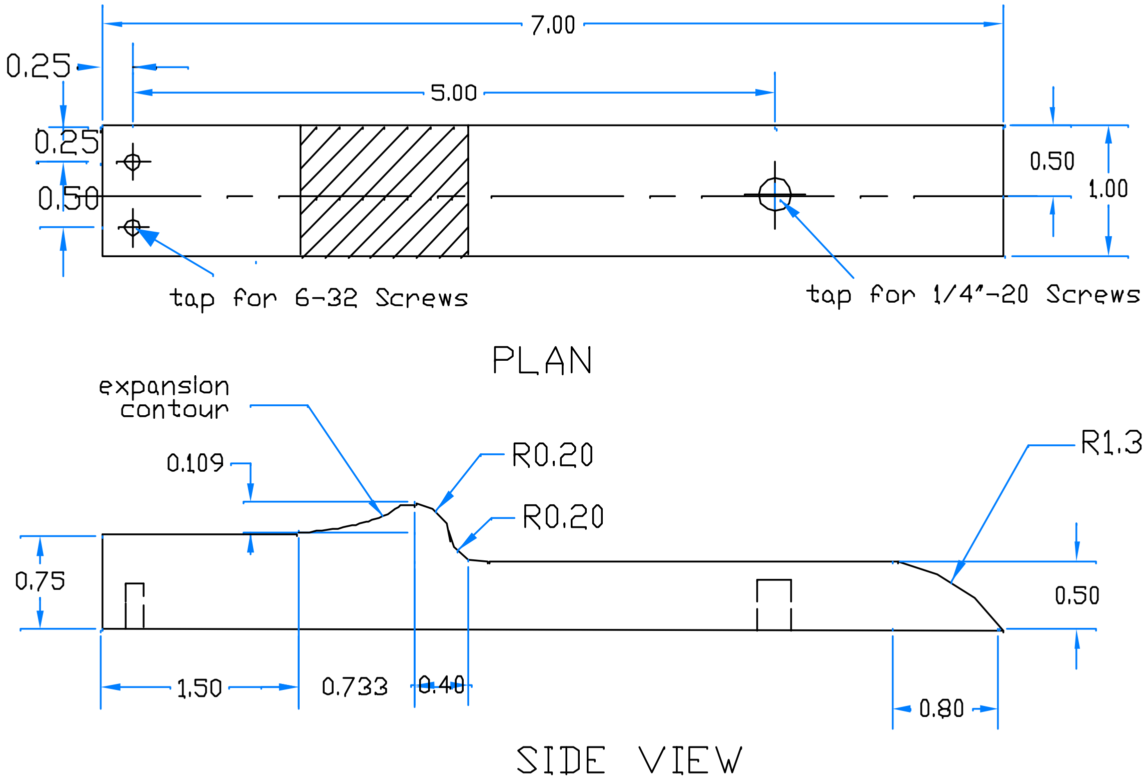

Figure 11. Supersonic nozzle (All dimensions are in inches)

A detailed picture of the 2D sharp-cornered converging-diverging nozzle used to expand the high-pressure air from the compressor to supersonic speeds has been depicted in Figure 11. The nozzle was designed for a Mach number of 2.059 at the exit, and has an aspect ratio of 4 at the exit. The nozzle was designed by adopting the Mach line contours developed in Shapiro [37]. The exit section of the nozzle piece acted as the inlet to the cavity section. The cavity plate was separated from the nozzle piece so that changing the cavity plate could modify the cavity configurations.

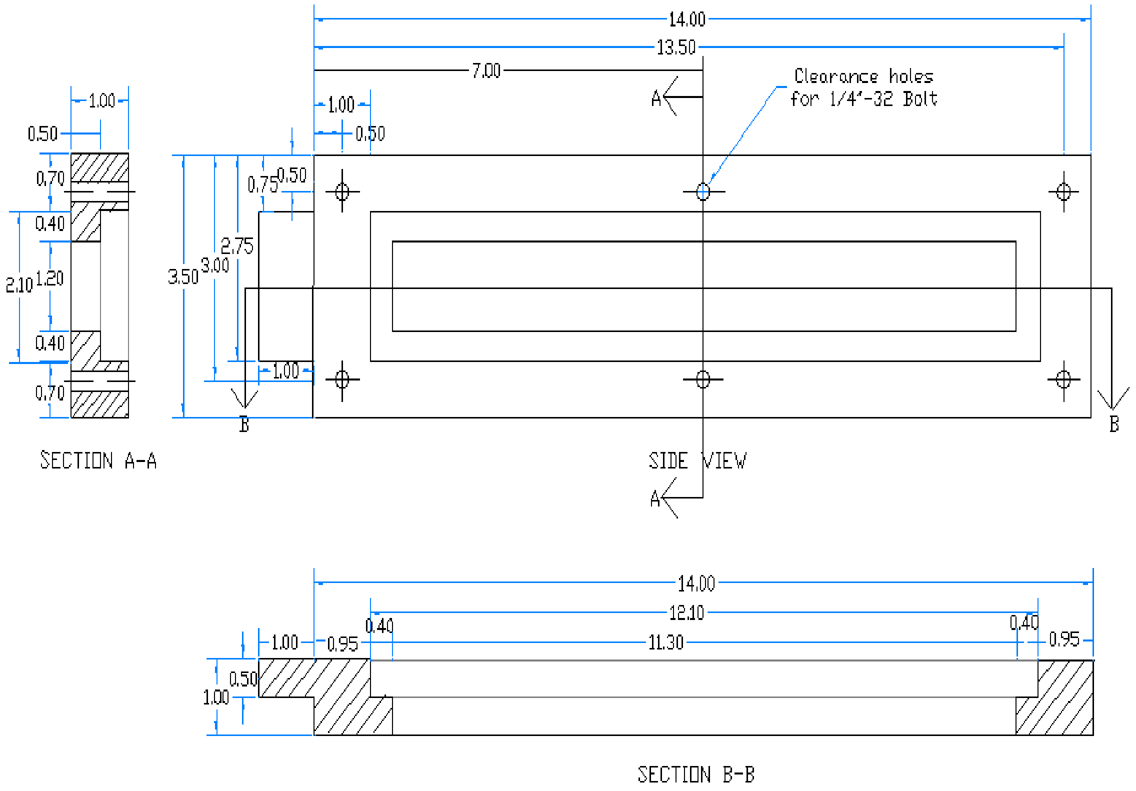

Figure 12. Window holder with optical access.

Figure 12 shows a schematic of the window holders that were provided with slots for optical visualization access. The window holders were fitted with Quartz windows to provide for optical access to the flow field to conduct flow visualization studies. Aluminium windows with ports for dynamic pressure transducers replaced the quartz windows for the pressure characterization experiments.

Figure 13 shows the top plate used in the tests. It was originally designed as a straight section made out of stainless steel, but during the course of the experiments, several changes were necessitated in the setup due to various problems such as friction choking and leakage. The top plate was replaced by an aluminium plate with a 3º expansion geometrically located at the cavity inlet in order to prevent the frictional choking effects.

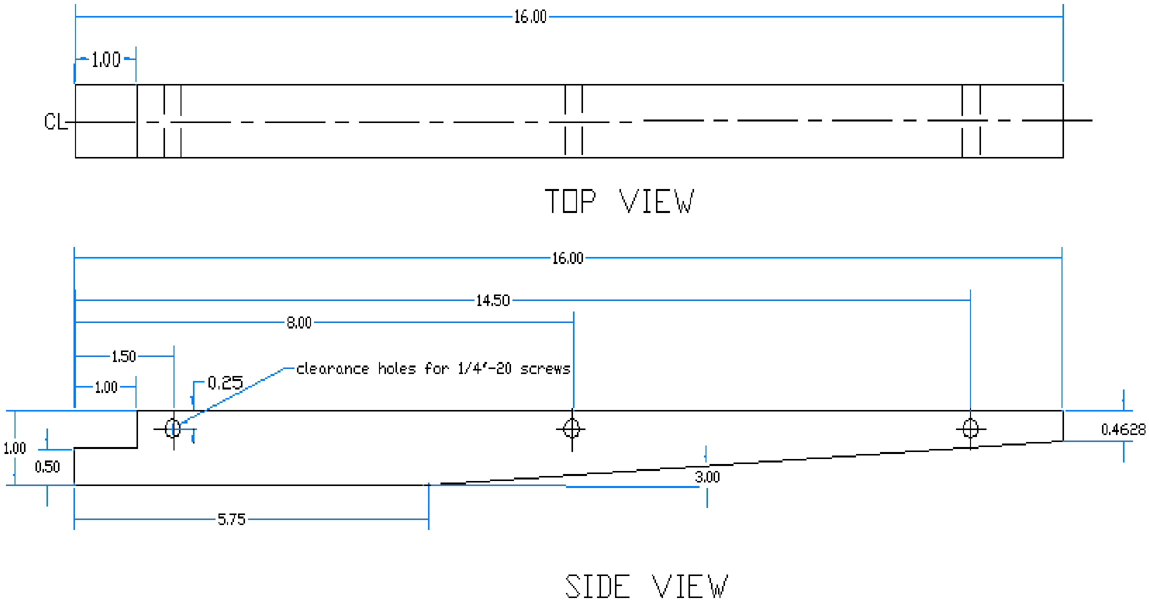

Figure 13. Top plate modified with the 3^0 expansion.

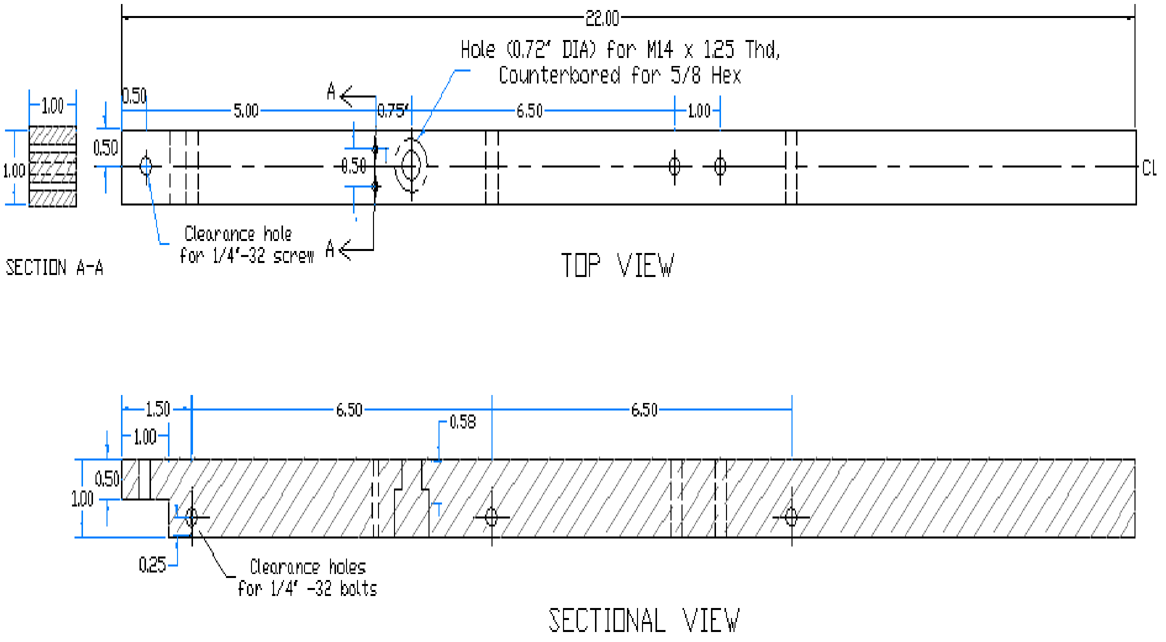

Figure 14. Bottom plate with connections for cavity section.

Figure 14 shows the bottom plate of the test setup with connections for the cavity plate. Also ports for the dynamic pressure transducer were provided and connections for the upstream. This too was made of stainless steel.

3.1.2. Helium injection experiments.

Helium from compressed bottles was used to simulate the transverse fuel injection as in a typical Scramjet combustor. The helium injection location was chosen in the wake of the cavity so as to assess the suitability of the cavity configuration for fuel-air mixing in high-speed flows. The setup was modified with the top and bottom plates of the setup being replaced by new aluminium plates. The new design was such that the cavity and nozzle sections were incorporated in the same bottom piece in order to avoid the number of joints. The drawback with this design was that the cavity configuration could not be modified and hence only the baseline case with the straight section and the L4D1 cavity were studied. An opening in the bottom plate downstream of the cavity provided the fuel injection port. A pressure regulator was used to maintain the pressure and an orifice was used to control the mass flow rate of the helium injected.

3.2. Schlieren imaging.

The Schlieren technique has been one of the most popular and oldest of optical techniques in flow visualization research (Settles [37]). The Schlieren image is created by the refraction of the light rays passing through a fluid field due to local variations of the optical path length. In a homogenous medium such as air in the ducted jet experiments, the refractive index is a function of the thermodynamic state, often only the density. Thus, this technique can be used to visualize flow fields with density variation, such as combustion flows and mixing flows. Although, Schlieren methods have traditionally been used for qualitative flow visualization, qualitative visualizations of the flow field have also been performed (Wu & Fu [39]).

3.2.1. Optics for Schlieren imaging.

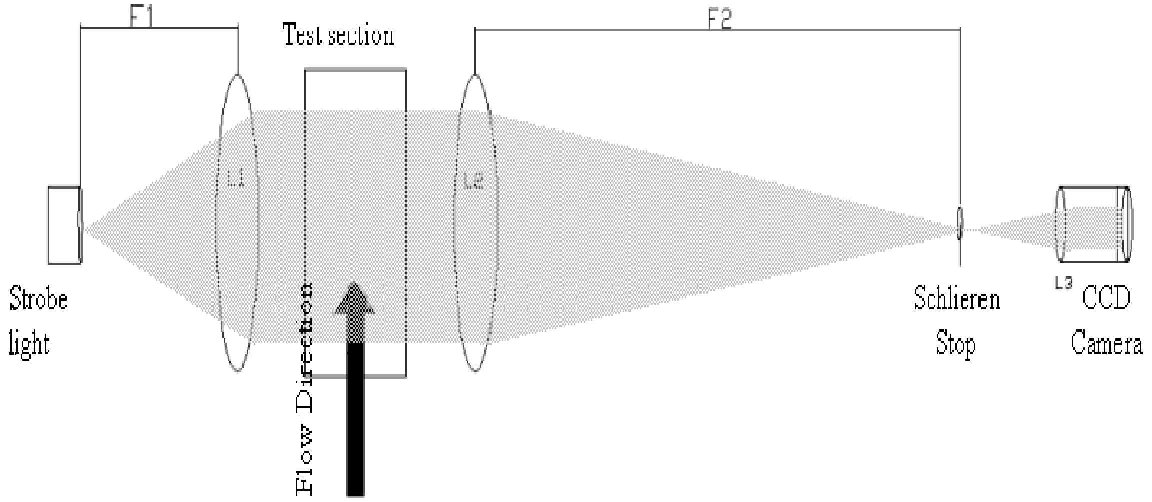

Figure 15. Schematic of the Toepler Schlieren setup.

A schematic of the optical setup used for the Schlieren imaging is given in Figure 15 above. A Digital Stroboscope from Omega, with a flash range of 30-14000 flashes per minute, was used as the light source. Since the stroboscope had two light sources, a thin perforated plate was used to block off light from one source and focus light from the other source. The stroboscope had a rotary knob, used to control the frequency of the flash. The light from the source was allowed to expand and then focused onto a collimating lens, denoted as L1, placed at a distance of 0.254 meters from the light source, which was the focal length of the lens, denoted as F1 in the figure above. The collimated beam then passed onto the test section to be visualized. A second lens, with a focal length of F2, which in this case was 1 meter, collected the beam emerging from the test section; focusing it to a point where the knife-edge would be placed, which blocked all the undeflected light. A radial Schlieren stop was used instead of a knife-edge, since the radial component of the density gradient was desired. Thus any light rays that have been refracted at the test section by a refractive index gradient caused in the flow field are no longer parallel to the optical axis of the system. These rays would then focus at a different location in the focal plane of the second lens and will thus, bypass the Schlieren stop. A 1/2" Pulnix Interline Transfer B/W CCD Camera with SC-745 shutter control was then used to collect the image. The camera has an adjustable shutter speed from 1/60 to 1/10,000 seconds. During the imaging, the frequency of the spark light source was set at 59.97 kHz to match with the frequency of the camera shutter speed. A manual variable zoom lens, denoted by L3, with a range of 12.5-75 mm was fitted onto the CCD camera to collect the images. Neutral density filters were used to adjust the brightness of the images that were visualized.

The Schlieren images obtained in the CCD camera were displayed on a 13" Diagonal Sony high-resolution Trinitron Monitor and simultaneously recorded to tape. The recorded video images were then digitized using a Data Translation frame grabber using the Global lab software. Both instantaneous and time averaged images were acquired for each run and stored on the hard disk for future reference.

3.3. Pressure measurements.

Stagnation pressure measurements were carried out upstream of the cavity section while the unsteady component of the pressure inside the cavity was measured using dynamic pressure transducers located on the side walls at the cavity section. The stagnation pressure measurements were carried out 2 meters upstream of the test section by a Setra pressure transducer flush mounted on to the circular pipe section. During the course of the experiments, in order to assess the pressure loss in the pipe, another static pressure transducer was mounted 0.25 m upstream of the test section. The pressure range of the transducer was 0 to 250 psi. The pressure measured by the transducers was displayed on a Datum 2000 digital dual channel display meter calibrated using a known signal.

The fluctuating component of the pressure signal was measured at the duct section using dynamic pressure transducers flush mounted to the walls. Initially it was planned to measure the unsteady component by a transducer mounted on the lower plate of the setup, but later the side plate mounted transducers were found to be more suitable. A Kistler 211B5 voltage mode dynamic pressure transducer with a measuring range of 0 to 100 psi and with a maximum pressure capability of 500 psi was used. A Kistler 5010B dual mode charge amplifier was used to manipulate the signal from the transducer and then it was fed into a 4 channel TDS3014B Digital Phosphor Oscilloscope that had a bandwidth of 100 MHz and a maximum sampling rate of 1.25 GHz on each channel. The fluctuating pressure signal was then transferred into a frequency domain using Fast Fourier Transform (FFT). In order to do this, a sampling rate was chosen according to the Nyquist criteria, which states that the highest frequency that can be accurately represented is less than one-half of the sampling rate. By accurate representation it is meant that there is no aliasing or distortion of the signal. Thus, the sampling rate had to be at least twice the peak frequency and for the frequency ranges of interest in the studies conducted, the sampling rate was chosen as 1 Mega samples/sec so as to cover a frequency range of 0 to 50 kHz. A typical pressure spectrum measured inside the cavity shows several intense tones superimposed on a broadband noise floor.

3.4. Experimental procedure.

3.4.1. Ducted jet experiment.

The following is a description of the various configurations studied along with the various stagnating pressure ranges. The suitability of a particular cavity to a Scramjet combustor was assessed by varying the cavity dimensions and the upstream stagnation pressure. This could be looked at as simulating the different flight regimes that could be encountered in an actual Scramjet combustor.

Cavity configurations:

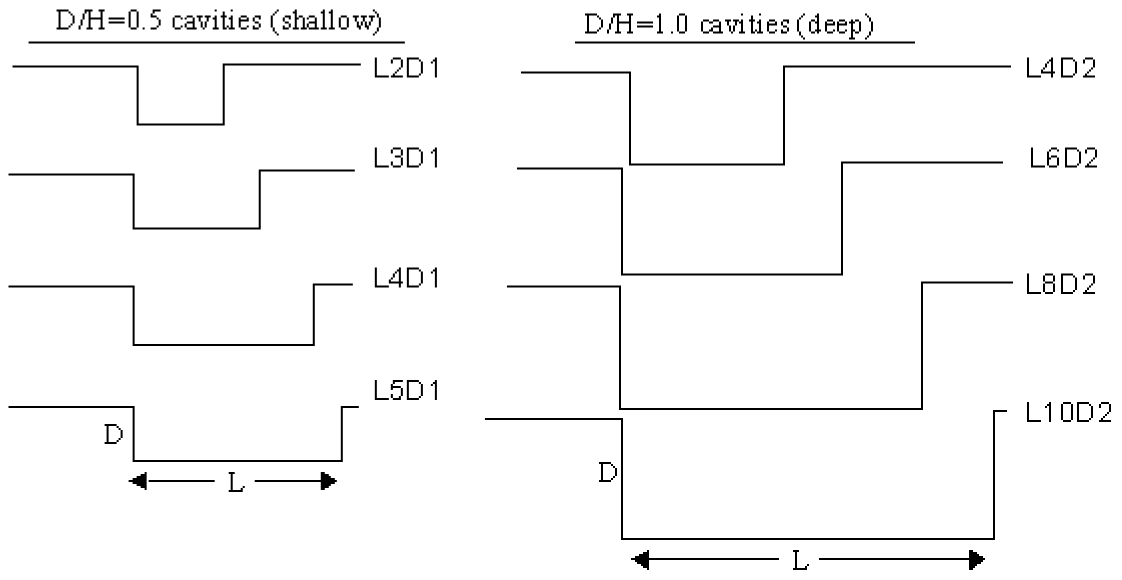

Figure 16. Cavity configurations used in the ducted jet experiments.

As the cavity plate was a separate plate downstream of the nozzle section, the cavity geometry was varied by changing the downstream cavity plate. Figure 16 shows the various cavity configurations and their designation. Nine cavity configurations were tested, beginning with the straight case with no cavity which was labeled as L0D0 and with increasing aspect ratio (L/D) of 2, 3, 4 and 5 for two normalized depths of D/H=0.5 and D/H=1.0.

Designation:

Table 1. Cavity dimensions

Cavity	L/H	D/H
L0D0	0	0
L2D1	1.0	0.5
L3D1	1.5	0.5
L4D1	2.0	0.5
L5D1	2.5	0.5
L4D2	2.0	1.0
L6D2	3.0	1.0
L8D2	4.0	1.0
L10D2	5.0	1.0

As shown in Figure 10, the inlet height H was equal to 0.25” and thus D/H=0.5 and D/H=1.0 meant that the cavity depth, D was 1/8” and 1/4” respectively. For each D/H ratio, the length of the cavity normalized by the inlet height (L/H) was varied and is tabulated in Table 1. The cavities were named according to the length and depth of the cavity normalized by the inlet height. For instance, L4D2 meant a L/H=4 and D/H=2.

Baseline case (D/H=0):

This represents the straight section without any cavity. This was used to delineate the importance of cavity configurations in mixing enhancement.

Shallow Cavities (D/H=0.5):

Four shallows cavities were studied. Cavities with aspect ratios of 2, 3, 4 and 5 were studied and are designated as L2D1, L3D1, L4D1 and L5D1 respectively.

Deep Cavities (D/H=1.0):

Four deep cavities that were studied had aspect ratios of 2, 3, 4 and 5, which were designated as L4D2, L6D2, L8D2 and L10D2 respectively.

It is to be noted here that the demarcation of these cavities as shallow and deep is with reference to the set of cavity configurations used for this study and should not be taken in a general sense. In past literature, cavities have been defined as shallow and deep on the basis of parameters such as the cavity aspect ratios (Rossiter [33]), but here the nomenclature doesn't refer to such distinctions. For the cavity configurations discussed above, both Schlieren measurements and pressure data were obtained. Exceptions were the cavity designated as L10D2 that was found inappropriate for Schlieren due to the camera limitations and the baseline case, L0D0 that produced no coherent pressure data, as it would be expected due to the absence of cavity resonance.

Procedure:

Once the Schlieren optics was set up, flow visualization studies were conducted on each of the cavity configurations. For each cavity configuration, data was obtained for each of the stagnation pressure values and changing the downstream plate varied the cavity dimensions. Once the entire set of Schlieren images had been obtained, they were digitized and studied. The stagnation pressure was measured at 2 m upstream of the nozzle throat, where the cross-sectional area of the duct was more than 20 times larger than the throat area. The effect of various inflow conditions was simulated by varying the stagnation pressure. For each of the cavity configuration discussed above, the stagnation pressure was varied from 30 psi to 120 psi. Pressure characterization studies were then carried out in a similar way for each of the cavity cases, varying the stagnation pressure and recording their FFT signal on the oscilloscope. For each run, the data was stored initially on the oscilloscope as a Microsoft Excel file and then copied onto a floppy disk and transferred to the computer.

The Mach number of the flow for various conditions was estimated on the basis of the angle that the pressure wave made with the upstream edge of the cavity. The pressure wave was considered as a weak Mach wave and the Mach number is determined from the geometry of the pressure wave from the formula $M = 1/\sin \theta$. The pressure wave becomes visible in the Schlieren Images due to the density gradient. The Schlieren pictures were studied and the Mach angles were measured for each case discussed.

3.4.2. Helium injection experiments.

The helium injection studies were carried out for two of the cavity configurations discussed. The cavity with the designation of L4D1 was chosen because of the good frequency response from the studies conducted for the ducted jet studies. Also, the baseline case with no cavity was also studied to accentuate the importance of the cavity configuration. For each of these cases, the air inflow stagnation pressure was varied from 35 psi to 115 psi and the helium injection pressure was varied from 0 psi to 115 psi.

4. Ducted Jet Experiments

The ducted jet experiments were conducted in order to analyze the flow induced resonance characteristics of cavities under various off design flight conditions. Different flight conditions encountered at varying altitudes were simulated by varying the inlet air stagnation pressure, which modified the Mach number at the cavity. It was felt that, by analyzing the cavity resonance characteristics at varying stagnation pressures, it would be possible to identify the range of frequencies that could be encountered at different altitudes, thus enabling the design of a particular cavity configuration for a Scramjet combustion system. Also, it was felt that the robustness of the cavity resonance mechanism could be put to test by varying the initial conditions. In this section, an attempt has been made to analyze the flow characteristics at both the cavity section and the supersonic nozzle upstream. An estimate of the possible boundary layer characteristics at the leading edge of the cavity has also been studied based on flat plat results. Schlieren images and unsteady pressure data have been presented.

4.1. Analysis of nozzle throat.

In order to get a qualitative idea of the flow at the nozzle throat, a few Schlieren images of the throat were captured at varying stagnation pressures and are depicted in Figure 17. It was hoped that this could be used to explain the Mach number anomalies seen at the cavity section. The figures shown here depict Schlieren images of the nozzle throat section when the upstream stagnation pressure is varied from 25 psi to 120 psi. As described earlier, the Mach number was deduced from the angle that the pressure wave makes with the horizontal.

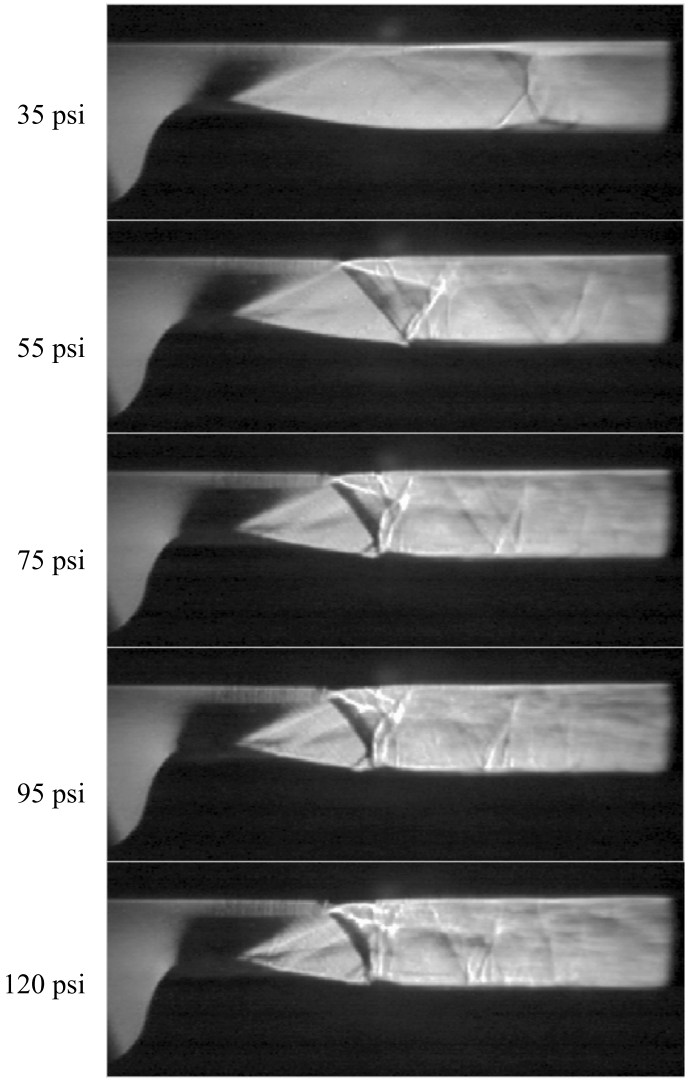

Figure 17. Supersonic nozzle at various upstream stagnation pressures.

It can be seen from the figure that, at a stagnation pressure of 35 psi, the Mach number is close to the design Mach number of 2.0. The flow is largely uniform and the boundary layer is tripped at the place where the first expansion wave strikes the top plate of the test section. Also, it can be seen that an almost normal shock is created in the section downstream of the nozzle throat. As the upstream stagnation pressure was further increased, it was found that this shock, which was in fact a multiple shock, increased in strength and continually moved upstream. For the cases with stagnation pressures of 95 and 120 psi, the shock stood close to the nozzle throat, creating near subsonic flow downstream of the shock. This was interesting, because it would be expected that the shock be washed down as the upstream stagnation pressure is increased. A possible explanation for this could be that the pressure ratio is modified through the increase in the boundary layer thickness that causes the reversal in trend. This will investigated in more detail in the next few sections. Further downstream, the flow accelerated back to supersonic just prior to the cavity section. The reasons for this could be the pressure changes due to the boundary layer characteristics, the 3^0 expansion provided to the top plate or flow expansion due to the presence of the cavity. The flow at the test section was thus supersonic with a Mach number different from the design Mach number due to these flow conditions.

4.2. Analysis of flow in the duct.

In this section, it is attempted to present an analysis of flow in the duct where cold flow studies without any helium injection were conducted. Initially, an estimate of the possible boundary layer conditions at the leading edge of the cavities is attempted. Then, Schlieren results of the cavity configurations at various stagnation pressures are presented and analyzed. Also, unsteady pressure spectra collected from the dynamic pressure transducers are presented. Further, a comparison of experimental results with the classical results is attempted.

4.2.1. Boundary layer characteristics.

In order to analyze the characteristics of the flow in the cavity configuration and to explain the anomalies in the Mach numbers, it would be useful to get an estimate of the possible boundary layer characteristics at the leading edge on the cavity.

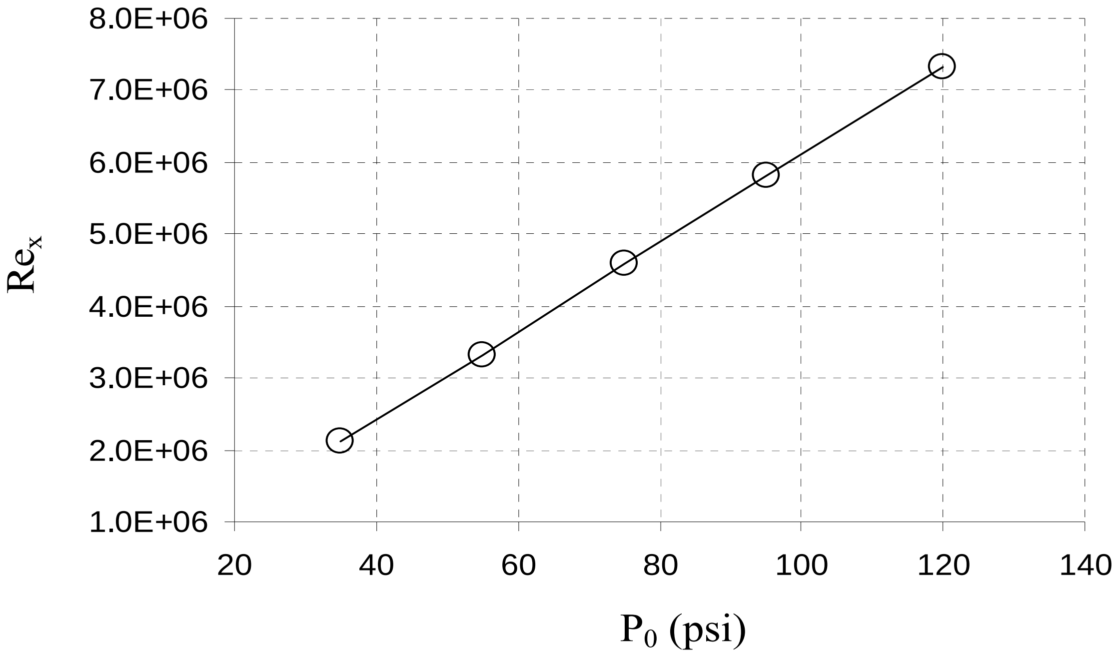

Figure 18. Estimated Reynolds number at the cavity inlet.

Figure 18 shows the plot of the estimated Reynolds number at the cavity leading edge as a function of the upstream stagnation pressures. For the Reynolds number estimate, the length dimension was taken as the inlet length from the nozzle throat to the cavity leading edge, which was about 56 mm. The velocity was calculated based on the Mach number estimate at the leading edge of the cavity. It can be seen from Figure 18 that the Reynolds number of the flow increases linearly with the increase in the stagnation pressure for the flow conditions used and the value of the Reynolds number ranges roughly from 1 million to 6 million. Usually, transition from laminar to turbulent boundary layer takes place at a critical Reynolds number roughly equal to 3 million (Schlichting [35]). It can be seen that some of the data points lie above this critical value and some of them below it. Thus, as the inlet stagnation pressure is increased, the cavity leading edge might have varying boundary layer conditions, varying from laminar to transitional to turbulent regimes.

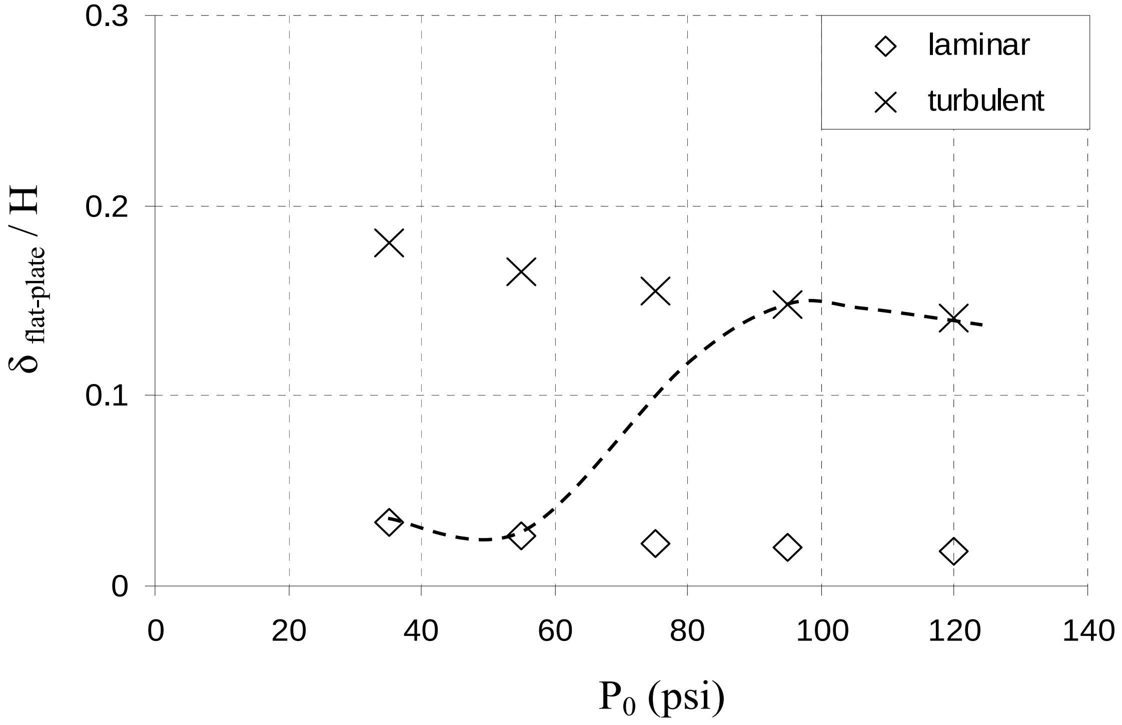

Figure 19. Estimated boundary layer thickness from flat-plate result.

Both laminar and turbulent boundary layer thickness at the leading edge of the cavity were estimated using flat plate results (Schlichting [35]). Figure 19 depicts the estimated boundary layer thickness normalized by the duct inlet height for both laminar and turbulent boundary layers at the stagnation pressures of interest. It can be seen that the boundary layer thickness decreases with the increase in stagnation pressure for either cases. But it can be observed that, when the boundary layer is turbulent, the boundary layer thickness for the flat plate result is almost 20% of the duct height, and the thickness for the rectangular test section would be twice as much, since the boundary layer would develop both on the top and bottom sides. Thus, when the boundary layer is turbulent, the boundary layer thickness could be a substantial portion of the actual duct height, thus modifying the flow conditions drastically. This could explain the decrease in the Mach number with increasing stagnation pressure as will be seen in the next section.

The curve with dashed line in Figure 19 represents a hypothetical case in which the boundary layer transitions from laminar to turbulent with increase in stagnation pressure. It can be observed that, though there is a drastic increase in the boundary layer thickness after transition occurs, it should drop once transition is complete. Thus, the Mach number should initially drop at the transition point and then rise again, which is contrary to what was observed. This can partly be explained due to the shocks that were found at the nozzle throat, which could modify these processes drastically. The analysis of the nozzle throat and the boundary layer estimations show that the flow conditions at the nozzle and the cavity were exceedingly complex and unsteady. The next few sections will show that, in spite of these flow conditions, the cavity configurations showed significant resonance characteristics.

4.2.2. Schlieren results.

Spark Schlieren images of the flow were obtained for all the stagnation pressures from 35 psi to 120 psi. The spark duration of the strobe used was of the order of 20-50 microseconds, which was not adequate to freeze the coherent structures expected in these flows. Thus, no direct evidence of these structures could be conclusively established. In spite of this limitation, some of these images are indicative of the coherent structures that were being investigated. Direct evidence of these coherent structures will be established by the frequency characterization studies, where all the cavity cases showed good frequency response. To establish the flow feature in the duct, a baseline case, in which the cavity section was replaced with a straight plate, was investigated.

4.2.2.1.Baseline Case.

In order to make a comparison of the flow behavior with and without the cavity configuration, it was decided to initially use a straight plate instead of the cavity configurations and run the setup through the range of flow conditions to determine a baseline. Figure 20 depicts the Spark Schlieren images obtained for this baseline case for increasing stagnation pressures from 35 psi to 120 psi. A strong pressure wave becomes visible at the joint of the inlet plate and the downstream plate due to a possible mismatch

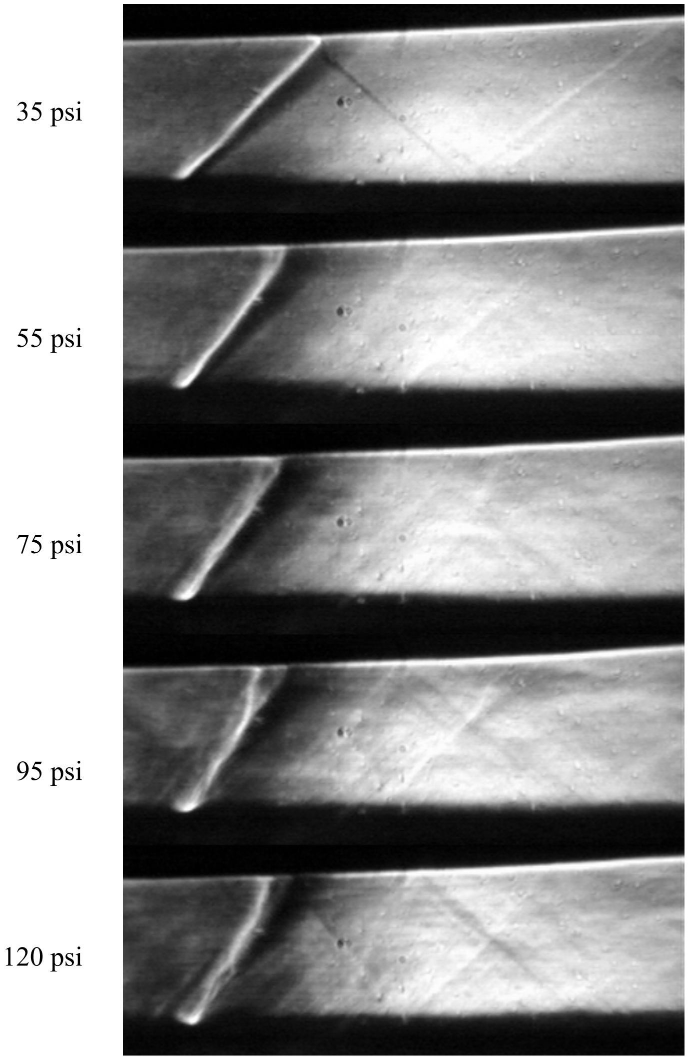

Figure 20. Baseline case at various stagnation pressures.

at the junction. But this gives a means to gauge the flow conditions and Mach number as the stagnation pressure is varied upstream. The angle that this pressure wave makes with the horizontal surface is used to estimate the Mach number in the leading edge of the test section. As the stagnation pressure is increased from 35 psi to 120 psi, the shock angle increases, which translates into a decrease in the Mach number at the section. As explained in the previous section, this trend is surprising because the Mach number would be expected to increase with the stagnation pressure, while the trend here shows the opposite. The analysis of the boundary layer conditions could offer an explanation. The change in the boundary layer conditions can be gauged from these images. Comparison with Figure 19 for boundary thickness estimation discussed in the previous section would be useful. It was mentioned that, the flow conditions in duct would be such that the boundary layer would be in the laminar, transitional or turbulent regime. It can be seen from these figures, that for cases (a) and (b), the boundary layer is probably in the laminar regime which can be seen from the uniform pressure waves and flow structures, while for higher stagnation pressures in (c), (d) and (e), the boundary layer is either transitional or turbulent as observed from the chaotic flow structures.

4.2.2.2. Shallow cavities.

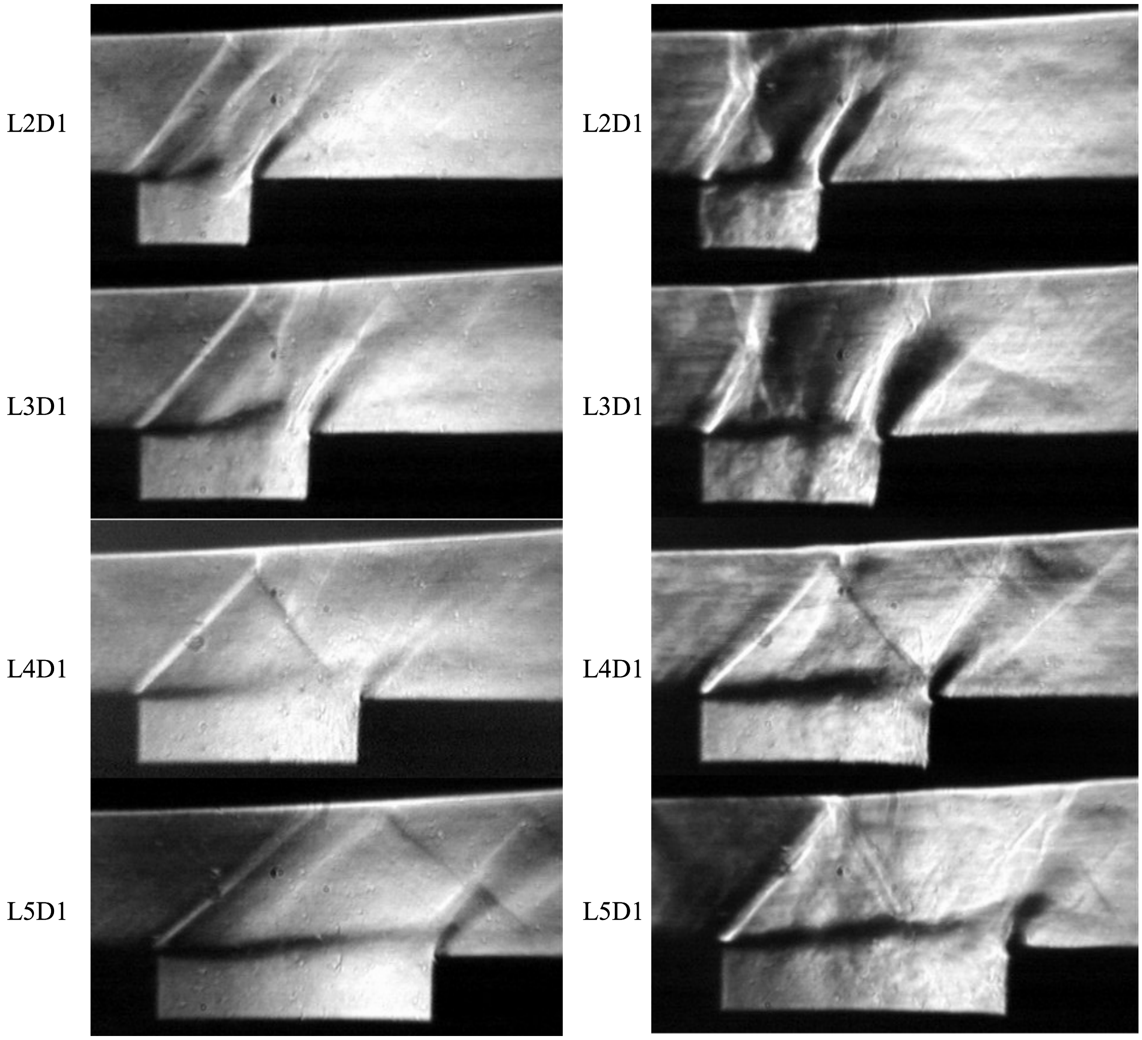

35 psi 120 psi

Figure 21. Schlieren images of shallow cavities at selected stagnation pressures.

Figure 21 shows spark Schlieren images of flow over shallow cavities at the two extreme upstream stagnation pressures of 35 psi and 120 psi. The entire set of Schlieren images for shallow cavities (D/H=0.5) with aspect ratios of 2, 3, 4 and 5 and for upstream stagnation pressures from 35 psi to 120 psi, is included in Appendix A1 as Figure 33 through Figure 37. All these figures are distinctly characterized by the following features of a typical compressible cavity flow: (i) An expansion wave at the leading edge of the cavity, (ii) The shear layer structure spanning the length of the cavity, reattaching downstream of the cavity and (iii) Compression wave at the trailing edge of the cavity. In some cases, additional pressure waves can be seen as a result of the waves reflecting off the top wall. In some of these images, faint roll-up of the shear layer can be noticed, but in other cases comparison of the images and the corresponding pressure spectrum for the same flow conditions would reveal presence of flow resonance in the cavities. As described in the section with the baseline case, it can be seen that the boundary layer characteristics of the cavity vary from laminar to transitional and finally to turbulent as the upstream stagnation pressure is increased from 35 psi to 120 psi. Though it was not able to point out the exact transitions points from the figures, a rough estimate can be made by the sharpness of the pressure waves and the overall flow field. Another fact observed in all the images is that the Mach number appeared to increase with increasing aspect ratios for almost all the stagnation pressure cases. One explanation for this could be the increased expansion that the cavity would experience with the increase in the length of the cavity, which would lead to the increase in the Mach number.

35 psi: Figure 33 shows the Schlieren images of shallow cavities at a stagnation pressure of 35 psi. At this pressure, the boundary layer is probably in the laminar regime, as discussed earlier and thus the flow is rather clean and images are sharp. The image of the L2D1 cavity faintly shows the roll-up of the shear layer, and in the L2D1 and L3D1 images, it can be seen that there is an interaction between the mainstream flow, above the cavity, and that inside the cavity. Also, shock-shear layer interaction can be seen in the L3D1 cavity case.

55 psi: At a stagnation pressure of 55 psi, as depicted in Figure 34, a similar trend to the one observed for the previous case is observed, though the flow structures are slightly more disturbed, or chaotic in this case. Comparing with Figure 18 it can be seen that the boundary layer in this case probably lies in the transitional regime. Again, images of the L2D1 and L3D1 cavities faintly show the roll-up of the shear layer and also depict some aspects of shock-shear layer interaction.

75 psi: As the stagnation pressure is increased to 75 psi, Figure 35 shows that the images are more chaotic, indicating that the boundary layer has probably transitioned to turbulent. Also, it can be seen from the images that the roll-up of the shear layer can be faintly detected for almost all the cavities. Furthermore, all the images show interaction between the flow in the cavity and the mainstream flow above the cavity. And again, the Mach number is seen to be increasing with the increase in the aspect ratio.

95 psi: Figure 41 shows Schlieren images for the 95 psi case. From the thickness of the pressure waves and the appearance of the flowfield, it can be safely predicted that the boundary layer is in the turbulent region. The images also show evidence of the wavy structure of the shear layer spanning the cavity. Evidence of shock-shear layer interaction in the images for L3D1 and L4D1 can also be noticed.

120 psi: Figure 37 shows the Schlieren images for the highest stagnation pressure tested, which was 120 psi. The turbulent nature of the boundary layer can be evidenced from the appearance of the images. The expansion wave at the leading edge of the cavity in the case of L2D1 and L3D1 cavities have large Mach angles, indicating that these near normal shocks might create local subsonic flow downstream.

4.2.2.3. Deep cavities.

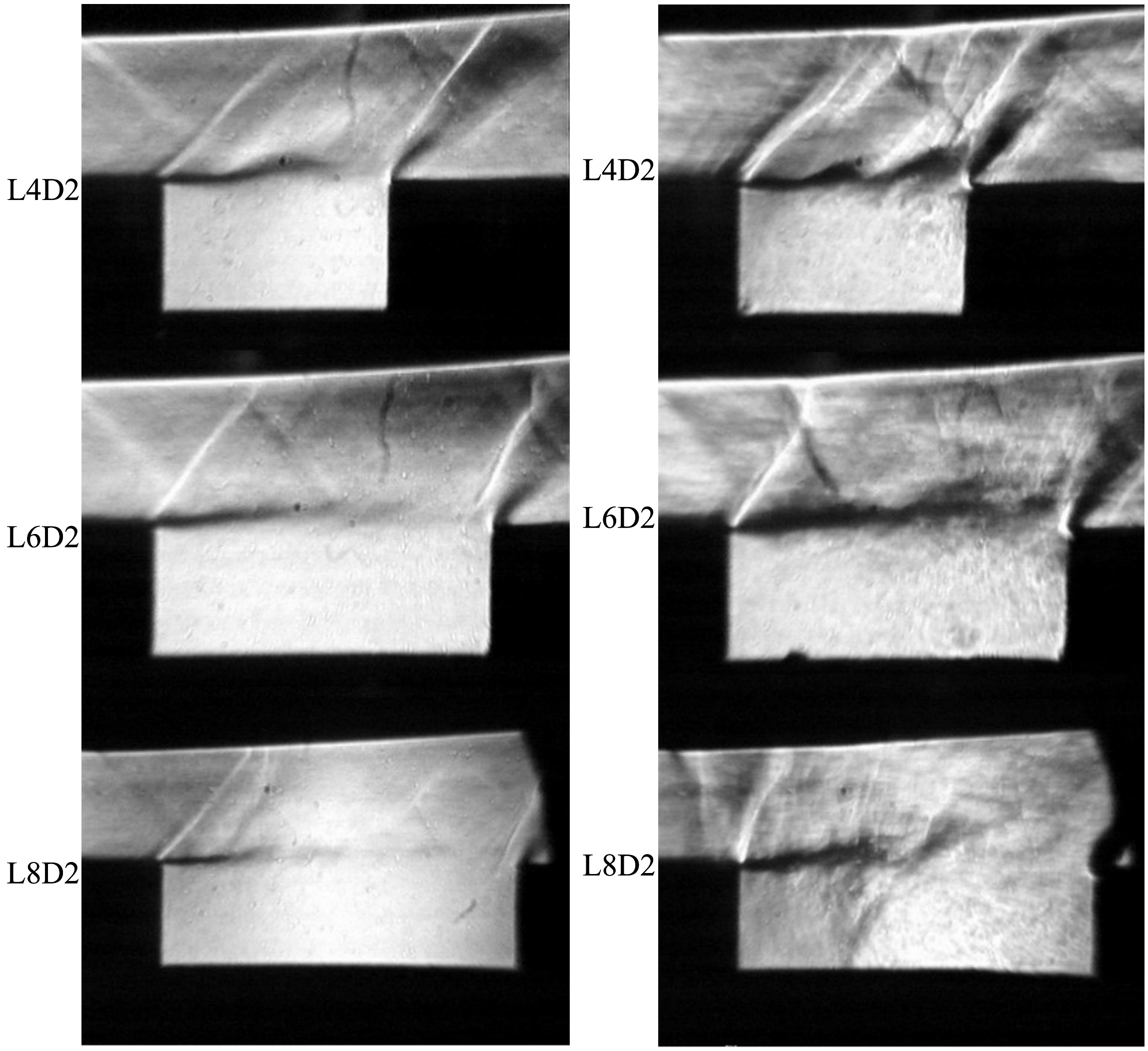

(a) 35 psi

(b) 120 psi

Figure 22. Schlieren images of deep cavities at 35 psi and 120 psi

Figure 22 shows Schlieren images of deep cavities (D/H=1.0) at the two extreme stagnation pressures of 35 psi and 120 psi. The entire set of Schlieren images for the deep cavities with different aspect ratios of 2, 3 and 4 for increasing stagnation pressures from 35 psi through 120 psi are included as Figure 38 through Figure 42 in Appendix A1. In all these cases, the aspects of the flow structures around the cavity are similar to those described in the case of the shallow cavities. An additional feature of these images is that the expansion wave emanating at the 3^0 expansion is clearly visible at the higher left corner of the images. One other salient feature of these figures compared with the one for the shallower cavities is that the pressure wave created at the leading edge of the cavity, after bouncing off the top plate of the flow facility, more often strikes the shear layer somewhere midway of the length of the duct rather than at the trailing edge. This appears to change the flowfield by modifying the shear layer growth pattern. Also, the shear layer appears to lift upward due to the shock interactions. A more thorough study is required to glean more information regarding the shock-shear layer interaction Another features distinct in these images is that the increase in the Mach number with the increase in the aspect ratio is not very marked. In fact in some of the cases, it will be seen that Mach number decreases with increase in aspect ratio.

35 psi: Figure 38 shows the Schlieren images at a stagnation pressure of 35 psi. It appears from the images that the Mach number doesn’t increase with increase in aspect ratio. The flow is rather clean and the pressure waves are sharp, indicating that the boundary layer is probably in the laminar region. Also, an expansion wave can be faintly seen from the top left corner of the images indicative of the 3^0 expansion in the top plate.

55 psi: As the stagnation pressure is increased to 55 psi as shown in Figure 39, the angle of the expansion wave indicates that Mach number decreases with the increase in aspect ratio. Also, the L8D2 cavity produces near normal shocks. The flowfield appears less chaotic, indicating a laminar or transitional boundary layer state. The L4D2 case shows the roll-up of the shear layer. The L6D2 case shows the leading edge pressure wave bouncing off the top plate and interacting with the shear layer midway of the cavity length.

75 psi: Figure 40 for deep cavities at 75 psi shows a trend for Mach numbers similar to the one observed for the previous case, with a near normal shock in the L8D2 cavity case. The flowfield in this set of figures is more chaotic, indicating that the boundary layer is probably in a transitional or turbulent state. The L4D2 and L6D2 cavities show the wavy structure of the shear layer spanning the cavities. The L6D2 and L8D2 cavities show the shear layer lifted upward after its interaction with the shock wave.

95 psi: The images in Figure 41 for the 95 psi case show trends similar to the previous cases as far as Mach number is concerned. It decreases with increasing length of the cavity. Almost all the cavity cases show the shear layer growth structures. But, in these high stagnation pressure cases, the expansion wave at the leading edge of the cavity was highly oscillatory, making the estimation of the Mach number a difficult task.

120 psi: Figure 42 shows Schlieren images for the 120 psi case, where the boundary layer appears turbulent. The L8D2 cavity shows near normal shocks at the leading edge of the cavity and the L4D2 cavity shows the roll-up of the shear layer spanning the mouth of the cavity. Again, the leading edge expansion wave had large oscillations as observed from the real time recording and thus the exact prediction of the Mach numbers based on the shock angles became difficult. This would be discussed in the next subsection.

4.2.2.4. Oscillations of the leading edge shock.

L6D2 cavity*:* Figure 43 and Figure 44 in Appendix A1 have been included in order to analyze the oscillating phenomena of the expansion wave at the leading edge of the L6D2 and L8D2 cavities that was evident from the real time images of the flow. In Figure 43, image (a) shows the various stages of the shock wave for the L6D2 cavity at 95 psi, where the three images presented are instantaneous images of the flow at the same condition but at different times, which gives an idea of how the flow behaves. As it can be seen in the first image, the flow has a higher Mach number and is supersonic through out. But in the next image, the expansion wave angle is vastly different and nearly normal. In the last image, a curved shock is seen and the flow is probably subsonic downstream of this shock. Again, a look at figure (b) shows a similar variation at 120 psi. A thorough investigation is required to determine the possible cause of this variation.

L8D2 Cavity:

In Figure 44, the oscillation of the leading shock has been clearly depicted for the L8D2 cavity at stagnation pressures of 95 psi and 120 psi. For both pressures, the rather unsteady behavior of the leading edge shock can be seen. While the first image in each case shows a smaller angle of the shock and thus a higher Mach number, the successive images show almost normal shocks and in the last case, almost curved shocks are observed, with possible subsonic flow downstream. These images appear to depict a phenomenon that could be due to the flow instabilities inherent in the higher-pressure cases. But, such oscillations were not observed for the shallow cavities. The oscillating trends in the deep cavities show that the flow traversing the cavity was highly unsteady and complex, with mixed supersonic-subsonic regions. Even under these conditions, the existence of flow induced cavity resonance shows that this mechanism is quite robust even under off-design conditions.

4.2.2.5. Effect of cavity aspect ratio (L/D).

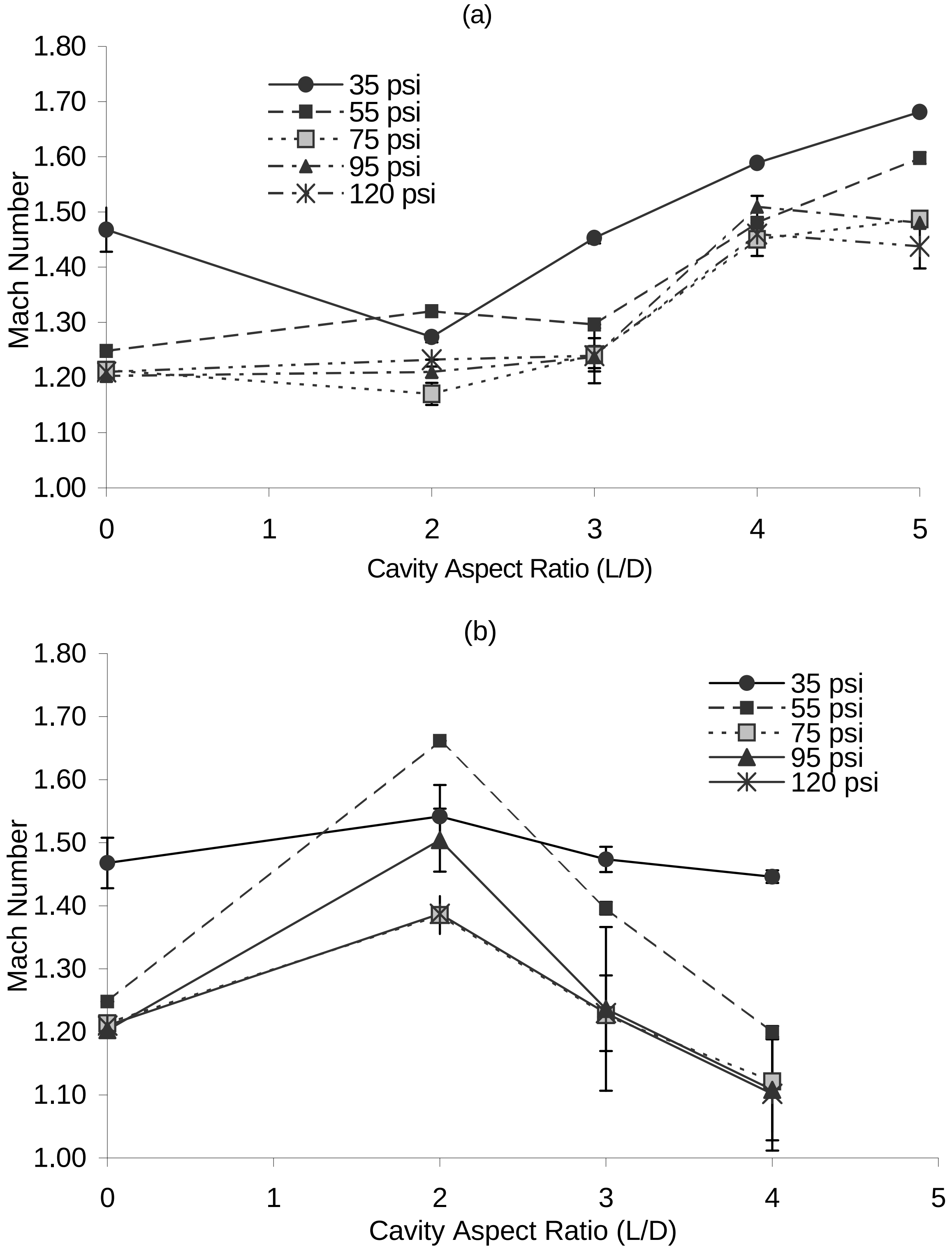

Figure 23. Mach number as a function of cavity Aspect Ratio for (a)D/H=0.5 & (b)D/H=1.0

Figure 23 and Figure 24 summarize the estimated Mach number results obtained from the Schlieren images both for shallow and deep cavities. The variation of leading edge Mach number with respect to the cavity aspect ratio has been analyzed for varying upstream stagnation pressures. Here, plot (a) depicts the Mach number variation for the shallow cavities. It can be seen that, as the cavity aspect ratio was increased for a given cavity depth, the Mach number appeared to be increasing slightly for all the stagnation pressures of interest. This could be attributed to the increased expansion area is available for the flow as the aspect ratio, and subsequently the length of the cavity, are increased. When the depth of the cavity was increased by a factor of two, however, the trend associated with the aspect ratio appeared to be different. Plot (b) shows the Mach number results for the deeper cavities for varying stagnation conditions. As it can be seen, the Mach number appeared to be smaller with the larger aspect ratio. The reversal in the trend appeared to be related to the fact that the pressure deficit in the cavity volume was too large to sustain supersonic flow. Also, it can be seen from plot (b) that some of the larger cavities have large variations in Mach numbers at higher stagnation pressure. This is the effect of the shock oscillations that were discussed in the previous subsection, which caused an uncertainty in the estimation of the Mach number.

4.2.2.6. Effect of upstream stagnation pressure.

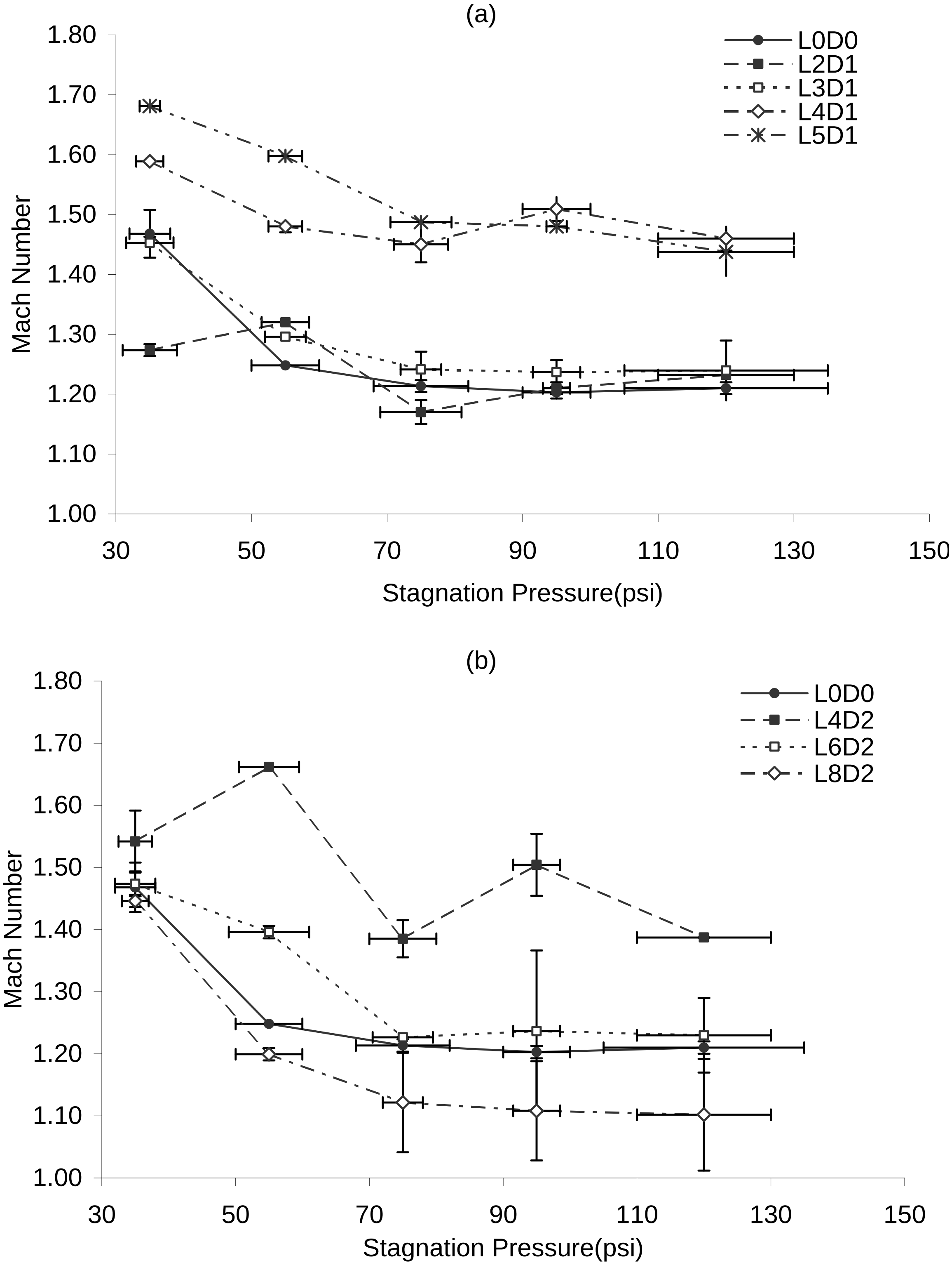

Figure 24. Variation of Mach number with stagnation pressure for (a)D/H = 0.5 & (b)D/H=1.0

To analyze the results in a slightly different manner, plots of the leading edge Mach number as a function of upstream stagnation pressures were generated with varying cavity aspect ratio for both shallow and deep cavities as shown in Figure 24. In this figure, plots (a) and (b) depict these variations for shallow and deep cavities respectively. Referring to plot (a), it can be seen that in all the cavity configurations, the Mach number appears to decrease with the increase in the stagnation pressures, which, as stated earlier was rather surprising. This trend could be attributed to the varying conditions at the nozzle and the presence of shocks at higher stagnation pressures as discussed in the previous sections. The boundary layer modification discussed earlier could also play a part in modifying the flow configuration. As noted in the previous section, huge variations in the higher values of the stagnation pressures can also be observed. The trend of the Mach number decrease with the increase in the stagnation pressure is similar for the deeper cavities depicted in plot (b), except for the L4D2 case. Again, large uncertainties in the Mach numbers associated with the higher-pressure cases can be observed, with near values very close to 1.0 for some cases.

4.2.3. Cavity unsteady pressure response measurements.

The unsteady pressure measurements were carried out using a pressure transducer flush mounted with the side plate. For each cavity configuration, the stagnation pressure was varied from 30 psi to 120 psi and the pressure spectra was obtained by conducting Fast Fourier Transform as described earlier.

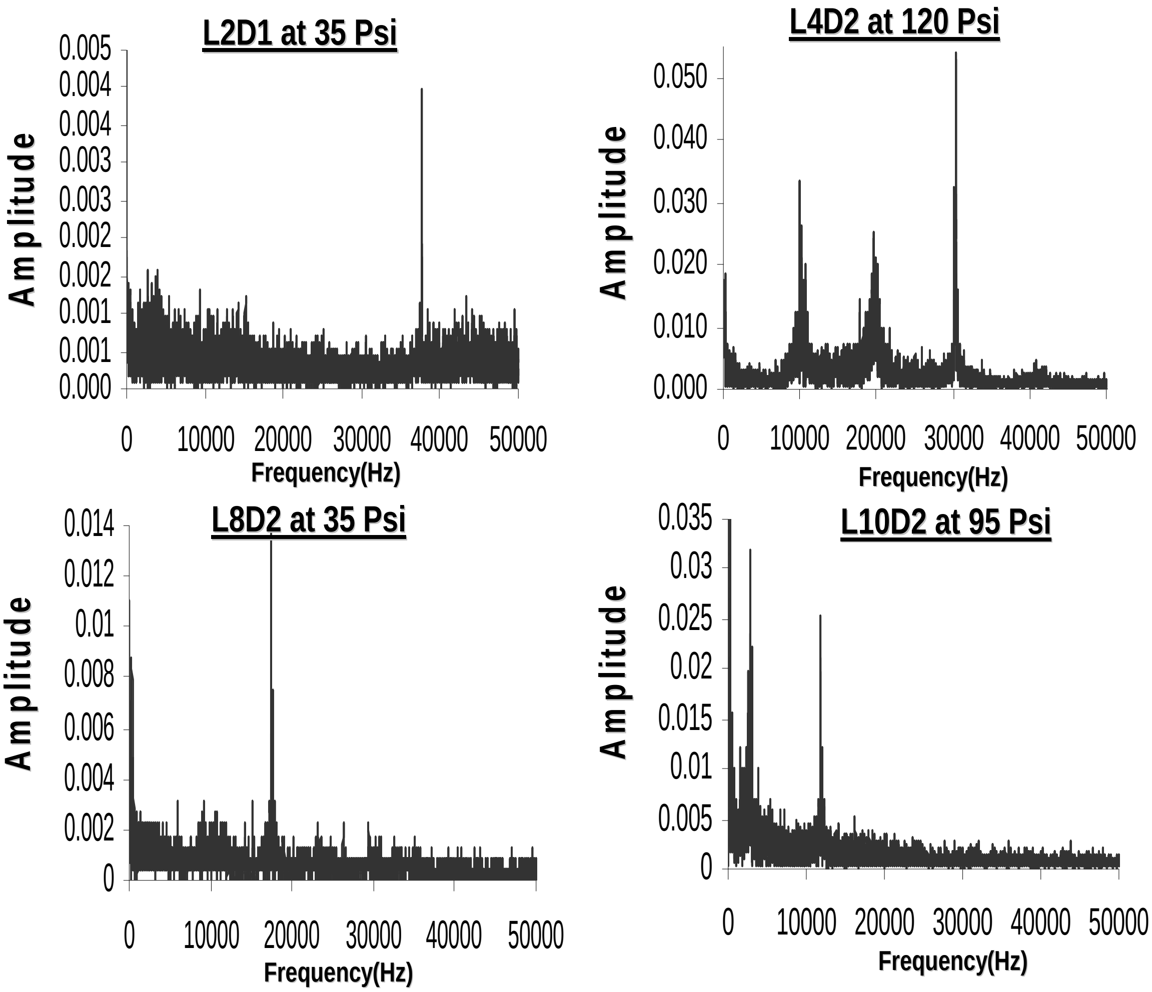

Figure 25. Typical unsteady pressure spectra for selected cavity cases.

Figure 25 shows the power spectra of the unsteady pressure for a few typical cases. It can be seen that while some of the cases show a single dominant peak, other cavities have multiple peaks, with the secondary peaks being harmonics of the fundamental frequency.

The pressure spectra obtained for all the cavity configurations at increasing stagnation pressures are depicted from Figure 50 through Figure 57 in Appendix B1. As can been seen from these figures, some of the cases exhibit a single dominant peak while in other cases very strong harmonics or other frequencies were detected. Based on past studies (Murray & Elliot [27], Kegerise [25]), it was expected that the spectra of the unsteady pressure signals would exhibit several peaks or modes at a discrete set of frequencies and that these frequencies would be well correlated with the Rossiter model (Tracy & Plentovich . A comparison of Rossiter predicted results and those obtained in this experimental study would be discussed in detail at the end of this section. Usually, the sound pressure level (SPL) of the unsteady pressure data is expressed in psi dB as $SPL = 20\log\left(\frac{P}{2.9*10^{-9}\,psi}\right)$. But it was decided to express the unsteady pressure data in the psi form itself rather than SPL for clarity. SPL data has also been included for reference in Table 2 and Table 3 that depict the frequency and amplitude data for the shallow and deep cavities respectively. The power spectra of each of the cavity configurations are analyzed in the next section.

Table 2. Measured peak frequencies and amplitudes for shallow cavities.

P_0 (psi)	**L2D1**			**L3D1**			**L4D1**			**L5D1**		
	Freq KHz	Amp Psi	SPL dB	Freq KHz	Amp Psi	SPL dB	Freq KHz	Amp Psi	SPL dB	Freq KHz	Amp Psi	SPL dB
30	38.4	0.002	116.8	15.2	0.003	120.3	15.2	0.007	127.7	15.2	0.002	116.8
35	37.6	0.004	122.8	21.4	0.002	116.8	15.2	0.007	127.7	15.2	0.003	120.3
55	37.1	0.006	126.3	25.9	0.005	124.7	15.2	0.007	127.7	15.2	0.003	120.3
75	37.5	0.012	132.3	25.3	0.006	126.3	15.2	0.008	128.8	27.9	0.003	120.3
95	36.8	0.018	135.9	25.5	0.010	130.8	20.4	0.015	134.3	27.6	0.005	124.7
120	36.8	0.032	140.9	25.0	0.068	147.4	20.1	0.018	135.9	26.7	0.007	127.7

Table 3. Measured peak frequencies and amplitudes for shallow cavities.

P_0 (psi)	**L4D2**			**L6D2**			**L8D2**			**L10D2**		
	Freq KHz	Amp Psi	SPL dB	Freq KHz	Amp Psi	SPL dB	Freq KHz	Amp Psi	SPL dB	Freq KHz	Amp Psi	SPL dB
30	21	0.001	110.8	23.6	0.003	120.3	17.6	0.01	130.8	8.6	0.003	120.3
35	20.4	0.073	148.0	22.7	0.005	124.7	17.5	0.014	133.7	9.1	0.005	124.7
55	19.8	0.027	139.4	21.5	0.011	131.6	10.1	0.02	136.8	12	0.007	127.7
75	19.5	0.003	120.3	21.3	0.025	138.7	10.1	0.038	142.3	12	0.014	133.7
95	30.4	0.051	144.9	21.2	0.03	140.3	9.9	0.057	145.9	11.8	0.025	138.7
120	30.3	0.054	145.4	21.2	0.036	141.9	9.9	0.095	150.3	12	0.018	135.9

4.2.3.1. Rossiter predicted results.

In section 2.3, Rossiter model and its modifications were discussed to explain the acoustic characteristics of flow-induced resonance in cavities. Here, these results are used to compare the observed frequencies with the predicted results. Tables 4 and 5 show comparisons of the predicted frequencies and Strouhal number obtained from the experiments with those calculated from the modified Rossiter predicted results using results from Heller & Bliss [24], for shallow and deep cavities respectively.

In Table 4 for shallow cavities and Table 5 for deep cavities, the Mach number estimated from the Schlieren images is used to calculate the flow velocity U, used in these calculations. The temperature of the flow at the duct is calculated using the isentropic flow relations, since the stagnation temperature is known upstream. The length of the cavity for each case is used as the length scale in the Strouhal number computations. The Strouhal number for the experimental frequencies is depicted as f_{exp}L/U, where f_{exp} is the experimental peak frequency described in the previous sections, L is the length of the cavity for each case and U is the flow velocity obtained from the Mach number using isentropic flow relations. The value of κ, which is taken as the ratio of convective velocity of the vortical structures in the shear layer to the freestream velocity, as obtained in section 2 is used:

$$\kappa = \frac{1}{\dfrac{1}{\sqrt{1+\dfrac{\gamma-1}{2}M^2}}+1}$$

Table 4. Comparison of predicted and experimental frequencies for shallow cavities

Duct	P0	f_{exp}	M	T_{duct}	U	St No.	κ	Predicted Frequencies			St No.
	psi	KHz		K	m/sec	f_{exp} L/U		m=1	m=2	m=3	f_{pred}L/U
L2D1	35	37.6	1.27	222.4	380.7	0.63	0.54	15.11	35.26	55.41	0.59
	55	37.1	1.32	218.9	391.4	0.60	0.54	15.42	35.98	56.55	0.58
	75	37.5	1.17	230.1	355.7	0.67	0.53	14.37	33.54	52.70	0.60
	95	36.8	1.21	227.6	365.8	0.64	0.53	14.68	34.25	53.82	0.59
	120	36.8	1.23	226.3	371.5	0.63	0.53	14.85	34.65	54.45	0.59
L3D1	35	21.4	1.45	207.2	419.1	0.49	0.54	10.80	25.19	39.59	0.57
	55	25.9	1.30	220.9	386.1	0.64	0.54	10.18	23.75	37.33	0.59
	75	25.3	1.24	224.1	372.1	0.65	0.53	9.90	23.11	36.31	0.59
	95	25.6	1.24	225.4	371.9	0.65	0.53	9.90	23.11	36.32	0.59
	120	24.9	1.24	225.9	372.4	0.64	0.53	9.92	23.14	36.36	0.59
L4D1	35	15.2	1.59	195.7	445.6	0.43	0.55	8.46	19.74	31.02	0.56
	55	15.2	1.48	205.2	425.0	0.45	0.55	8.18	19.09	30.00	0.57
	75	15.2	1.45	206.4	417.4	0.46	0.54	8.07	18.82	29.58	0.57
	95	20.4	1.51	202.1	430.1	0.60	0.55	8.25	19.24	30.24	0.57
	120	20.1	1.46	206.9	420.8	0.61	0.54	8.12	18.95	29.78	0.57
L5D1	35	15.2	1.68	188.2	462.3	0.52	0.56	6.95	16.21	25.48	0.56
	55	15.2	1.60	195.4	447.6	0.54	0.55	6.79	15.85	24.91	0.56
	75	27.9	1.49	203.2	424.9	1.05	0.55	6.54	15.25	23.97	0.90
	95	27.6	1.48	204.6	424.4	1.03	0.55	6.53	15.25	23.96	0.90
	120	26.7	1.44	208.8	416.1	1.02	0.54	6.44	15.04	23.63	0.90

Table 5. Comparison of predicted and experimental frequencies for deep cavities.

Duct	P0	f_{exp}	M	T_{duct}	U	St No.	κ	Predicted Frequencies			St No.
	psi	KHz		K	m/sec	f_{exp} L/U		m=1	m=2	m=3	f_{pred} L/U
L4D2	35	20.4	1.54	199.8	436.3	0.59	0.55	8.33	19.45	30.56	0.57
	55	19.8	1.66	190.1	459.3	0.55	0.55	8.65	20.18	31.71	0.56
	75	19.6	1.38	211.9	403.9	0.62	0.54	7.88	18.38	28.89	0.58
	95	30.4	1.50	202.8	428.6	0.90	0.55	8.23	19.20	30.17	0.89
	120	30.4	1.39	213.0	405.8	0.95	0.54	7.91	18.47	29.02	0.91
L6D2	35	22.9	1.47	205.4	423.2	1.03	0.54	5.44	12.68	19.93	0.90
	55	21.3	1.40	212.4	407.8	1.00	0.54	5.29	12.35	19.41	0.91
	75	21.3	1.23	225.3	369.0	1.10	0.53	4.92	11.48	18.04	0.93
	95	21.1	1.21	227.7	365.4	1.10	0.53	4.89	11.41	17.93	0.93
	120	21.1	1.22	226.9	369.8	1.09	0.53	4.93	11.51	18.09	0.93
L8D2	35	17.5	1.45	207.7	417.8	1.07	0.54	4.04	9.42	14.81	0.90
	55	10.2	1.20	229.2	363.9	0.71	0.53	3.66	8.53	13.41	0.60
	75	10.1	1.10	235.8	339.3	0.76	0.53	3.47	8.10	12.73	0.61
	95	9.9	1.09	237.9	336.5	0.75	0.53	3.45	8.06	12.66	0.61
	120	9.9	1.07	239.8	333.0	0.76	0.53	3.43	8.00	12.57	0.61

Thus the Strouhal number is calculated from section 2.3 as:

$$St_{\infty} = \frac{f_m L}{U_{\infty}} = \frac{m - \alpha}{\frac{1}{\kappa} + \frac{M_{\infty}}{\sqrt{1 + \frac{\gamma - 1}{2} M_{\infty}^2}}}$$

where *m* in the table and in the above formula denotes the Rossiter mode as 1,2,3…and α is the phase lag factor as described earlier. The shaded values indicate the frequencies corresponding to the experimental results and also those predicted using the modified Rossiter model of Heller & Bliss [24]. Since the table gives value of predicted frequencies for the first three modes of oscillations, the shaded values indicate the Rossiter mode that is closest to the observed frequency. Some of these values vary significantly from the experimental results indicating that the mode of oscillation could also be different from the predicted longitudinal mode.

It can be observed from the shaded portion of the tables that, for a particular cavity which is subjected to various stagnation pressures, these might be a sudden shift in frequency to a different value. This phenomenon, where the frequency mode of the shear layer structures changes to a different value, has been termed as mode-hopping. Based on the cavity acoustics presented in section 2.3, when the mode of the cavity changes from the first mode to the second mode, this indicates that, an additional feedback look has been started before the first one finishes. This would mean that the vortices or large scale structures produced from the cavity would increase if the mode of the frequency increases. This might have a direct influence on the mixing enhancement characteristics, because mixing is governed by the large scale structures and their growth rates. Thus, mode hopping behavior appears to be a critical factor, if the flow induced cavity mechanism were to be used in a Scramjet combustor.

4.2.3.2. Power Spectra of pressure oscillations:

Figure 50 through Figure 57 in Appendix B1 depict the power spectra of the pressure oscillations obtained for all the cavity configurations. All the cavity cases showed nice frequency response for the range of flow conditions through which they were subjected. As seen earlier, some of these had single dominant peaks while others had harmonics of the fundamental frequencies and also some depicted the mode hopping behavior.

4.2.3.2.1. Shallow cavities:

L2D1: Figure 50 (i), (ii) and (iii) show the power spectra of the pressure oscillation for the shallow cavity with aspect ratio of 2 for increasing stagnation pressures from 30 psi to 120 psi. It can be observed that in all these cases there is a single dominant peak at about 37 KHz. The frequency value doesn’t vary much with the increase in stagnation pressure, i.e., mode-hopping behavior is absent. The amplitude level expresses the magnitude of the pressure oscillation in psi. It can be seen that the amplitude increases with increasing stagnation pressure. This could be due to a general overall increase in the disturbance level with increase in stagnation pressure. Comparison of the frequencies with the Rossiter modified model, as done in Table 4, indicates that the experimental values match pretty closely with the trend observed with the modified model.

L3D1: Figure 51(i), (ii) and (iii) depict the power spectra of the unsteady pressure component for the shallow cavity with aspect ratio 3. At 30 psi, a single dominant peak is observed at a relatively low frequency of about 15 KHz. For 35 psi, the peak is not as dominant and has a slightly higher frequency of about 21 KHz, but for larger stagnation pressures from 55 psi to 120 psi, oscillations at a higher frequency of about 25 KHz are observed, indicating a shift in the frequency. Mode hopping thus occurs between 35 psi to

55 psi range. Also, for pressures above 55 psi, harmonics of the fundamental frequencies are also observed. From the modified Rossiter predicted of Table 4, it can be estimated that the primary mode of the oscillations here is of the second order and the harmonics observed are of first order. Again, it can be observed that there is steady increase in the amplitude level of the peak frequency with increasing stagnation pressures.

L4D1: Figure 52 (i), (ii) and (iii) depict the unsteady pressure spectra for the shallow cavity with aspect ratio of 4. In these frequency plots, a single dominant peak at about 15 KHz with almost constant amplitude can be observed for stagnation pressures from 30 psi to 75 psi. For higher stagnation pressures of 95 psi and 120 psi, a higher frequency was observed which suggested mode-hopping behavior. Also the amplitude increased for these cases following a trend similar to the previously discussed cavity configurations.

L5D1: Figure 53 (i), (ii) and (iii) show the unsteady pressure spectra for the shallow cavity with aspect ratio of 5. The trend is similar to the L4D1 cavity from 30 psi to 55 psi with an observed peak frequency of about 15 KHz at almost constant amplitude. As the stagnation pressure is increased to 75 psi, a shift in the peak is observed and for higher stagnation pressures, the frequency is maintained at this higher value of about 27 KHz. This is certainly a higher mode of oscillation and from the calculations of Rossiter predicted values of Table 4, it can be seen that while the 15 KHz peaks roughly correspond to the second mode, the higher frequency corresponds to the third mode of oscillations. Thus, mode-hopping behavior is clearly evidenced from these results. Again the amplitude levels increase with stagnation pressure possibly indicative of the overall increase in the disturbance level in the flow.

4.2.3.2.2. Deep cavities:

L4D2: The pressure spectra for this cavity are depicted in Figure 54 (i), (ii) and (iii). It can be seen that, for all stagnation pressure cases, favorable frequency response was obtained from the cavity. It can be seen from the figures that for the 30 psi case, two peaks are observed, the dominant peak at about 20 KHz and the other at about 10 KHz. From the modified Rossiter calculations of Table 5, it can be seen that the 20 KHz peak corresponds to the second mode and the 10 KHz peak to the first mode of oscillation. For the 35 psi case, only the 20 KHz peak is present, while for the 55 psi case, in addition to the two peaks at 10 and 20 KHz, a peak is also observed at about 30 KHz, which indicates a harmonic of the third order. Again, for the 75 psi case too, a similar trend is observed. In all the above cases, it is to be noted that the 20 KHz peak dominates. For higher stagnation pressure value of 95 psi, though all the three peaks are present, a shift in the dominant peak is observed to the 30 KHz value. Thus mode hopping occurs here and the third mode dominates for stagnation pressures greater than 95 psi. The pressure spectrum for the 120 psi case is similar to the 95 psi case with three peaks but with the 30 KHz peak dominating.

L6D2: From the power spectra of the unsteady pressure depicted in Figure 55 (i), (ii) and (iii), the L6D2 cavity can be seen to have a stable frequency response with no mode hopping behavior. For upstream stagnation pressure of 30 psi and 35 psi, three prominent peaks can be observed, with the peak at about 23 KHz being dominant. The other peaks at about 15 KHz and 30 KHz could either be harmonics of the fundamental frequency or other modes of oscillations. The modified Rossiter predictions of Table 5 don’t appear to match for this case at least for the 1st and 3rd modes. Further calculations reveal that the

30 KHz case could be a fifth mode oscillation. As the stagnation pressure is increased to 55 psi, a slight decrease of the frequency of the dominant peak to about 21 KHz can be observed. As the stagnation pressure is increased to higher pressures from 55 psi to 120 psi, the peak frequency remains almost constant at about 21 KHz with additional peaks observed at about 14 KHz and 29 KHz.

L8D2: Figure 56 (i), (ii) and (iii) show the pressure spectra of the pressure at various stagnation pressures for this deep cavity with aspect ratio of 4. It can be seen that, for stagnation pressures of 30 psi and 35 psi, pressure spectra are obtained with a dominant peak at about 17.5 KHz. Comparison with the modified Rossiter predicted results of Table 5 don’t reveal any similarity to fundamental mode of oscillations predicted. The reasons could be that there could be errors in the frequency characterization or the oscillations could be in a different mode other than the longitudinal mode or the usage of Mach number inherent in the modified Rossiter predictions could bring in some anomalies. But it is suspected that the reason is probably the latter, because for this cavity, the estimation of Mach number became difficult due to the oscillating nature of the shock structure, as discussed in the previous section. As the stagnation pressure is increased to 55 KHz and higher, there is definitive shift of the peak frequency to a value of about 10 KHz. It is a bit surprising that, while for all the other cavities, the mode hopping behavior shows a shift in the frequency to a higher value, here the shift is towards a lower value. The peak frequency is maintained at about 10 KHz for higher stagnation pressures, but the amplitude values fluctuate rather than increase with the stagnation pressure.

L10D2: Figure 57 (i), (ii) and (iii) show the pressure spectra obtained for this deeper cavity with aspect ratio of 5. The modified Rossiter predicted values for this cavity could not be obtained, due to lack of Schlieren images for this case due to the limitations of the lens system. It can be seen from the figures that, for a stagnation pressure of 30 psi, a single dominant peak is observed at about 9.5 KHz. As the stagnation pressure is increased, the peaks are not very dominant and the one observed at about 9 KHz was taken as the fundamental mode. As the stagnation was increased to 55 psi and beyond, there was a shift of the peak frequency to about 12 KHz that suggested mode-hopping behavior, but it was difficult to predict the actual mode due to the lack of Mach number data.

4.2.3.3. Effect of cavity aspect ratio (L/D).

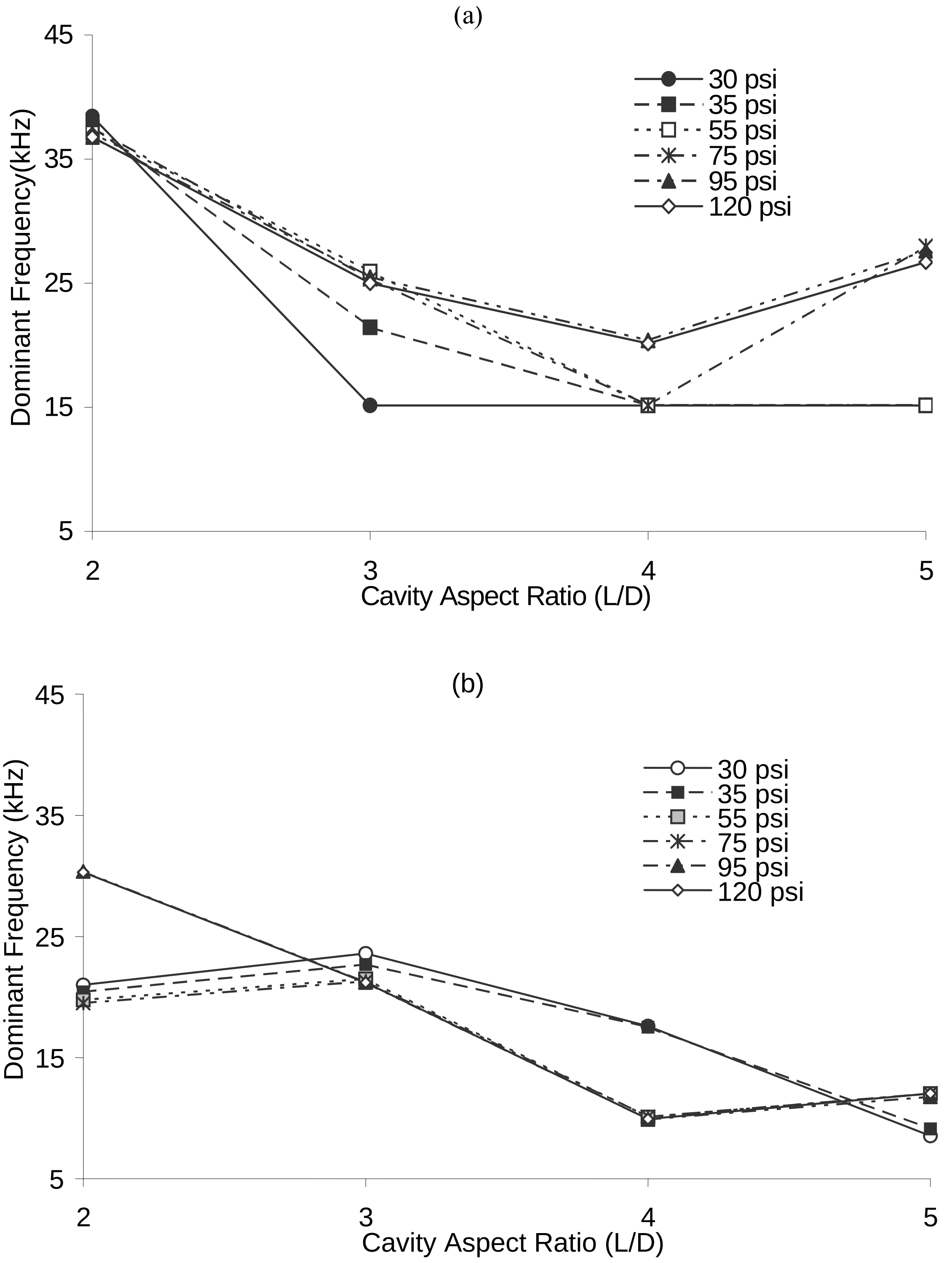

Figure 26. Peak amplitude frequency as a function of cavity aspect ratio for (a) D/H=0.5 and (b) D/H=1.

Figure 26 through Figure 29 show a summary of the knowledge gleaned from the above discussions regarding the pressure response measurements. Figure 26 shows how the peak frequencies of oscillation were affected by the cavity aspect ratio for both shallow and deep cavities. In this figure, plot (a) shows the results of peak frequency for the shallow cavities with D/H ratio of 0.5 for the stagnation pressures of interest. As it can be seen from the plot, the peak frequency reduces with increase in the cavity aspect ratio for almost all the stagnation pressure pressures.

For higher cavity aspect ratios of 3 and above, mode-hopping behavior can be seen from the location of the peak frequency points. Plot (b) shows the frequency data for the deep cavities as a function of cavity aspect ratios for varying stagnation pressures studied. The trend is similar to the shallow cavity case, with the dominant frequency decreasing with increasing aspect ratio. But here it can be seen that mode-hopping behavior is observed for the smaller cavity with aspect ratio of 2 also, indicating that mode-hopping behavior could be dependent on the depth to height (D/H) ratio of the cavity too.

4.2.3.4. Effect of stagnation pressure.

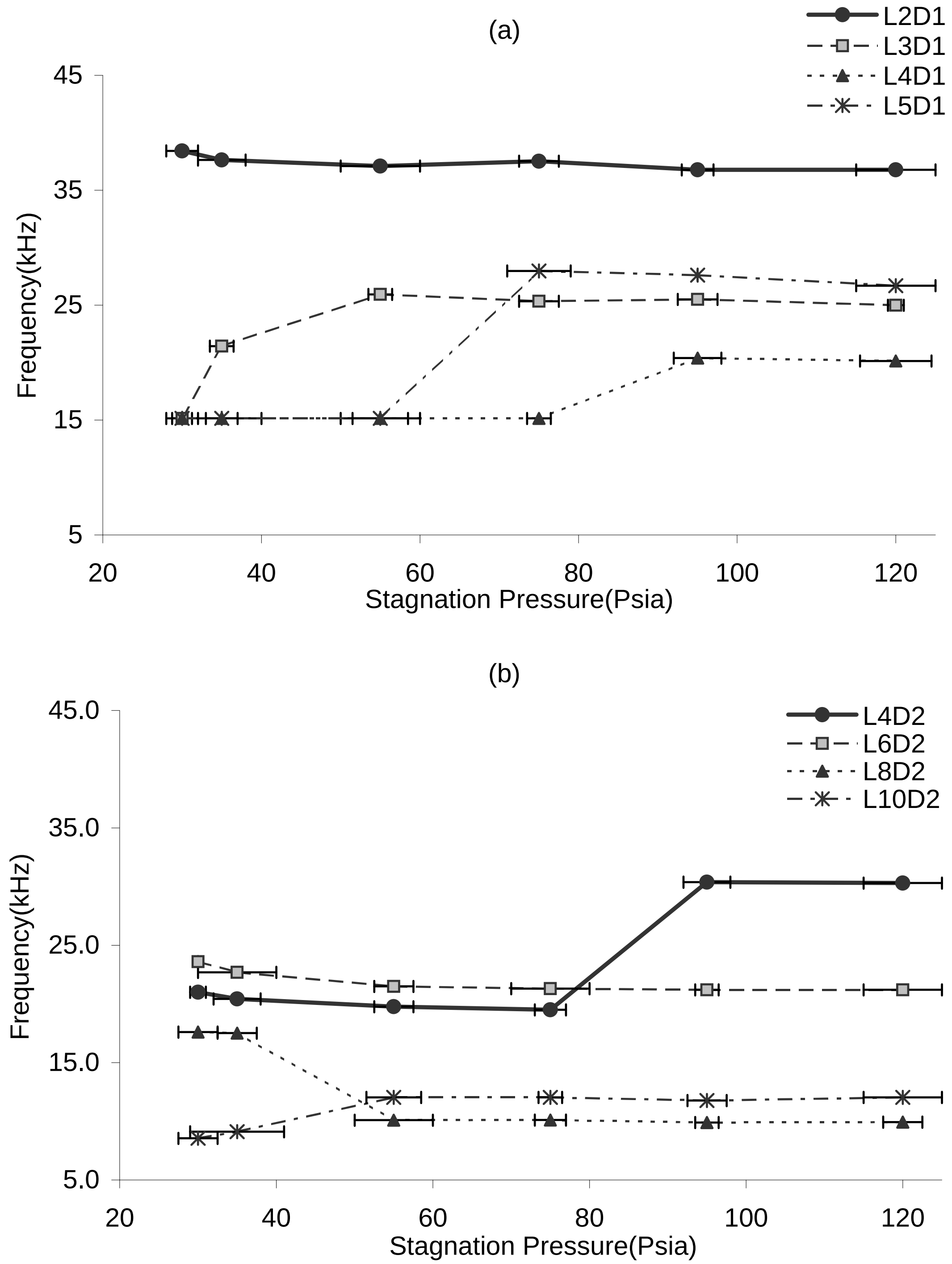

Figure 27. Peak Frequency as a function of upstream stagnation pressure for (a)D/H=0.5 & (b) D/H=1.

Figure 27 shows how the peak frequency was affected by the stagnation pressure for each cavity case. In this figure, plot (a) depicts the variation of peak frequency as a function of the upstream stagnation pressure for shallow cavities with D/H=0.5. This gives a better idea of the mode-hopping behavior exhibited by the cavities. As it can be seen from the plot, the L2D1 cavity is fairly steady for the stagnation pressures of interest, in that there is no mode hopping behavior. For all the higher aspect ratio cavities, mode-hopping behavior is exhibited. While the L3D1 cavity exhibits mode hopping at 55 psi, the larger cavities, L4D1 and L5D1, exhibit similar behavior at stagnation pressures of 95 psi and 75 psi respectively. Though no definitive trend can be detected with the mode hopping patterns of the cavity, this behavior is of importance and merits further investigation.

Plot (b) is for the deep cavities with D/H=1.0, depicting the variation of the peak frequency with upstream stagnation pressure for various aspect ratios. Here, the L6D2 cavity is the exception regarding mode-hopping behavior. While the larger cavities, L8D2 and L10D2, show mode hopping at a relatively lower stagnation pressure of 55 psi, the shorter cavity, L4D2, shows mode hopping at a higher stagnation pressure of 95 psi.

4.2.3.5. Spectral amplitude of the dominant peak.

The amplitude dependence on aspect ratio is shown in Figure 28 (a) and (b) for shallow and deep cavities respectively. These plots give an idea of the range of amplitudes obtained for the various cavities at different stagnation pressure and is an indication that almost all the cases that were tested yielded coherent oscillations that could be used to enhance mixing.

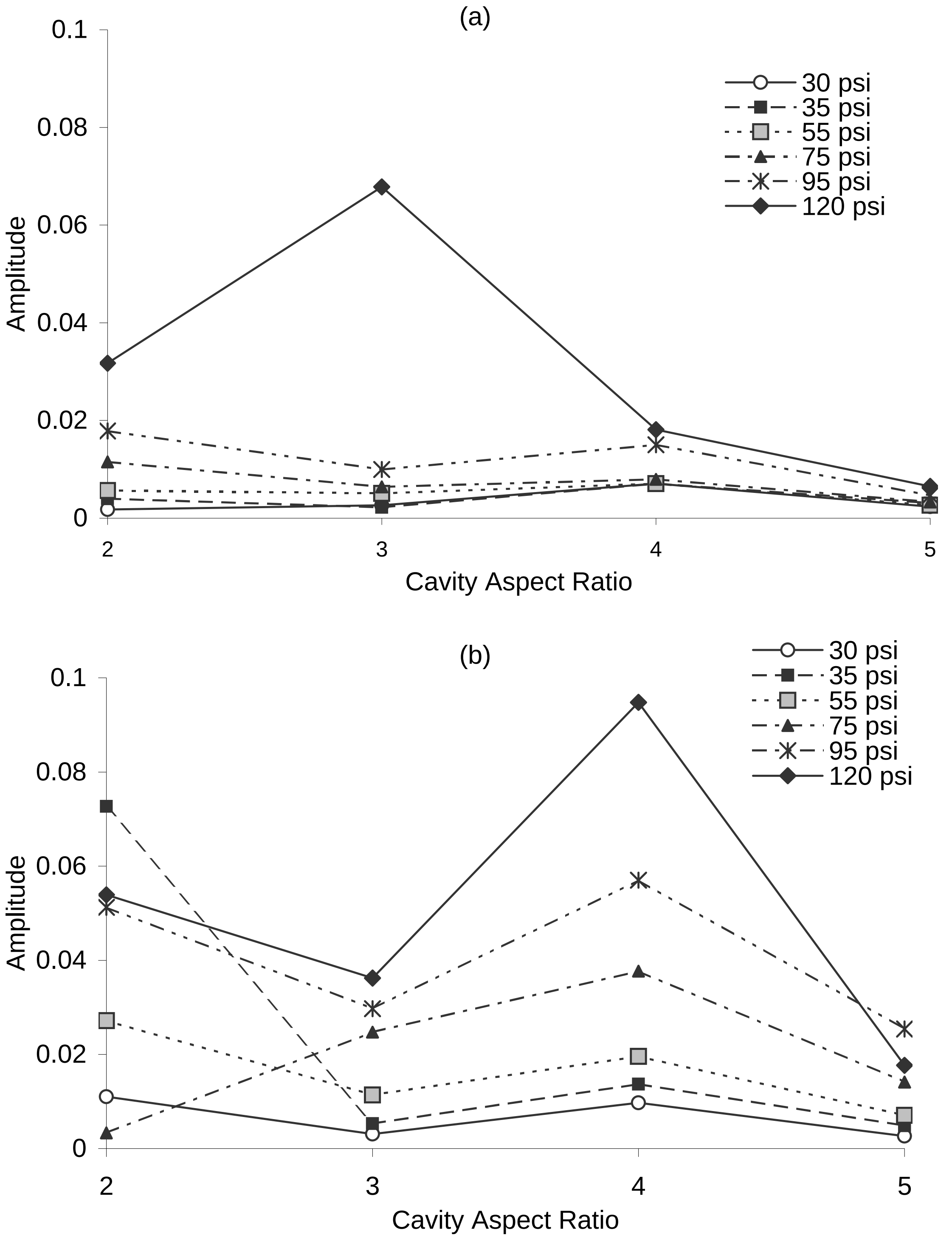

Figure 28. Spectral amplitude as a function of cavity aspect ratio for (a) D/H=0.5 and (b) D/H=1.

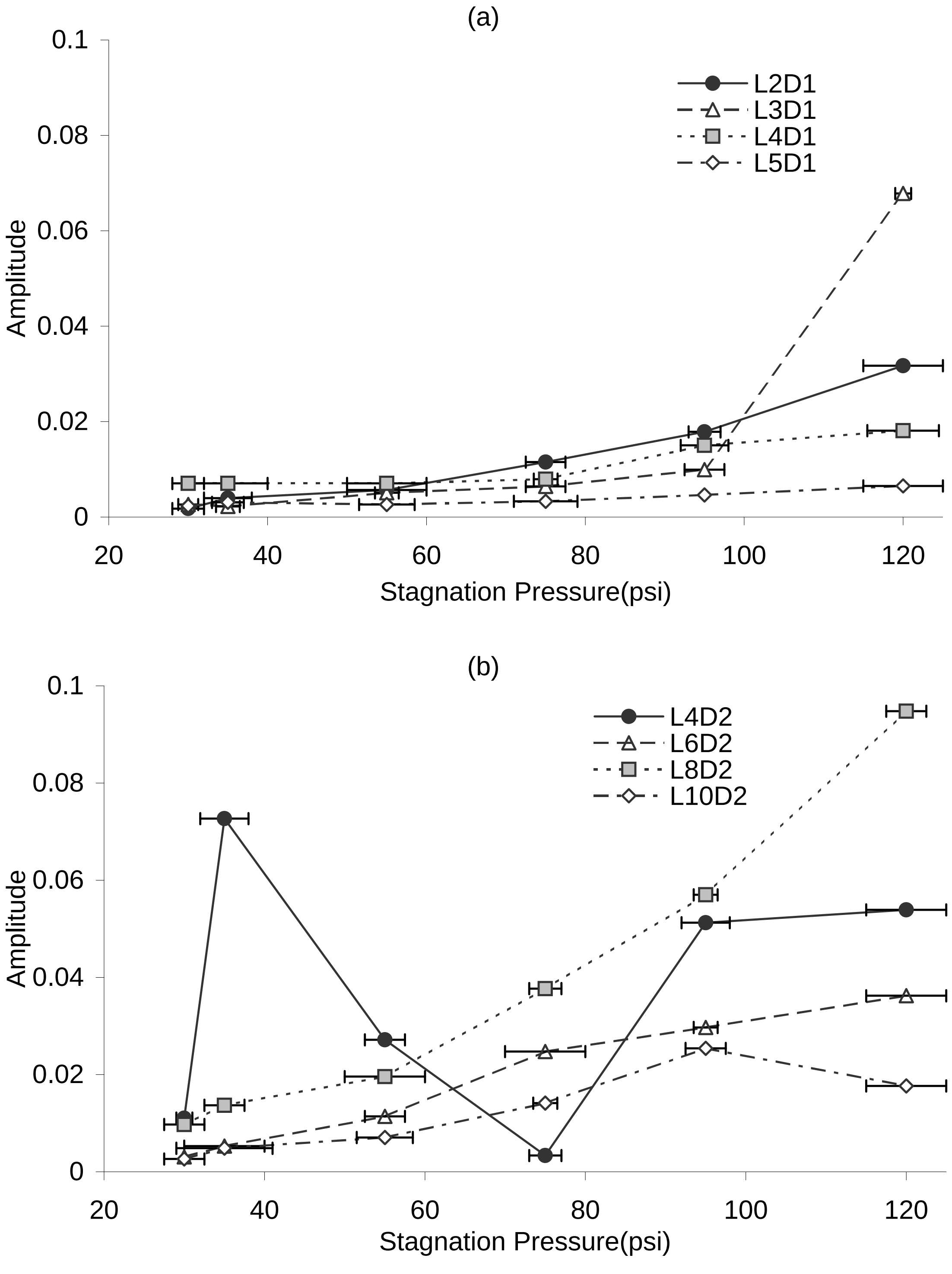

Figure 29. Spectral amplitude at peak frequency for (a) D/H=0.5 and (b) D/H=1.

Figure 29 shows the spectral amplitude at peak frequency of oscillation as a function of stagnation pressure both for shallow and deep cavities. Plot (a) depicting the amplitude variation for the shallow cavities, shows an increase in oscillation amplitude with the stagnation pressure. This could be attributed to the general increase in overall fluctuation level in the flowfield. Plot (b) of this figure gives a similar plot of amplitude variation with stagnation pressure for the deeper cavities with D/H=1.0. Here, except for the L4D2 cavity, all the other cavities show a similar trend to that observed in plot (a), Again the increase of the amplitude of oscillations with stagnation pressure could be related to the overall increase in the fluctuation level.

5. Helium Injection Studies

Qualitative mixing studies were conducted using Helium as the simulated fuel. Helium was chosen on the basis of fluid property and safety concern. Helium exhibits a similar density ratio as hydrogen or high-temperature hydrocarbon fuel mixing with air (Burnes et al [6]). Various fuel injection locations have been investigated in literature. Since only mixing studies were being carried out rather than flameholding tests, the helium injection point was chosen in the wake of the cavity so the coherent structures shed from the cavity would entrain the helium jet and enhance mixing. The practical application for such a fuel injection scheme would be as secondary fuel injected downstream of the cavity to control the fuel-air ratio (Burnes et al [6]).

5.1. Comparison of simulated fuel injection with and without cavity.

Figure 30 shows Schlieren images of the baseline case, on the left marked as (i) and the L4D1 cavity, on the right marked as (ii), when simulated fuel was injected in the wake of the cavity. In each of these cases, the airflow was maintained at a constant stagnation pressure of 30 psi and simulated fuel injection was performed at increasing stagnation pressures of 0 psi (no fuel injection), 30 psi, 45 psi, 65 psi and 115 psi as indicated in the figure. It can be seen that in (a), where no injection was performed, a few weak shocks appear in either case. Since the camera settings were different for cases (i) and (ii), the demarcation line drawn along the length of figure (i) shows the corresponding length downstream of the injection location that is visualized in case (ii).When simulated fuel was introduced into the flow as shown in (b), strong jet induced shocks appear upstream of the fuel injection point. It can be seen that this shock also changes the flow characteristics upstream of the injection point.

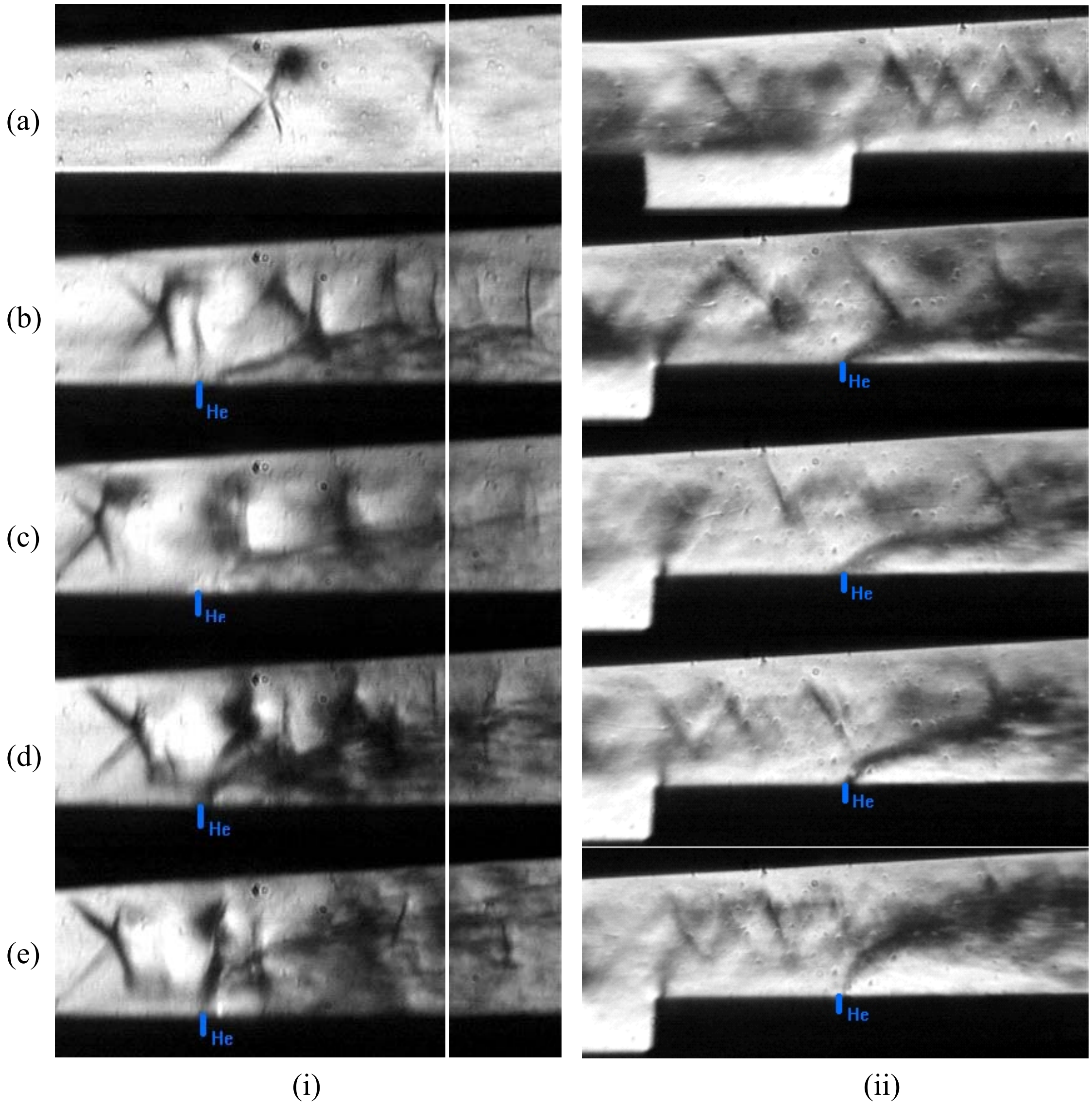

Figure 30. Comparison of helium injection in (i) without cavity, and (ii) L4D1 cavity at inlet air flow stagnation pressure of 30 psi and fuel injection pressures of (a) 0 psi, (b) 30 psi, (c) 45 psi, (d) 65 psi, (e) 115 psi.

Comparing the two images for case (b), it can be observed that while the helium jet appears as dark undisturbed streaks for the baseline case, the presence of the cavity makes the helium jet much more dispersed in the flow. This would translate into increase in the interfacial area between the fuel jet and air and thus enhance mixing. In case (c), the helium injection pressure was increased to 45 psi. It can be seen that the penetration depth of the injection stream is higher with the increase in the injection pressure for both the baseline and the cavity case. Again, comparing the image of the baseline with the cavity case shows increased dispersion in the cavity case. In cases (c) through (e), when the helium injection pressure was increased successively, a similar trend is observed. The penetration depth increased with increase in the fuel injection pressure for either cases and always, the cavity case showed increased spreading of the fuel jet into the supersonic airflow. This is a direct evidence of the effectiveness of the cavity resonance characteristics in mixing enhancement. Quantitative mixing studies would yield a measure of the effectiveness of this mechanism.

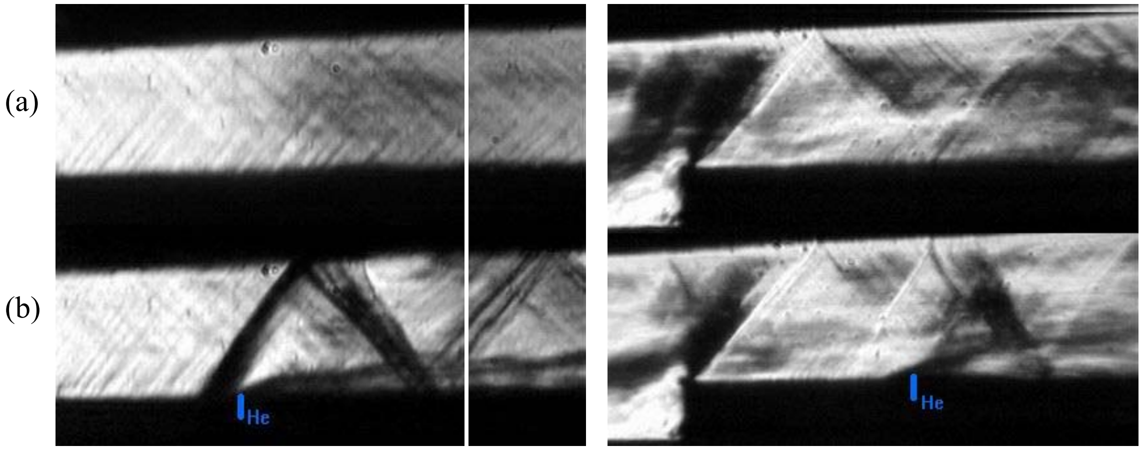

(i) (ii)

Figure 31. Comparison of helium injection in (i) without cavity, and (ii) L4D1 cavity at inlet air flow stagnation pressure of 115 psi and fuel injection pressures of (a) 0 psi, (b) 115psi.

Figure 31 shows a similar comparison for an airflow stagnation pressure of 115 psi and helium injection pressures of 0 psi (no injection) and 115 psi. Comparison of the case (a) with no helium injection shows that the baseline case has uniform shock pattern across the section viewed, while the image on the right with the cavity shows the shear layer characteristics and trailing edge expansion wave as discussed in the previous section. In case (b), helium is injected in the 115 psi airflow at a pressure of 115 psi. The baseline case clearly shows the strong jet induced shock and the helium jet trail with a rather slow spreading rate. On the other hand, when the cavity is introduced as in figure (ii), the strength of the jet induced shock appears reduced and the spreading of the helium jet into the airstream increases. While the preliminary studies of the cavity with helium injection indicates that the spreading rate is increased due to the resonance mechanism, further quantitative and qualitative study is required to establish clearly how the cavity affects the mixing process.

5.2. Variation of airflow stagnation pressure.

In the previous subsection, Schlieren images of flow with and without cavities were compared for two sets of initial conditions. Here, attempt has been made to explore the effect of injection pressure downstream of the cavity by studying the Schlieren images of the duct with varying helium injection pressure for each airflow stagnation pressure. Figure 32 and figures 45 through 49 in Appendix A2, show Schlieren images of the helium injection in the wake of the cavities for varying airflow and helium stagnation pressures. Though no quantitative mixing information could be gleaned from the set of data acquired, the study was aimed at demonstrating the fuel injection process and the flow field created in the wake of the cavity due to the transverse injection process. The set of data presented here gives an idea of the type of fuel injection that would be required and the extent to which transverse injection downstream of the cavity would affect mixing.

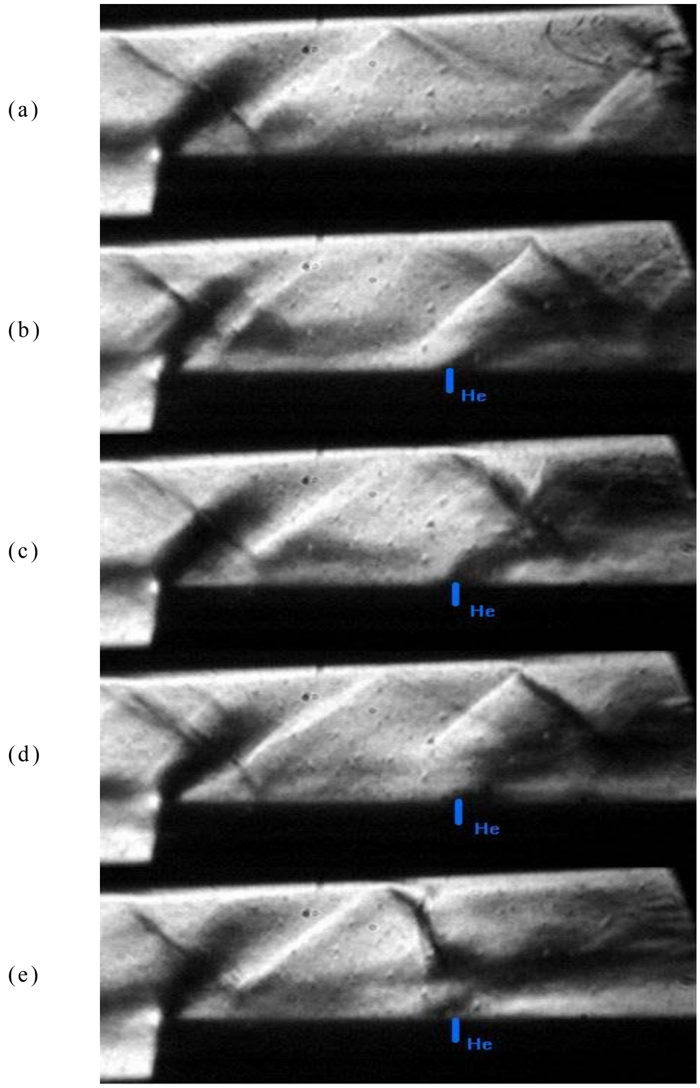

Figure 32. Airflow at 35 psi for helium injection pressures (a) 0 psi, (b) 35 psi, (c) 65 psi, (d) 90 psi, (e) 115 psi.

Figure 32 shows Schlieren images of the L4D1 cavity with an airflow stagnation pressure of 35 psi subjected to various helium injection pressures of 0 psi (no injection) to 115 psi. The distinctive features visible in the image (a) without helium injection are 1) a part of the shear layer impinging on the trailing edge of the cavity, 2) the compression wave appearing at the trailing edge of the cavity and 3) a bouncing oblique shock train probably created at the leading edge of the cavity. Case (b) shows helium injected at 35 psi, which is equal to the stagnation pressure of the airflow for this case. It can be seen that the flow structures upstream of the helium injection point have been modified from the previous image. A jet induced oblique shock is created just upstream of the helium injection point and this shock continues to travel downstream bouncing off the upper wall. As indicated in the previous subsection, the increase in stagnation pressure of the jet causes increased penetration inside the airflow. The image (c) in the sequence shows helium injected at a pressure of 65 psi, when the airflow stagnation pressure is maintained at 35 psi. In this image, the features are similar to the previous case, except that the jet-induced shock is not made visible prominently, though the wave reflection created as a result of the jet induced shock is clearly visible. Again, helium penetration inside the air stream is deeper due to higher stagnation pressure of the helium injected. Also, the coherent structures expected to be shed from the cavity can be faintly observed in this image. Image (d) helium injected at a stagnation pressure of 90 psi while the airflow stagnation pressure is maintained at 35 psi. While, there are not many distinct differences from the previous images, the helium penetration inside the airflow is higher.

Figure 45 through Figure 49 in Appendix A2 show the complete set of Schlieren images for airflow stagnation pressures from 35 psi 120 psi with varying helium injection pressures. The flow features were similar to the ones observed in the first case. As the airflow stagnation pressure is increased, the helium jet penetrates lesser inside the airflow due to lower relative injection pressure. In the actual design of the fuel injection scheme to cavity based mixing enhancement device, a optimum range of stagnation pressure would be chosen depending on the flight conditions.

6. Summary and Conclusions

Scramjet combustion has been regarded as the preferred mode for the hypersonic flight regimes. In such a combustor, the flow entering the combustor is maintained supersonic through out the length of the combustor. At such high Mach numbers inside the combustor, fuel-air mixing becomes a primary limiting factor in the overall combustion process. The effect of compressibility is found to have an adverse effect on mixing and an efficient device is sought which will augment the mixing process. It has been shown that flow-induced cavity resonance can be a promising technique to enhance supersonic mixing in propulsion devices. In this thesis, it is attempted to analyze the effectiveness of this mechanism under various off-design conditions. Also, the mixing device in a typical Scramjet would be expected to operate over a wide range of flight speeds, so it is important to establish the robustness of such a mechanism. Thus, a parametric investigation was performed in which the stagnation pressure was varied from 35 psi to 120 psi and the acoustic characteristics of various cavities were examined. The nozzle was designed for Mach 2.0 exit flow, but the flow facility available did not support Mach 2.0 flow at the nozzle exit. Thus, the nozzle essentially operated at an off-design condition. Spark Schlieren flow visualizations, unsteady pressure measurements and spectral analysis of the measurements were carried out to characterize the flow field in the cavity.

The Schlieren images of the flow field over cavities revealed a strong interaction between leading edge expansion wave and boundary layers. The wave-boundary layer interaction was also affected by downstream conditions, which changed the Mach number of the flow entering the leading edge of the cavity. Also, the analysis of the nozzle throat revealed complexities of the flow upstream of the cavity section. It was found that the characteristic of the flow at the nozzle throat was changed considerably with stagnation pressure. The unsteadiness of the leading edge pressure wave in the cavity was also analyzed. Despite such complexities in the upstream flow field, the flow-induced cavity resonance mechanism was fairly robust producing large-amplitude coherent fluctuations in all cases of selected cavity configurations. For certain cases, however, the dominant frequency of oscillations was shown to change as a function of stagnation pressure. The effect of such mode hopping behavior on quantitative result of mixing enhancement warrants further investigation. Also, the prediction of mode hopping behavior with the change in the cavity and flow parameters need further study. A demonstration of the extent to which analytical techniques can assist in prediction of the frequencies of oscillation was also attempted by comparing the results of this experimental study with those obtained by earlier investigators (Rossiter [33] and Heller et al [24]) under pressure-matched conditions. It was found that the experimental results were in close agreement with the predicted ones.

In the next set of studies, helium was injected downstream of the cavity, and comparisons were made between the cases with and without helium injection. Schlieren images showed that the presence of the cavity increased the depth of penetration and spreading rate of the helium jet into the air stream. Also, the helium injection pressure was changed and the effect on penetration depth and modifications in the flow structures were analyzed. Though these studies were useful in analyzing the flow field characteristics due to helium injection, further quantitative mixing studies would help a great deal in assessing the effectiveness of the cavity resonance mechanism.

Appendix A1 - Flow visualization results

I. Shallow cavities

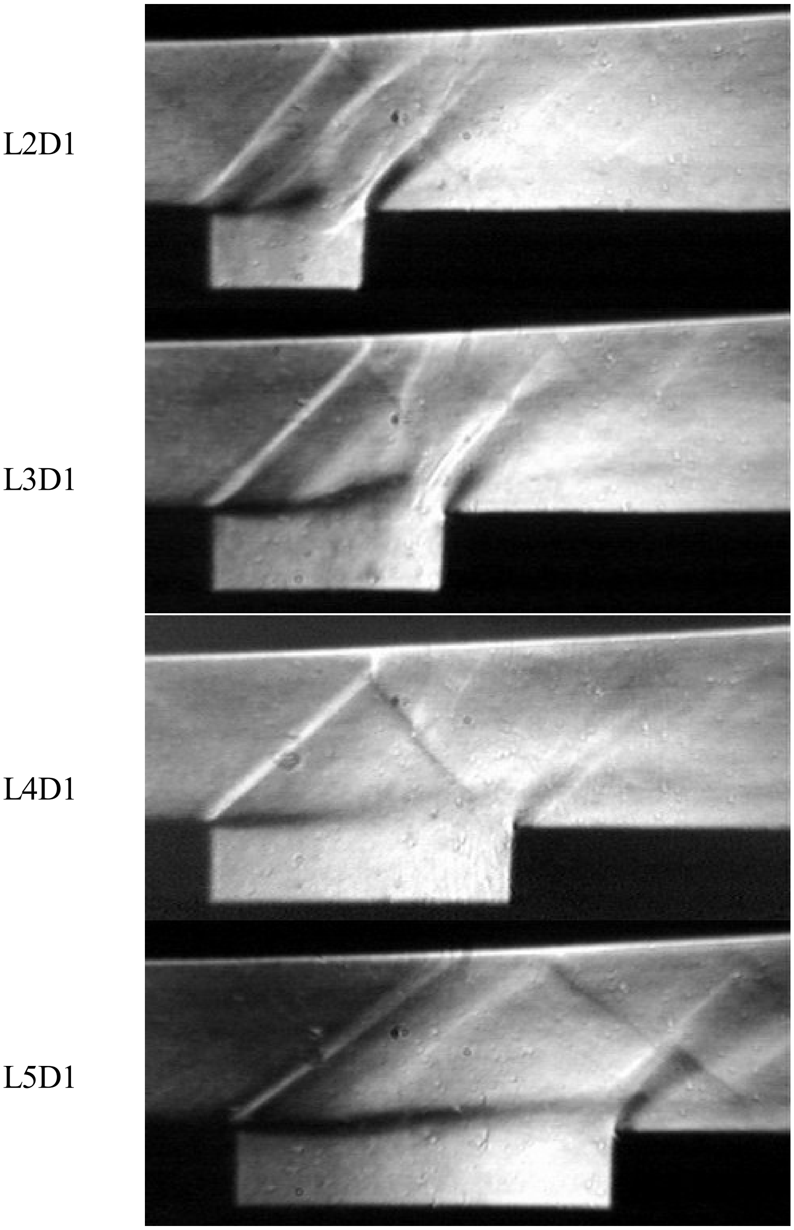

Figure 33. Schlieren images of shallow cavities at 35 psi.

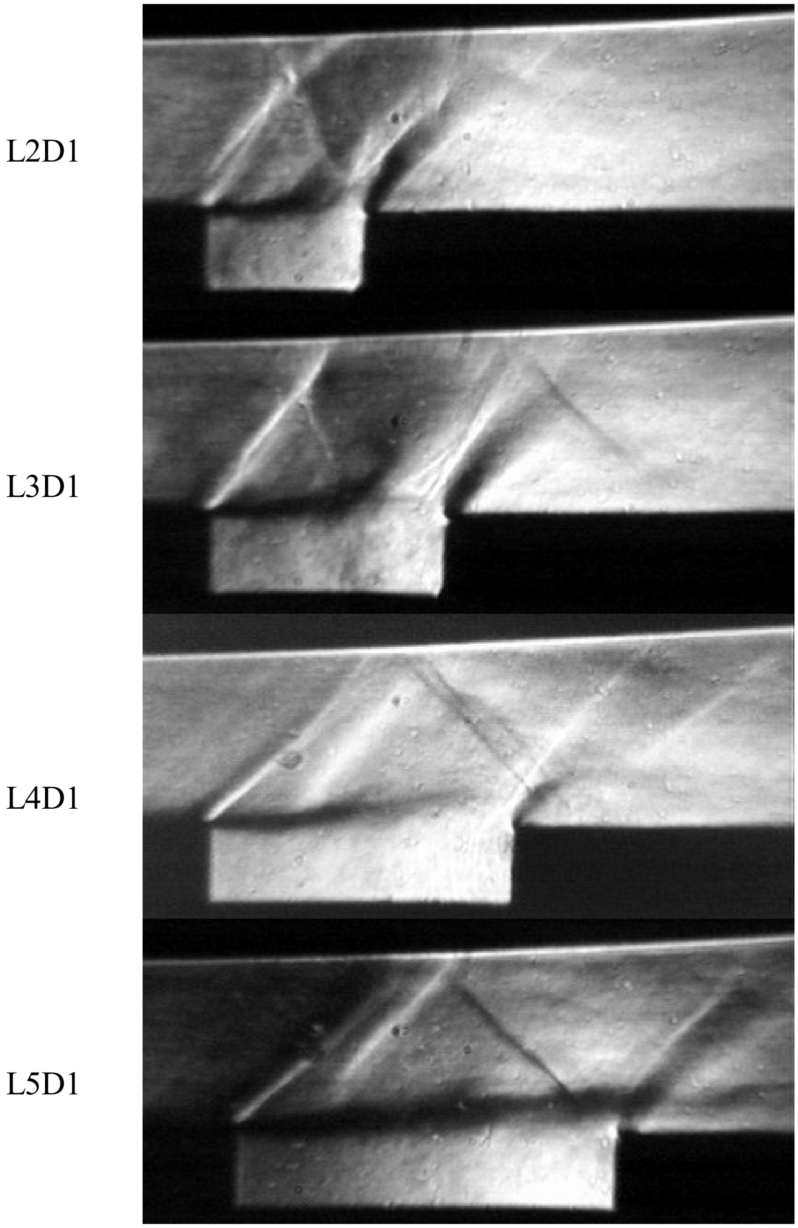

Figure 34. Schlieren images of shallow cavities at 55 psi.

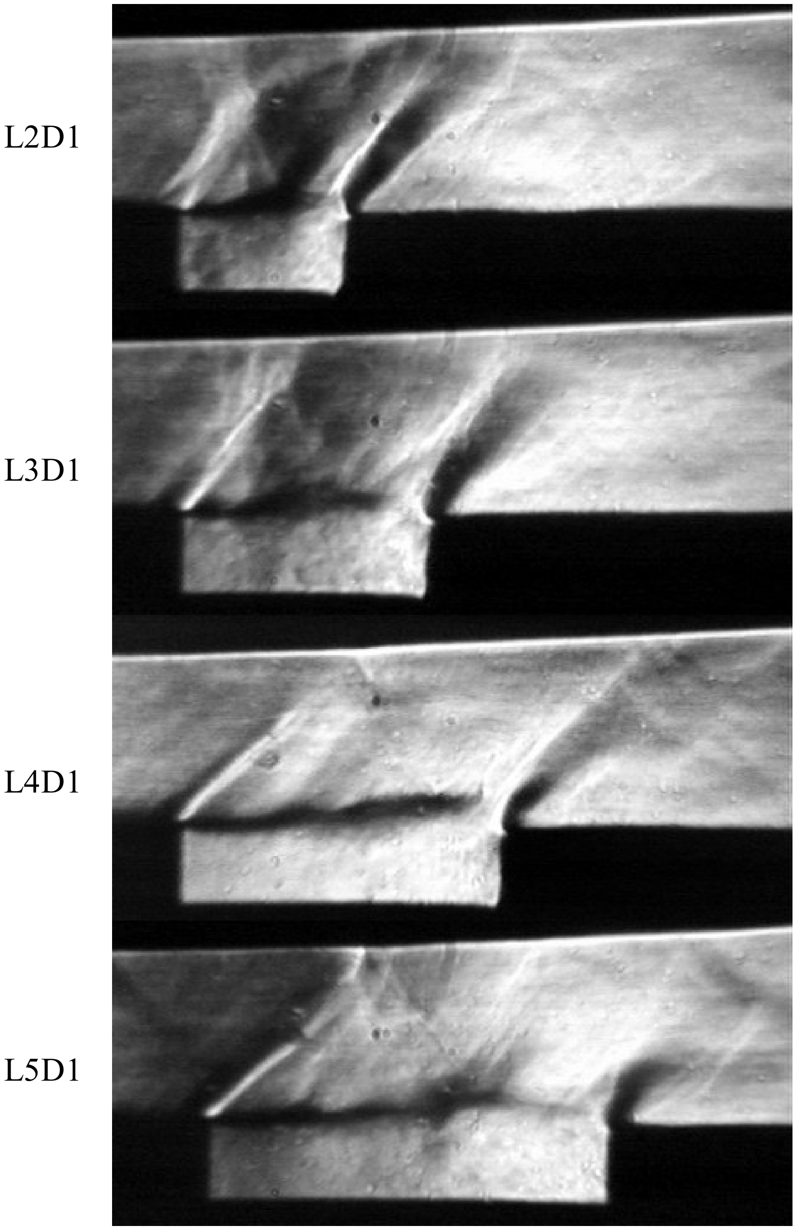

Figure 35. Schlieren images of shallow cavities at 75 psi.

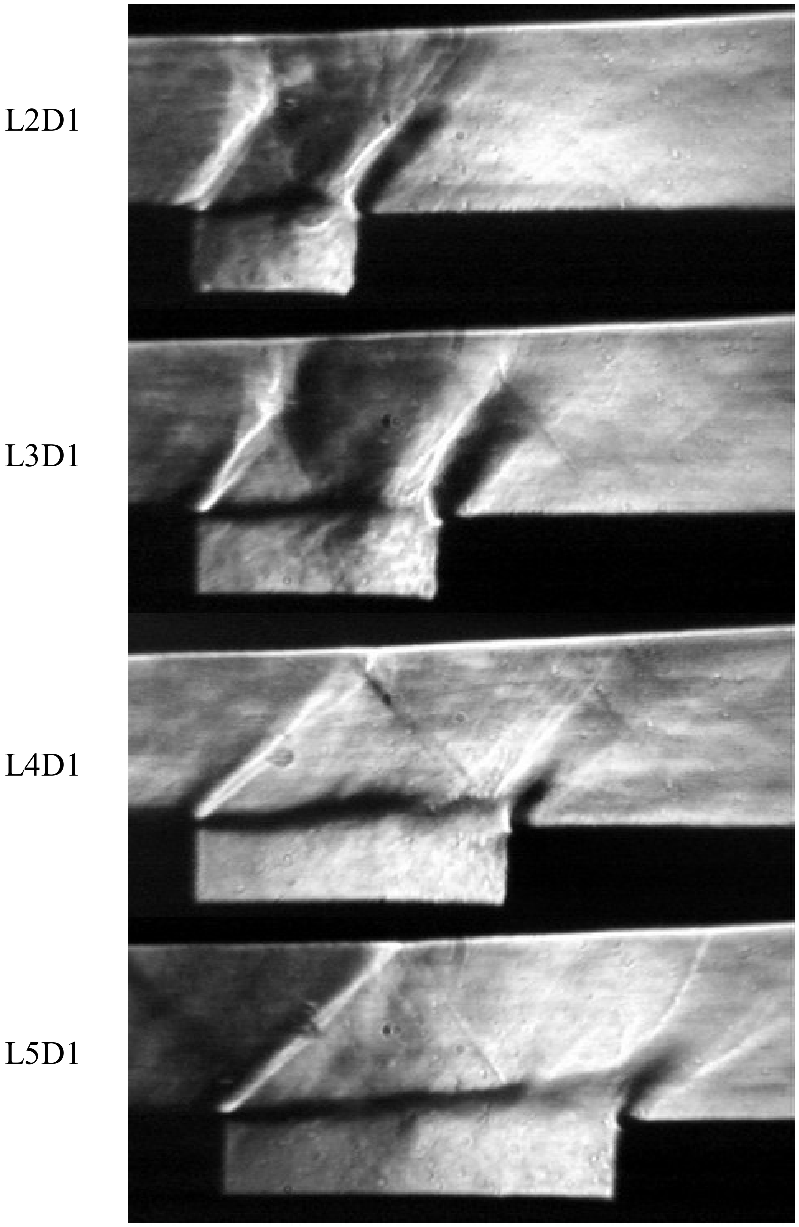

Figure 36. Schlieren images of shallow cavities at 95 psi.

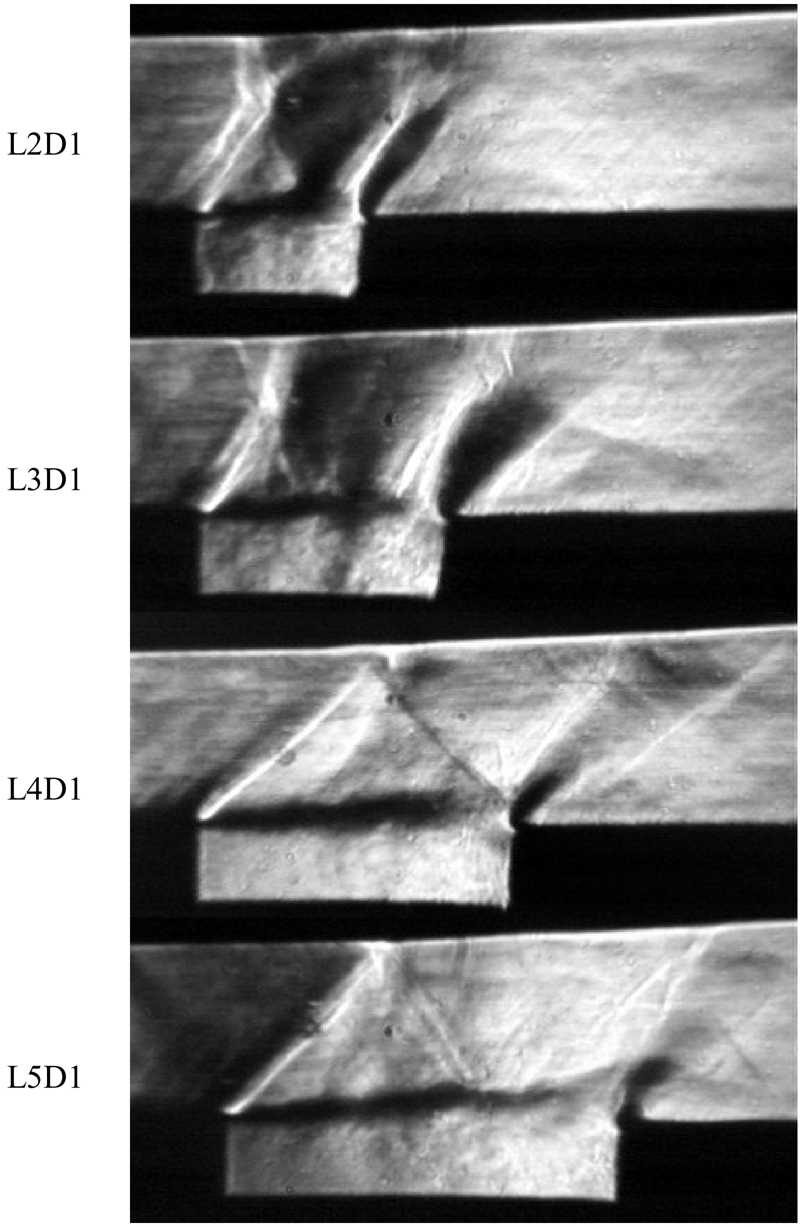

Figure 37. Schlieren images of shallow cavities at 120 psi.

II. Deep cavities

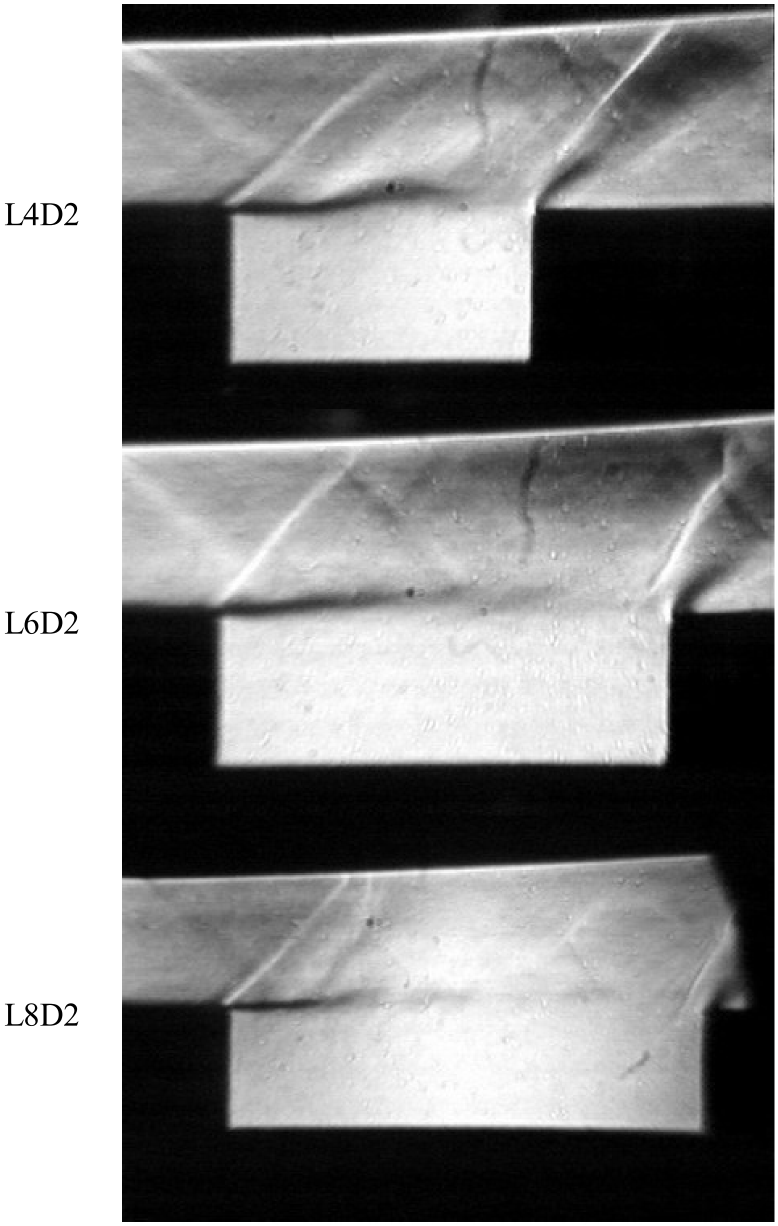

Figure 38. Schlieren images of deep cavities at 35 psi.

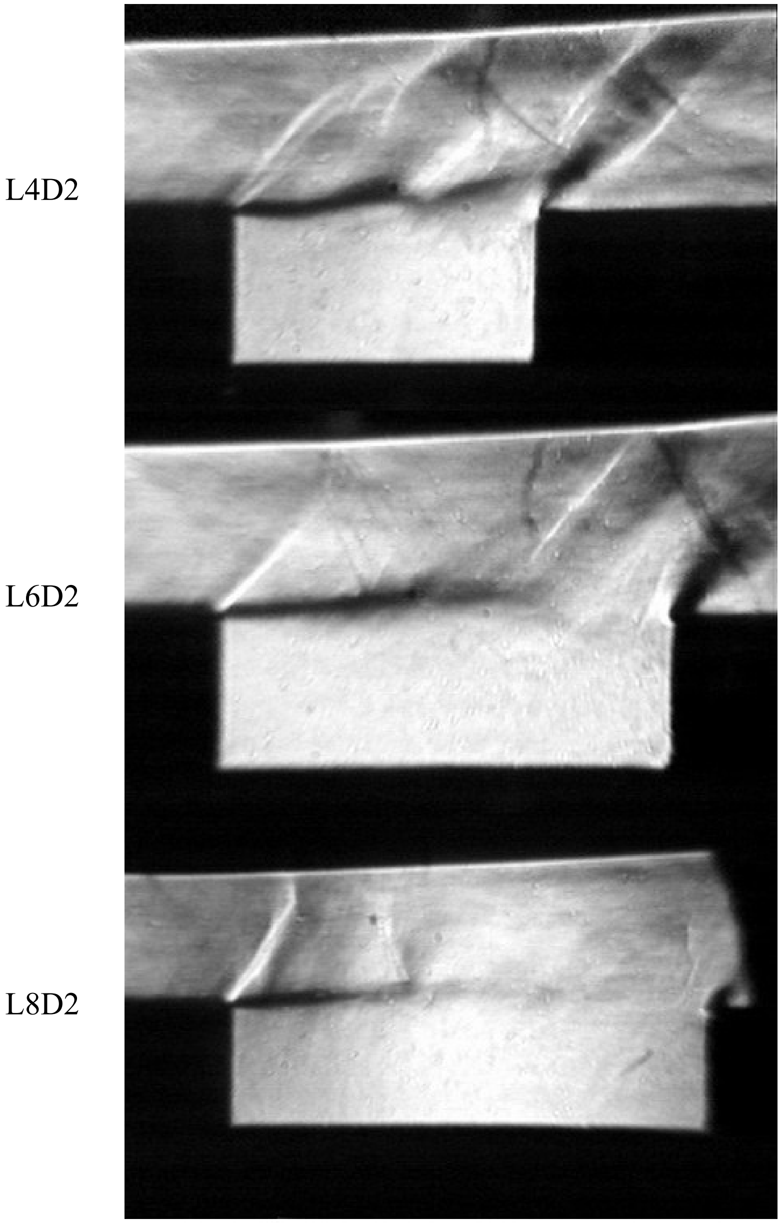

Figure 39. Schlieren images of deep cavities at 55 psi.

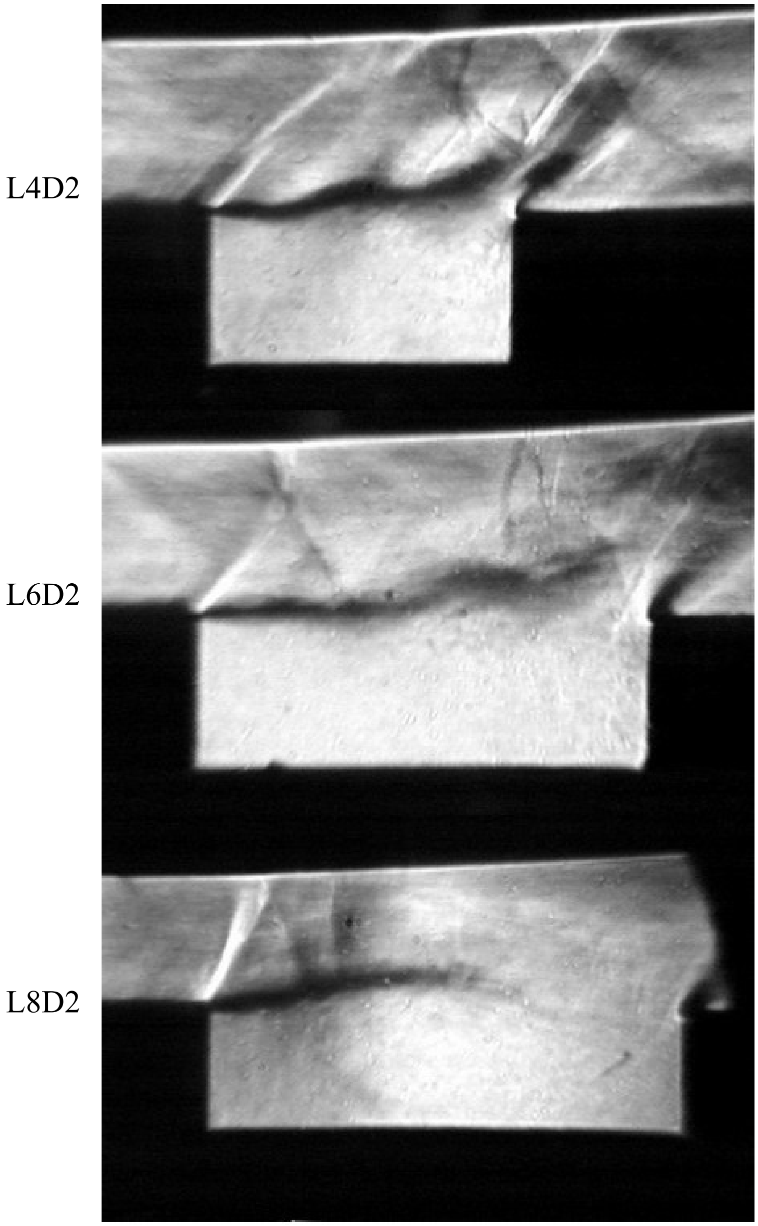

Figure 40. Schlieren images of deep cavities at 75 psi.

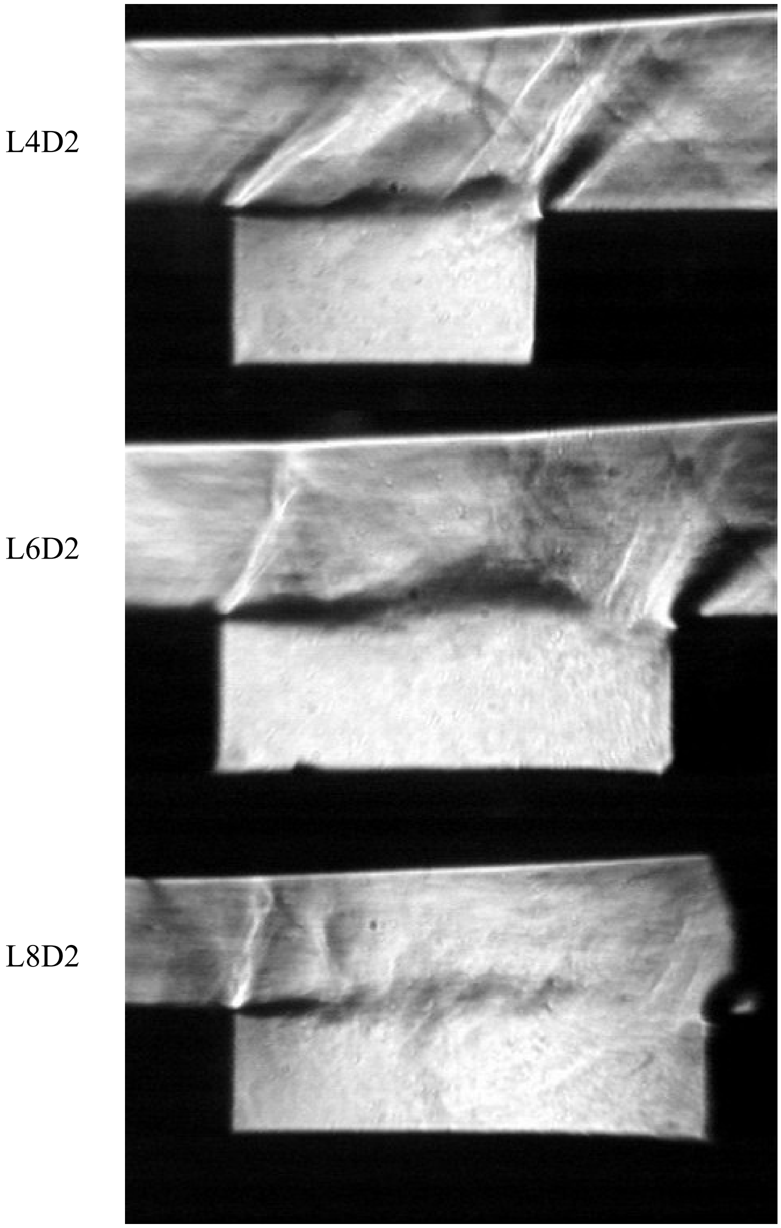

Figure 41. Schlieren images of deep cavities at 95 psi.

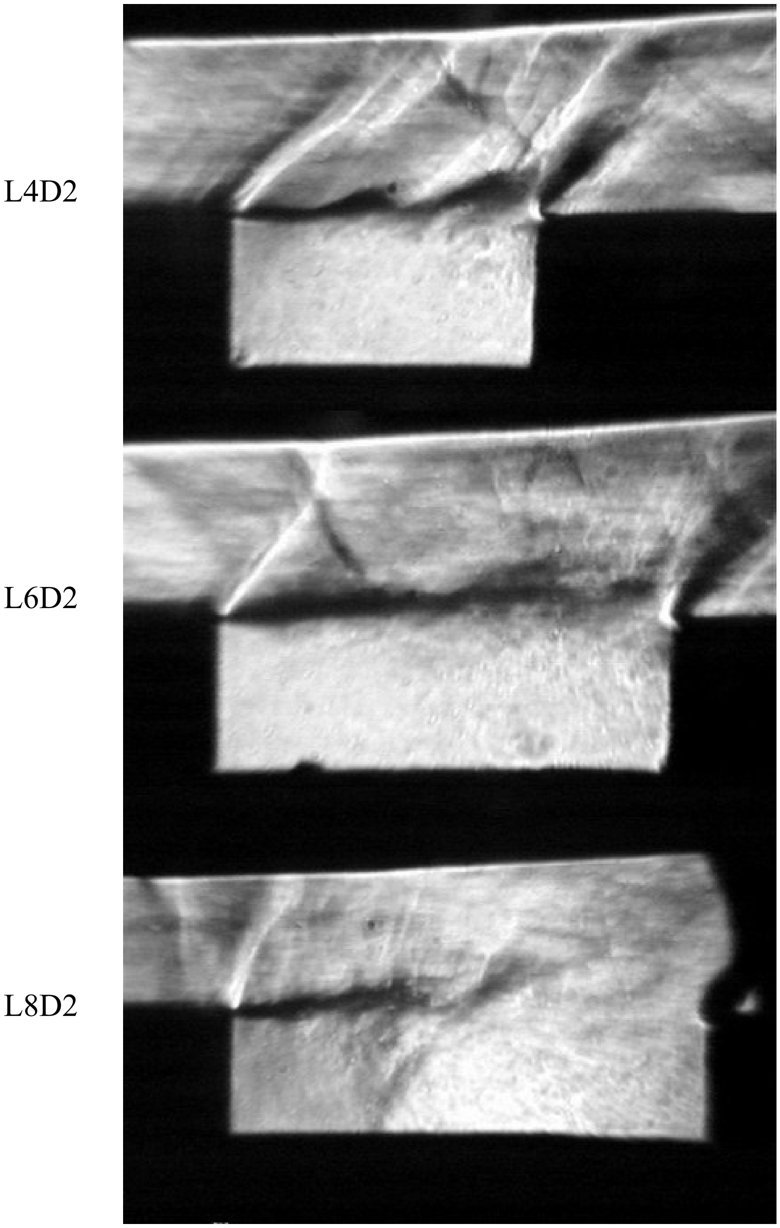

Figure 42. Schlieren images of deep cavities at 120 psi.

III. Leading edge shock oscillations

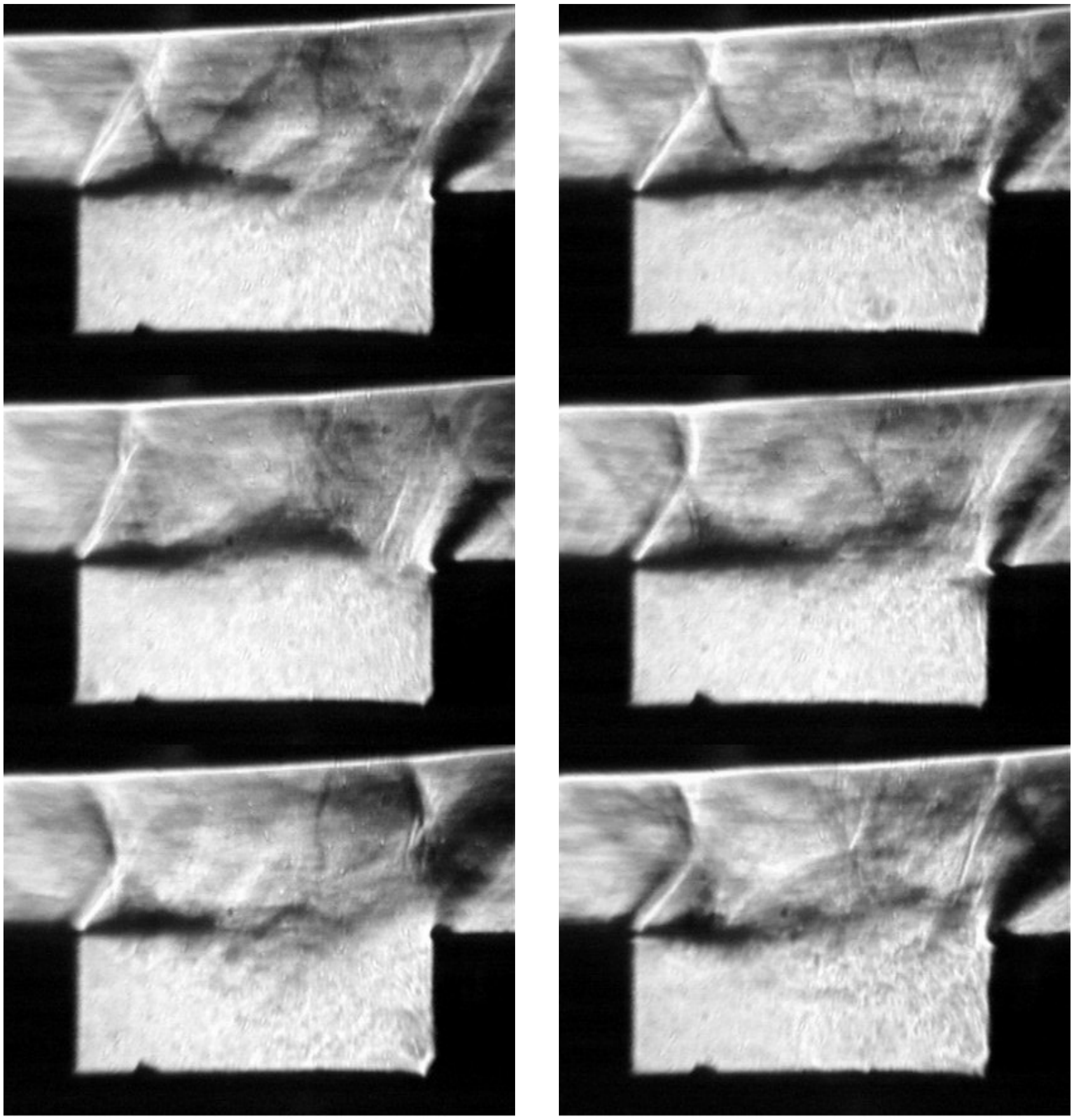
(a) (b)

Figure 43. Shock oscillations in L6D2 cavity at (a) 95 psi, (b) 120 psi

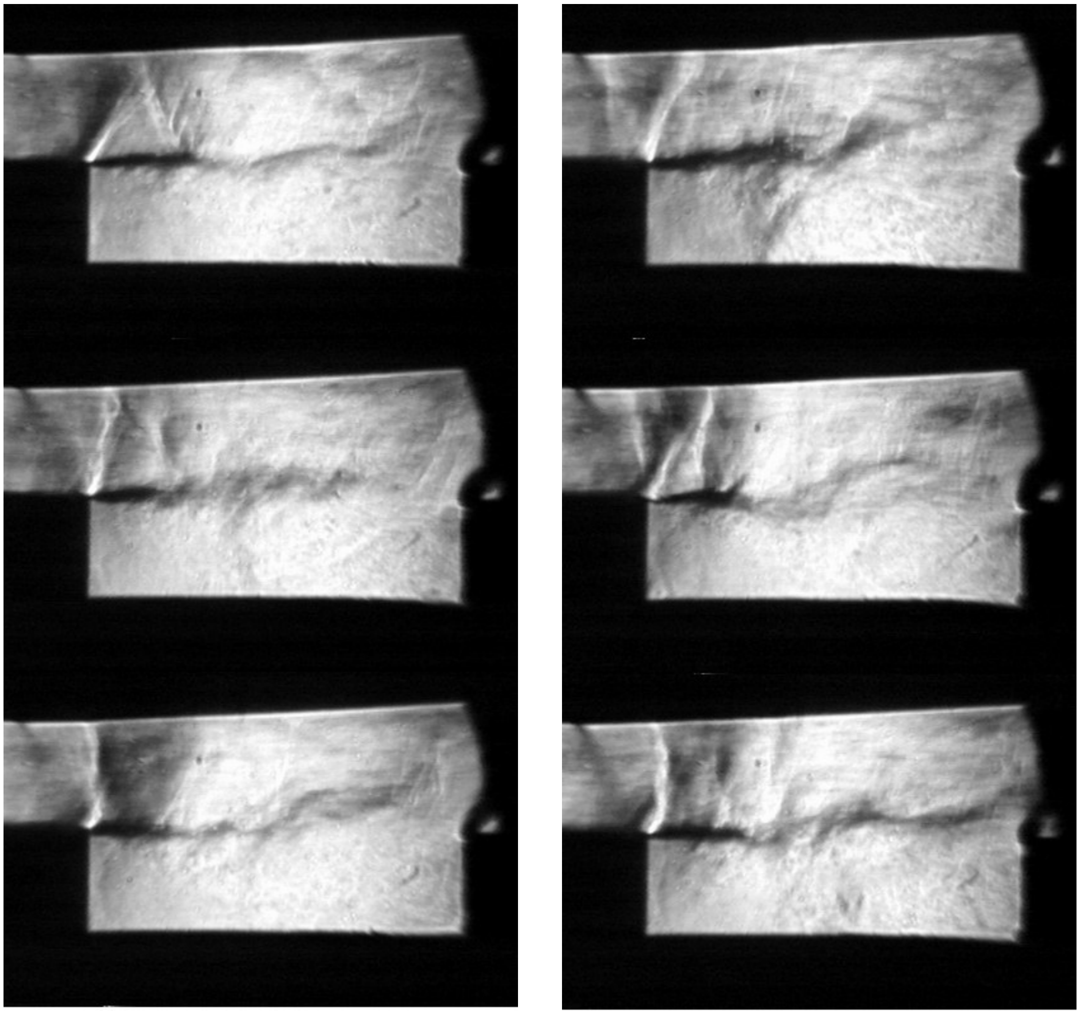

(a) (b)

Figure 44. Shock oscillations in L8D2 cavity at (a) 95 psi, (b) 120 psi

Appendix A2 – Helium injection studies

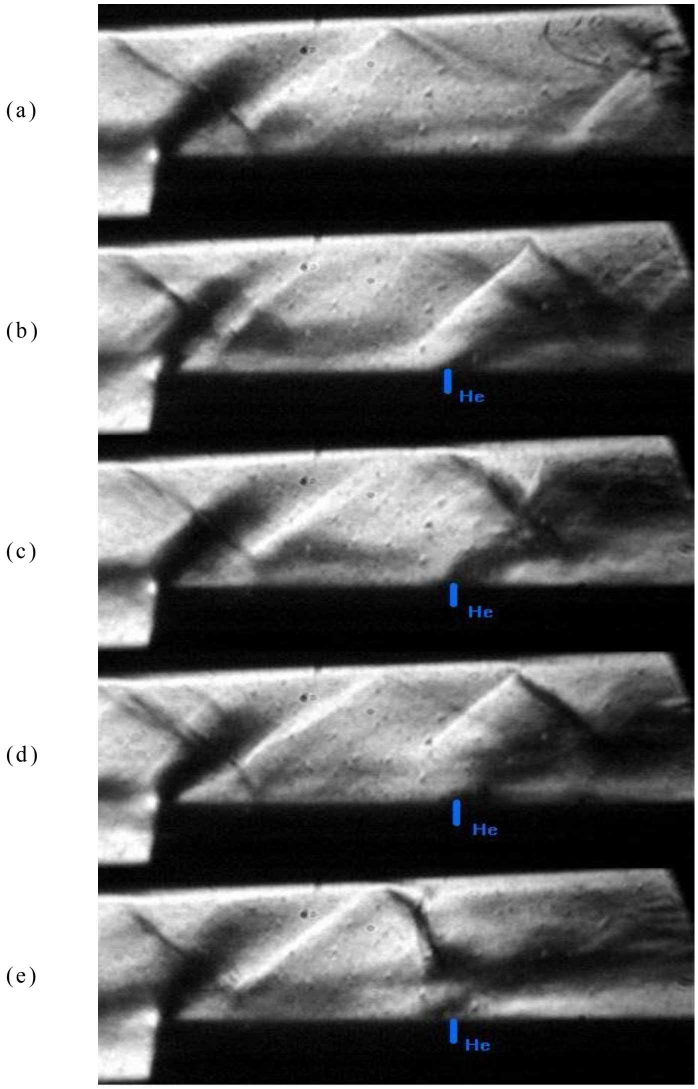

Figure 45. Airflow at 35 psi for helium injection pressures (a) 0 psi, (b) 35 psi, (c) 65 psi, (d) 90 psi, (e) 115 psi.

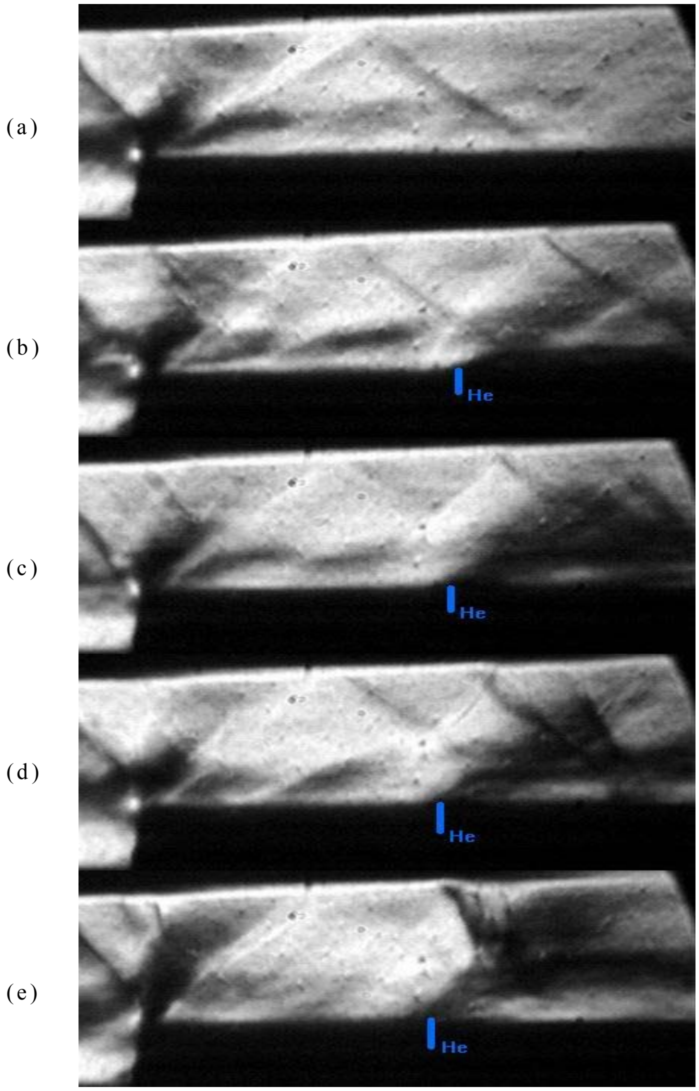

Figure 46. Airflow at 55 psi for helium injection pressures (a) 0 psi, (b) 35 psi, (c) 65 psi, (d) 90 psi, (e) 115 psi.

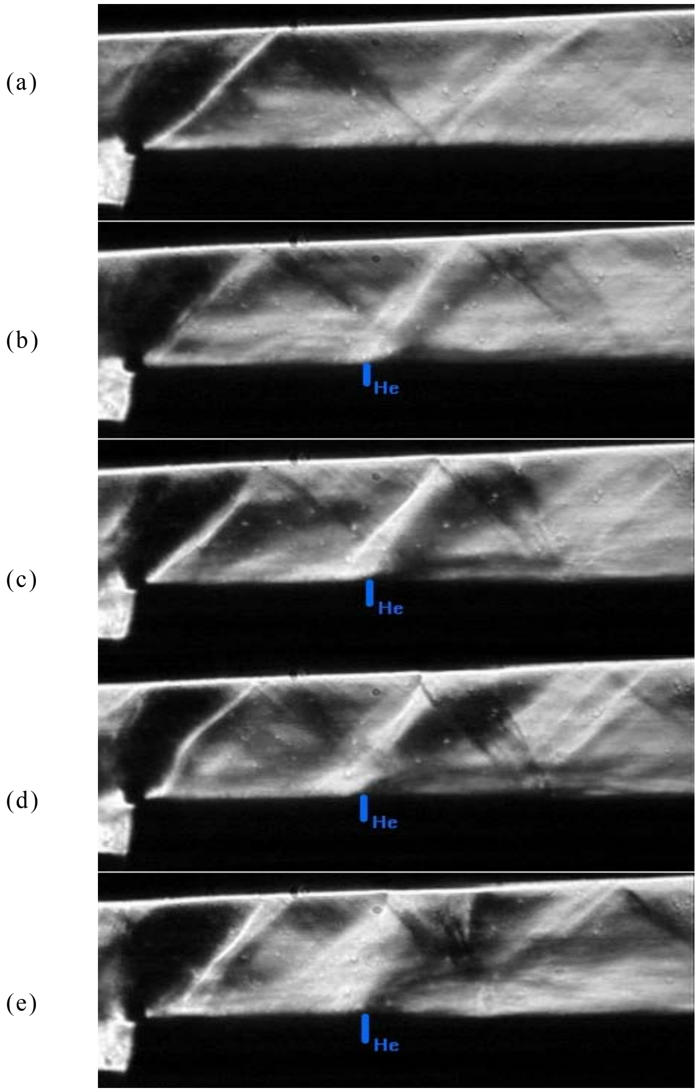

Figure 47. Airflow at 75 psi for helium injection pressures (a) 0 psi, (b) 35 psi, (c) 65 psi, (d) 90 psi, (e) 115 psi.

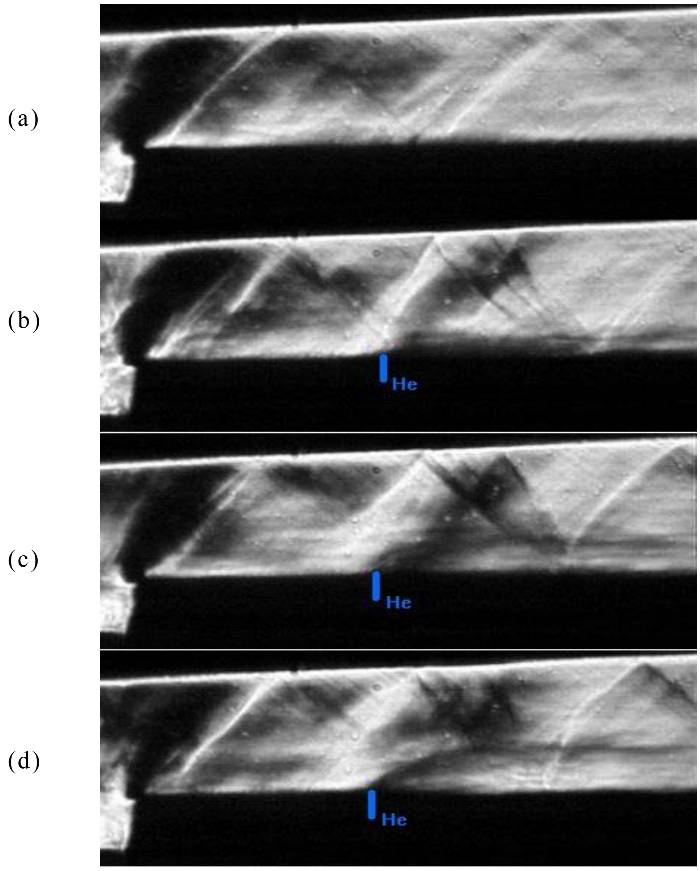

Figure 48. Airflow at 95 psi for helium injection pressures (a) 0 psi, (b) 65 psi, (c) 90 psi, (d) 115 psi.

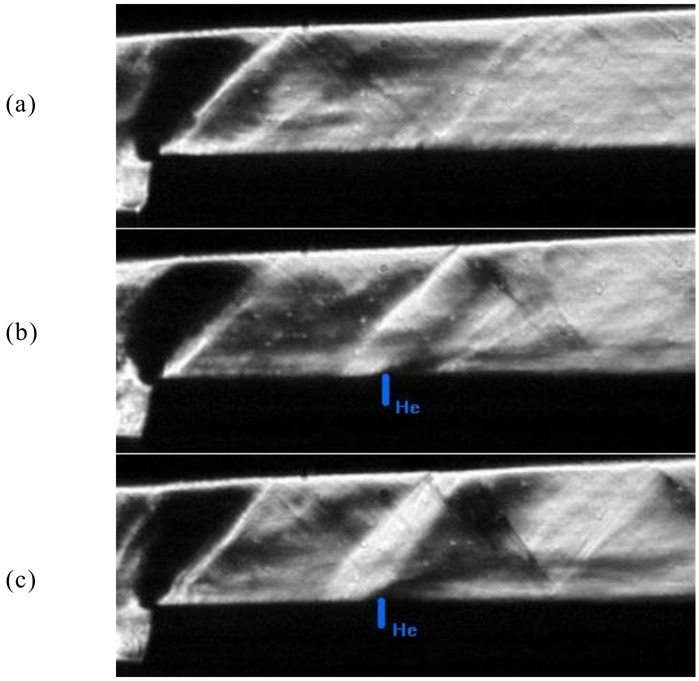

Figure 49. Airflow at 115 psi for helium injection pressures (a) 0 psi, (b) 65 psi, (c) 115 psi.

Appendix B1 - Unsteady pressure spectra

I. Shallow cavities

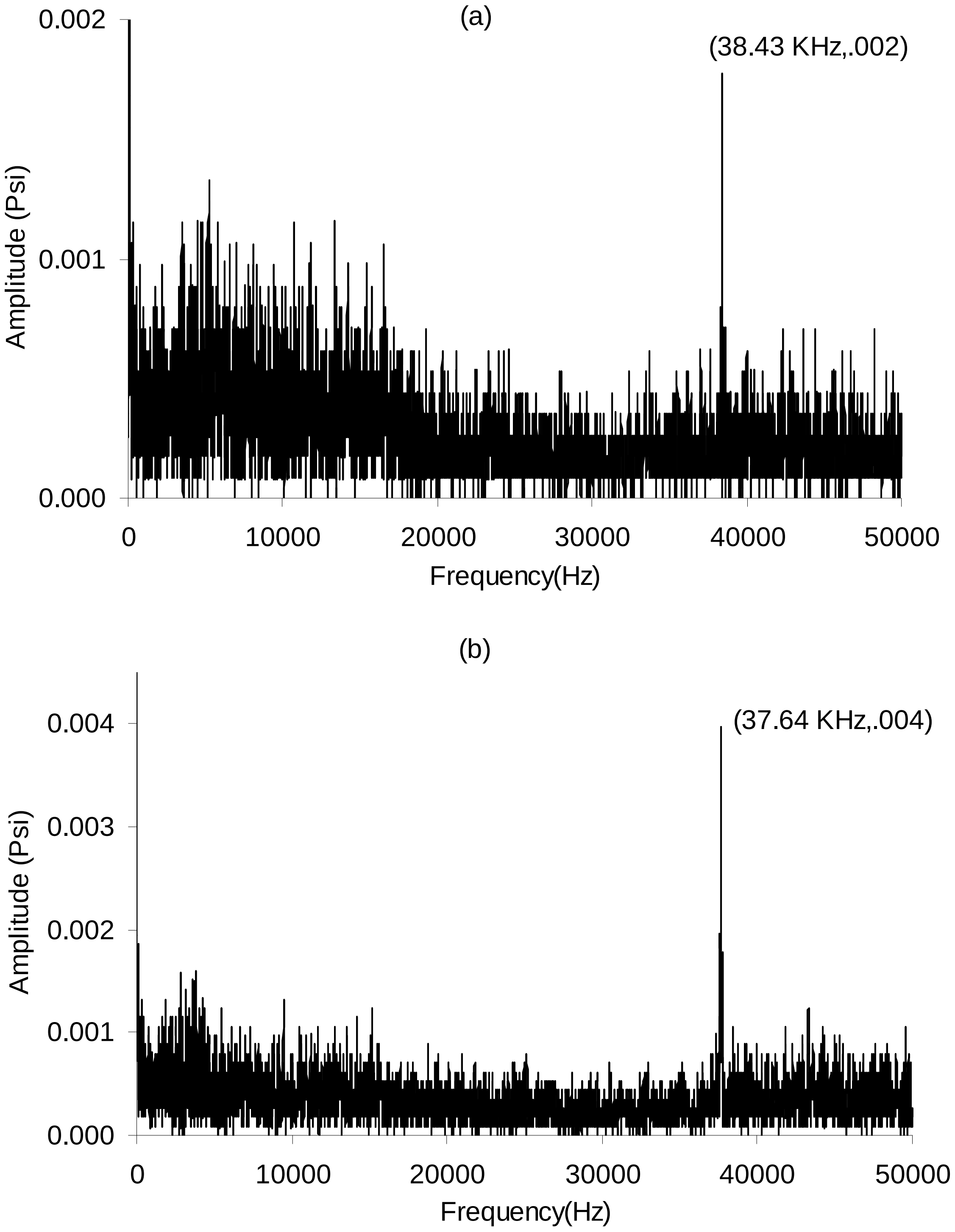

Figure 50(i). L2D1 cavity at upstream stagnation pressures of (a) 30 psi, (b) 35 psi.

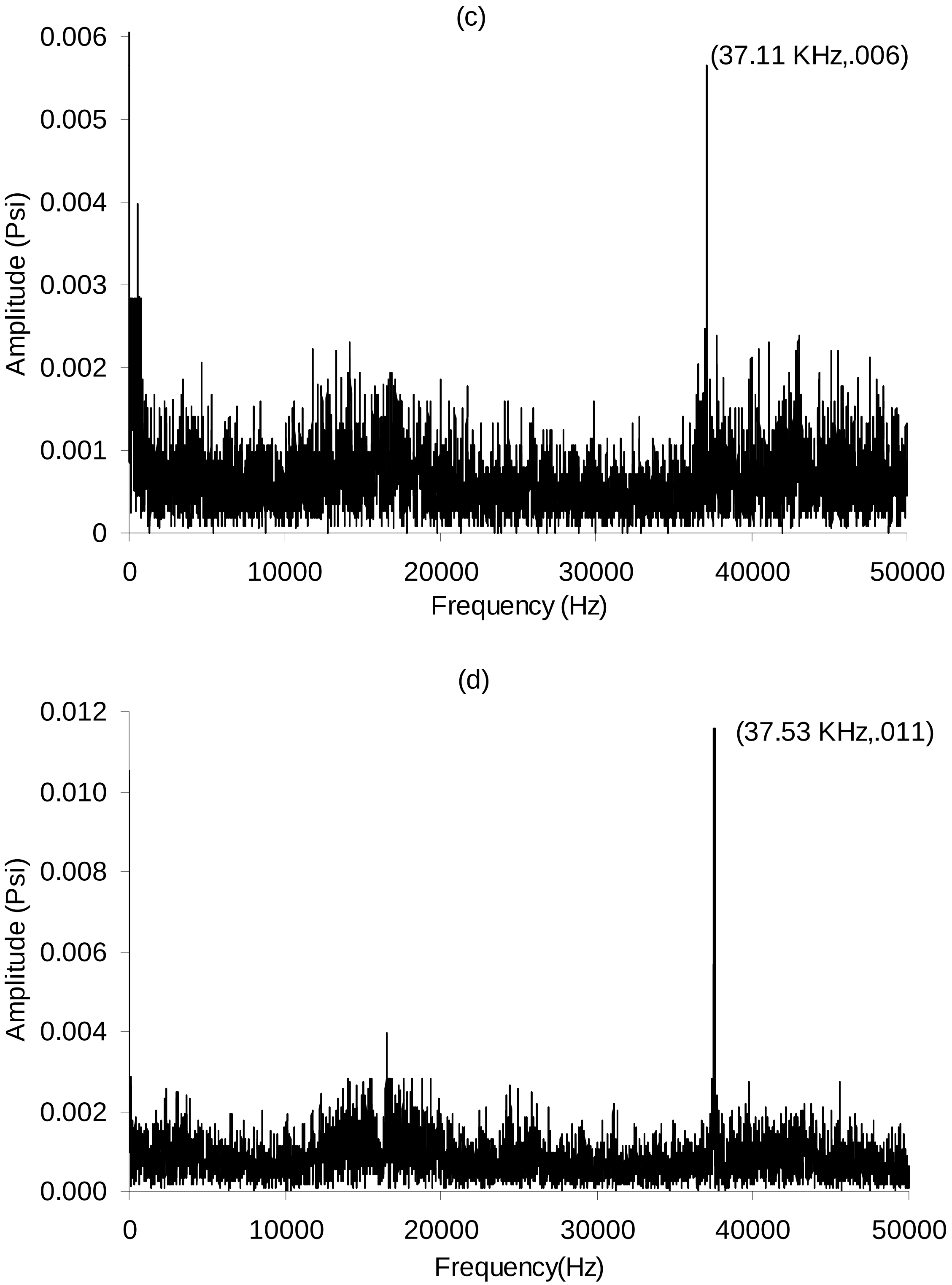

Figure 50(ii). L2D1 cavity at upstream stagnation pressures of (c) 55 psi, (d) 75 psi.

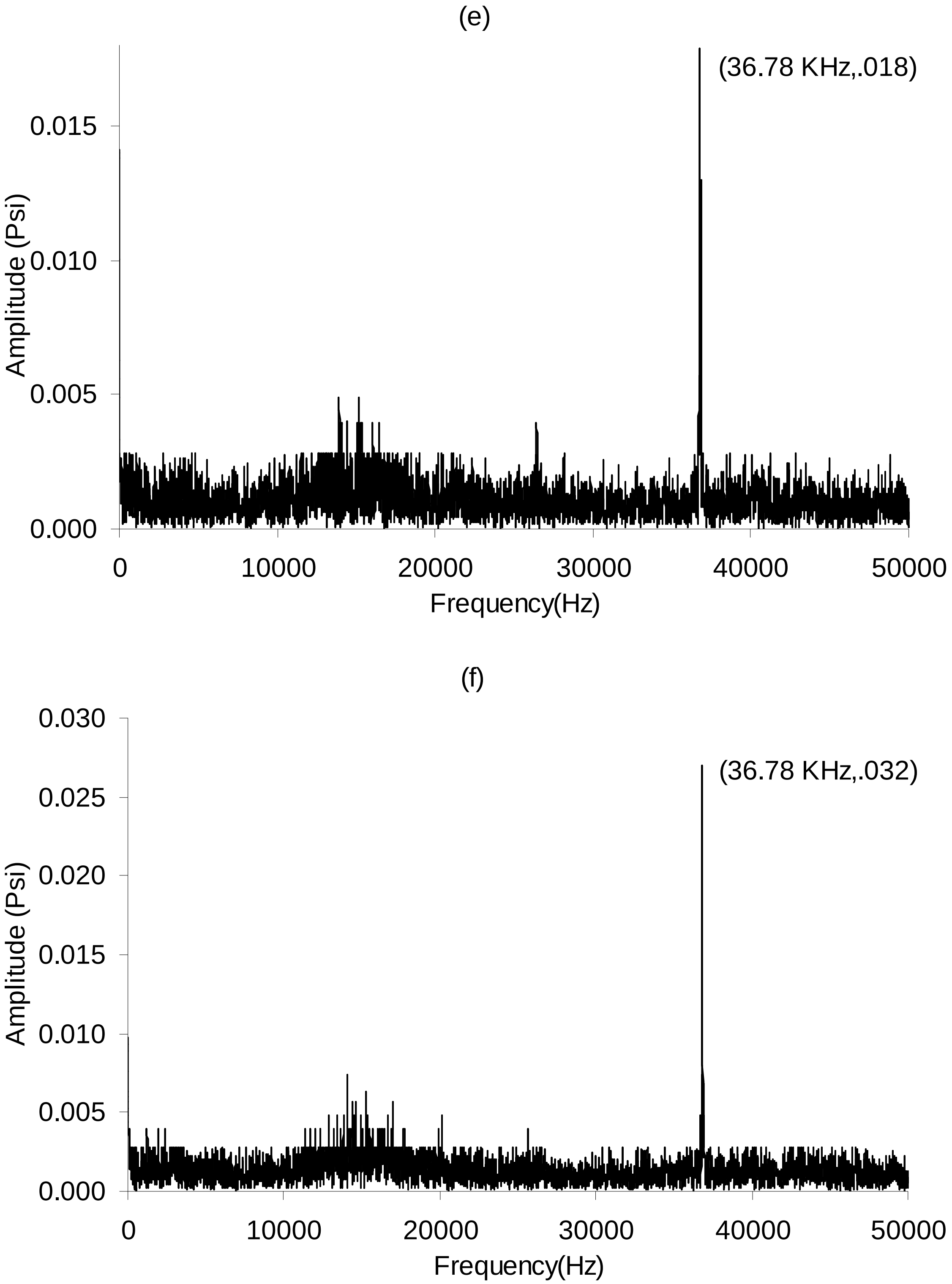

Figure 50(iii). L2D1 cavity at upstream stagnation pressures of (e) 95 psi, (f) 120 psi.

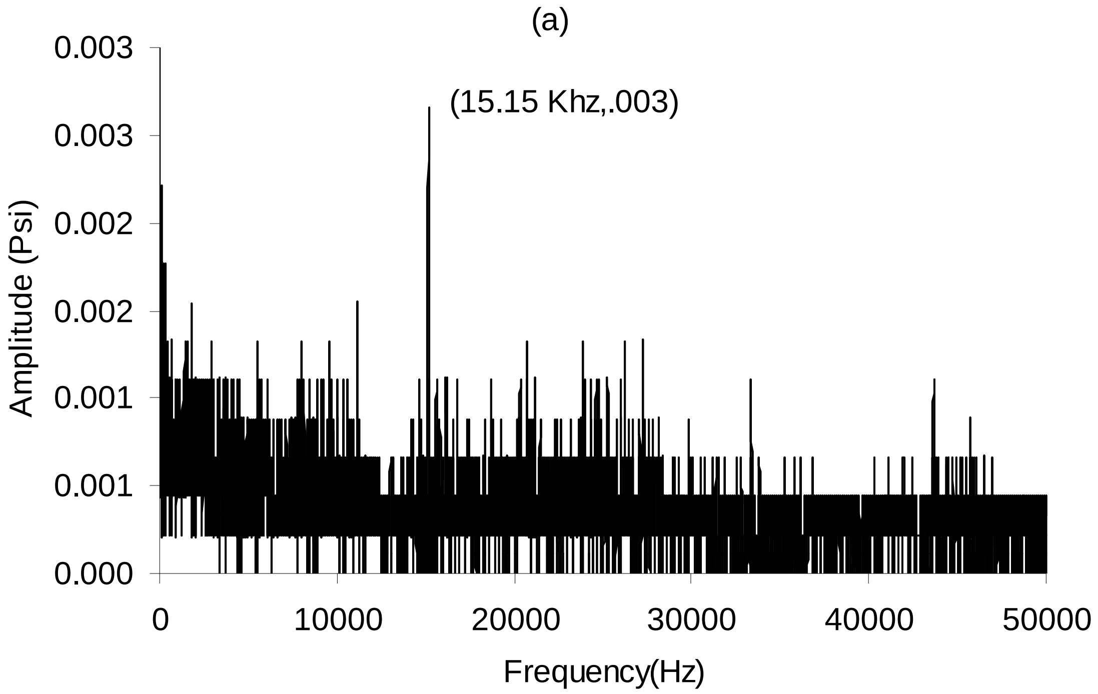

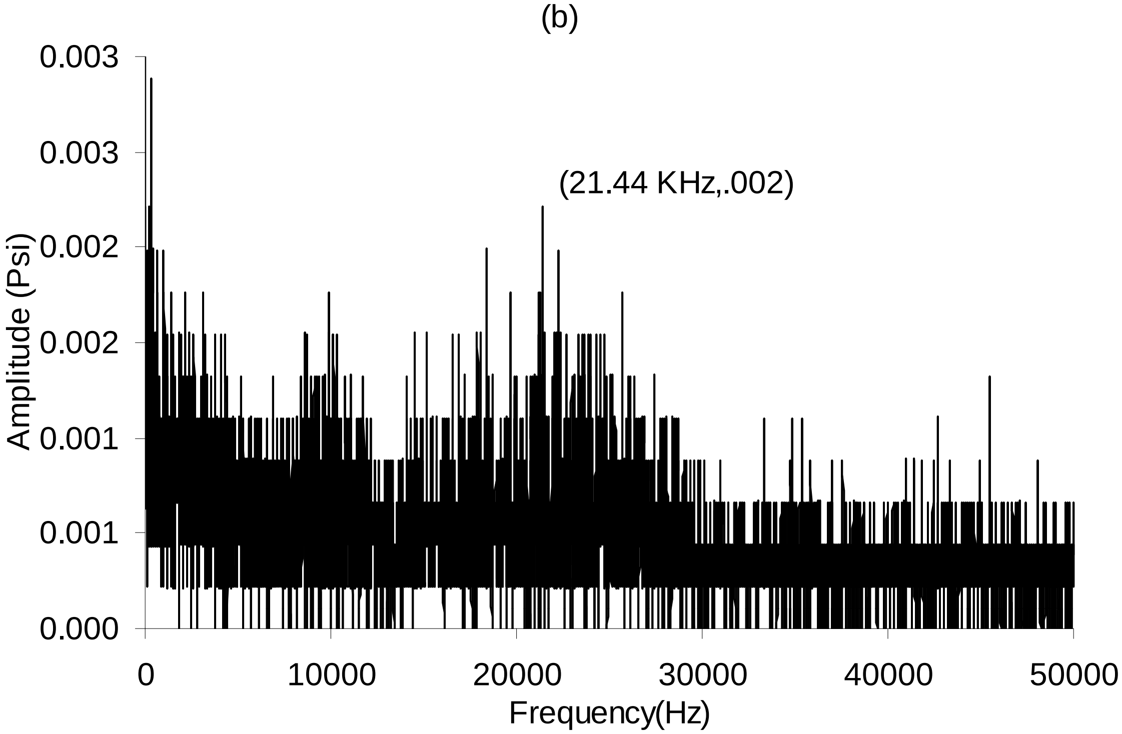

Figure 51(i). L3D1 cavity at upstream stagnation pressures of (a) 30 psi, (b) 35 psi.

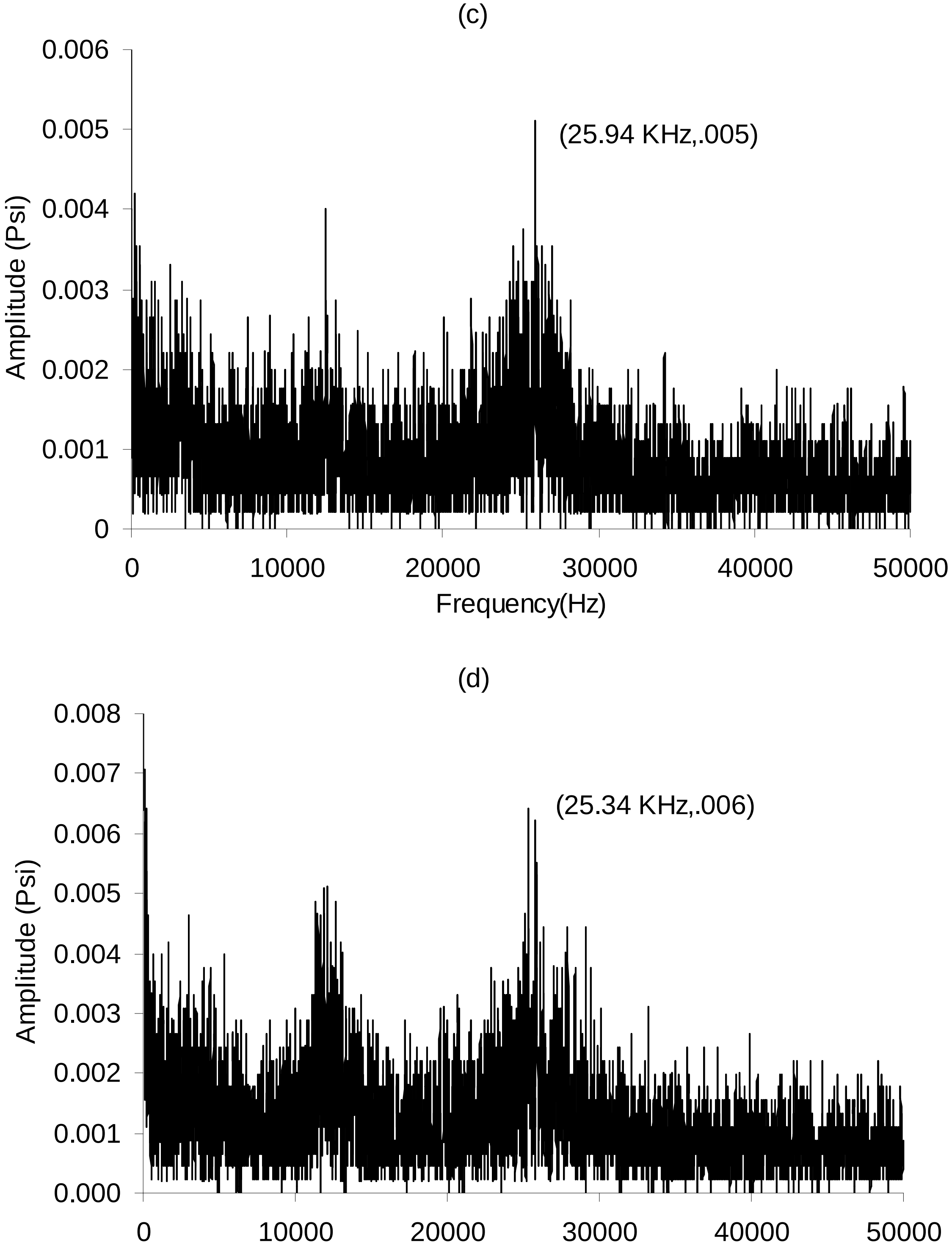

Figure 51(ii). L3D1 cavity at upstream stagnation pressures of (c) 55 psi, (d) 75 psi

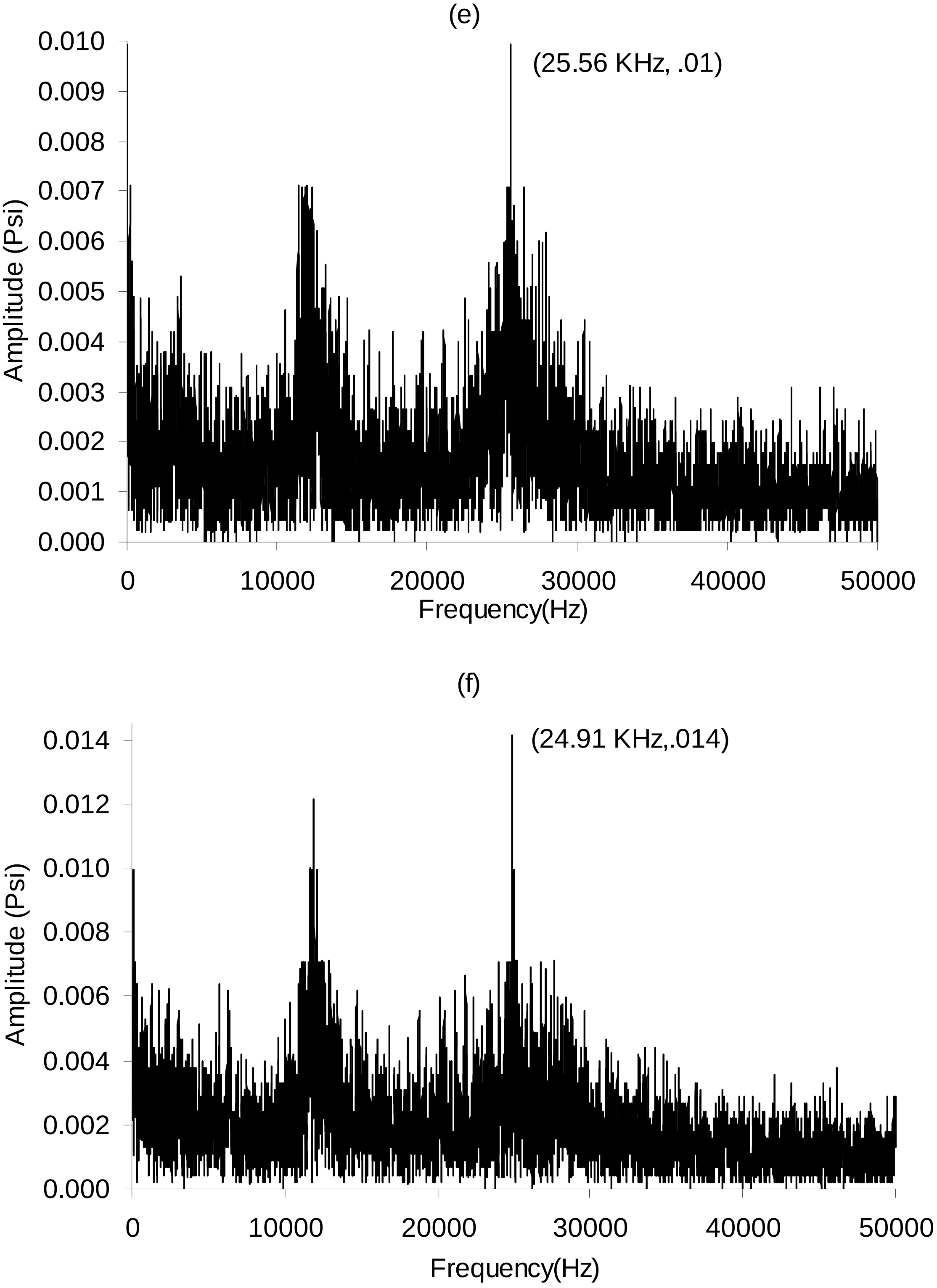

Figure 51(iii). L3D1 cavity at upstream stagnation pressures of (c) 95 psi, (d) 120 psi

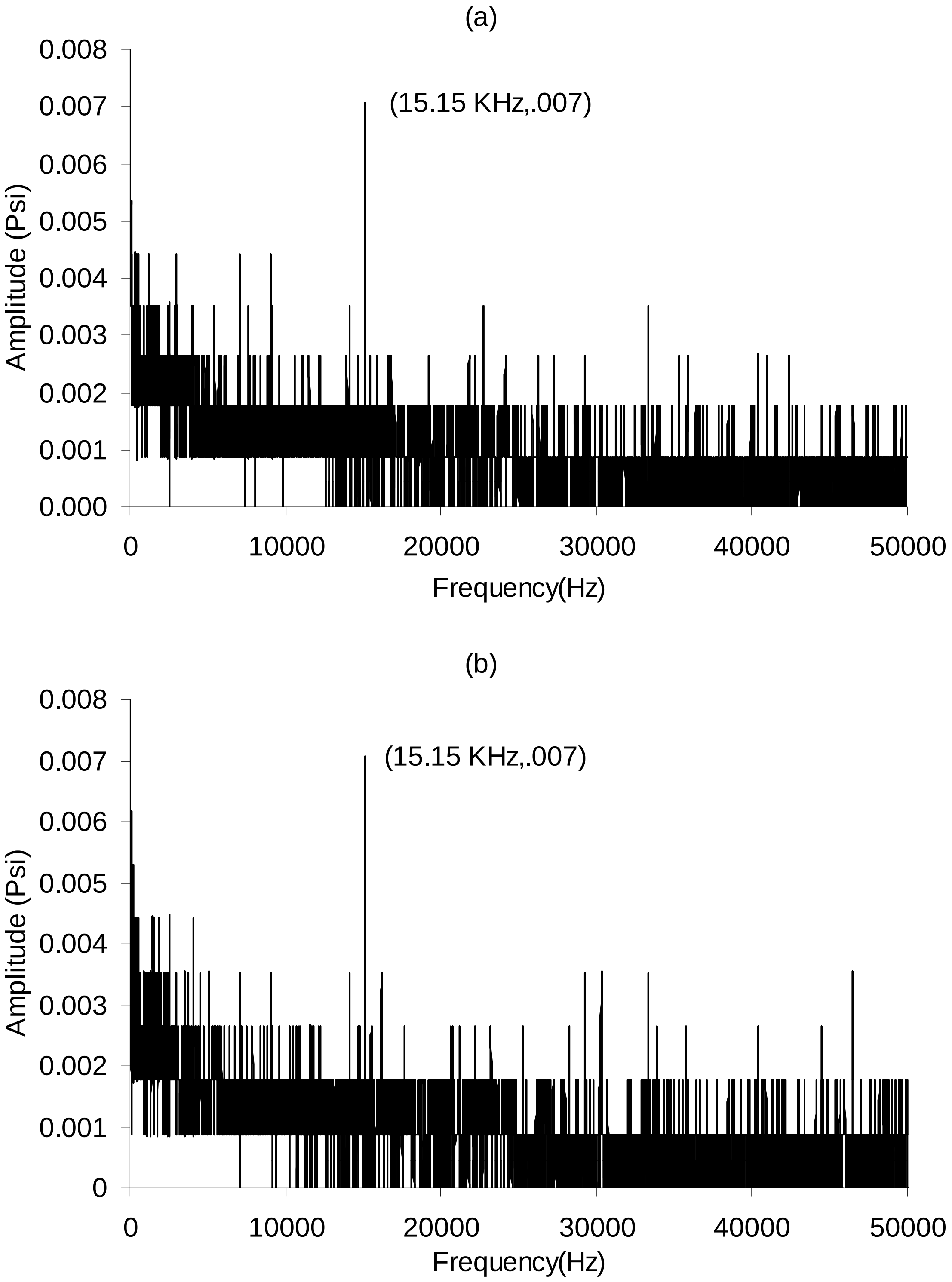

Figure 52(i). L4D1 cavity at upstream stagnation pressures of (a) 30 psi, (b) 35 psi.

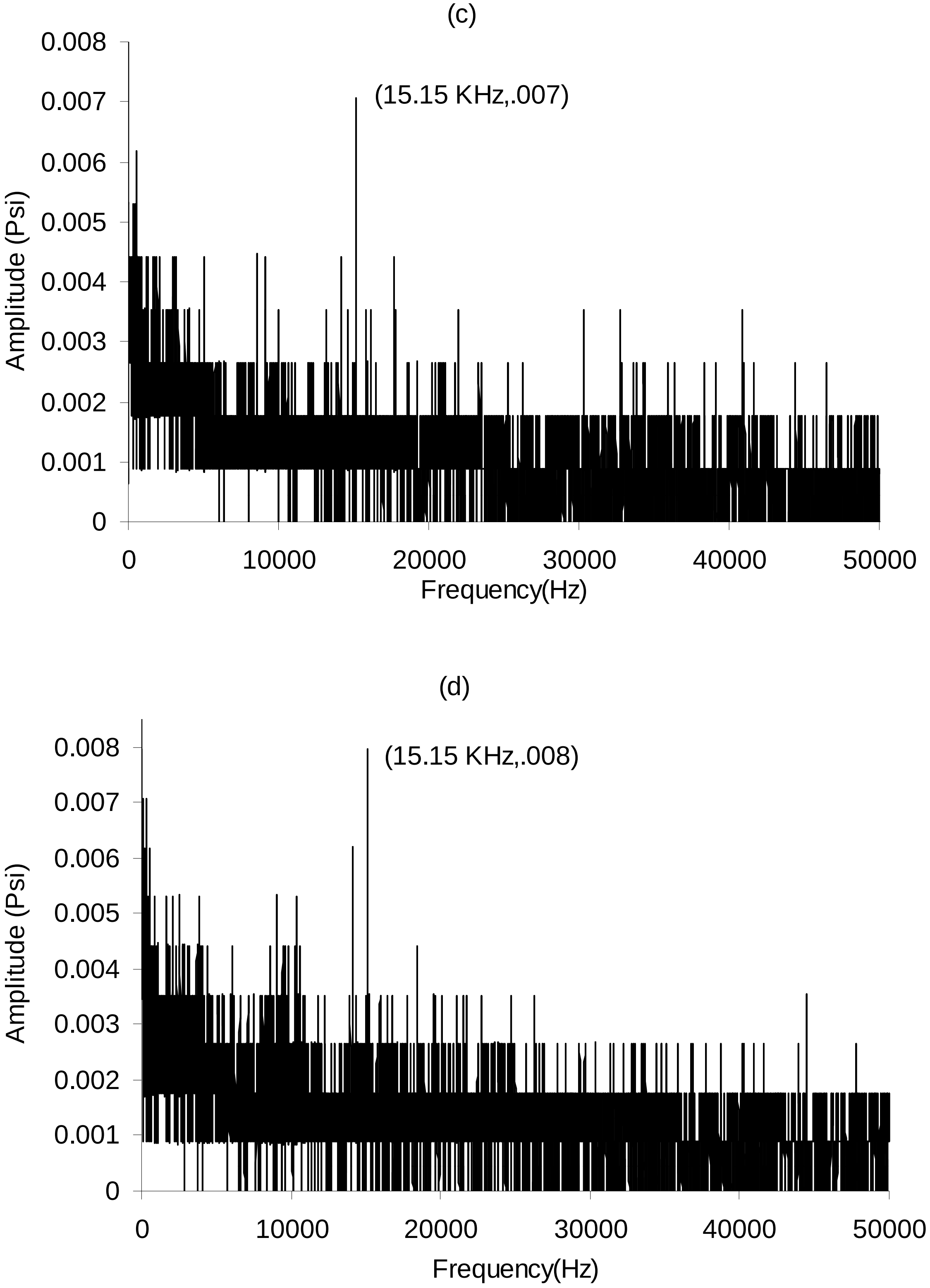

Figure 48(ii). L4D1 cavity at upstream stagnation pressures of (c) 55 psi, (d) 75 psi.

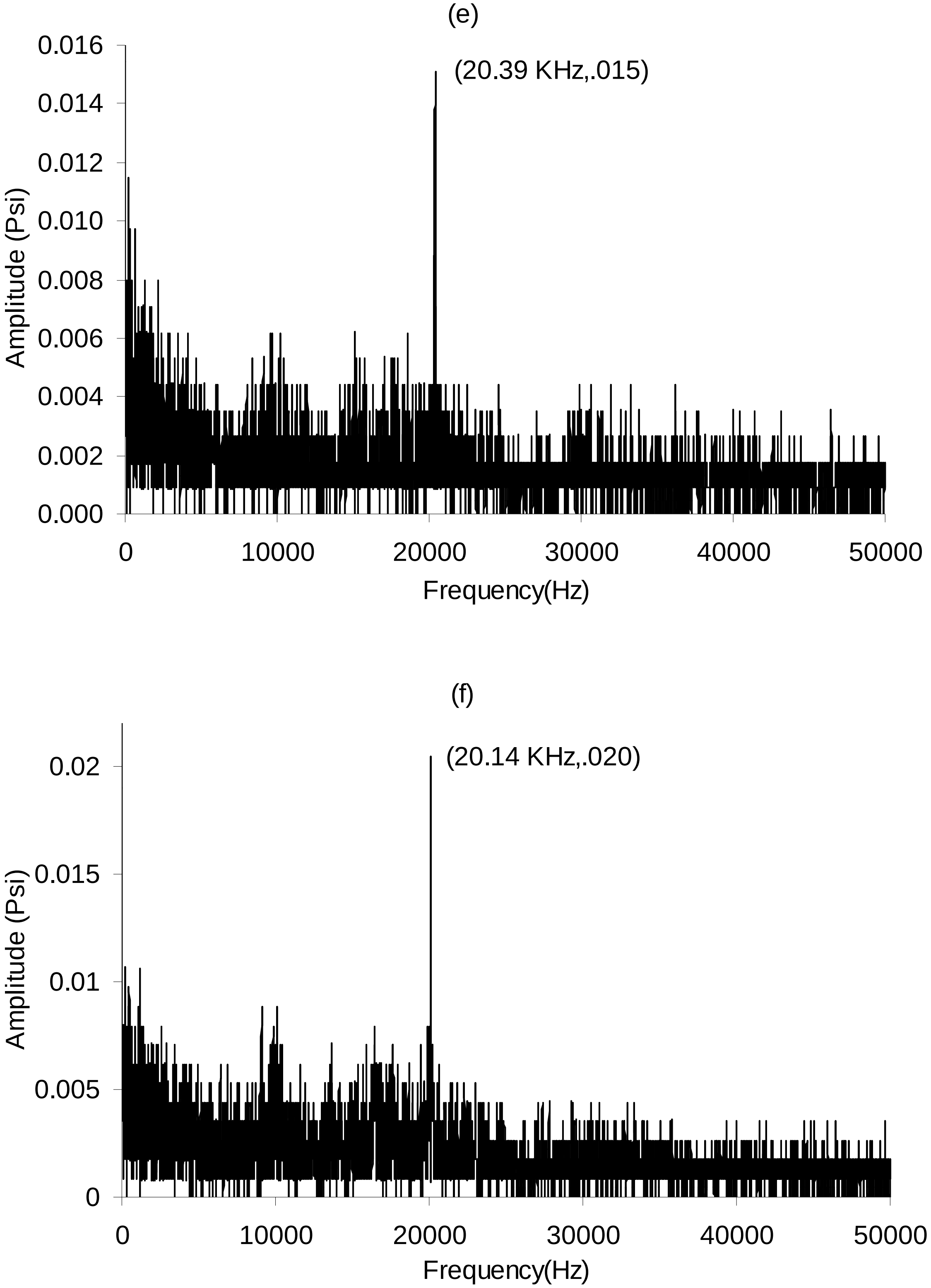

Figure 51(iii). L4D1 cavity at upstream stagnation pressures of (e) 95 psi, (f) 120 psi.

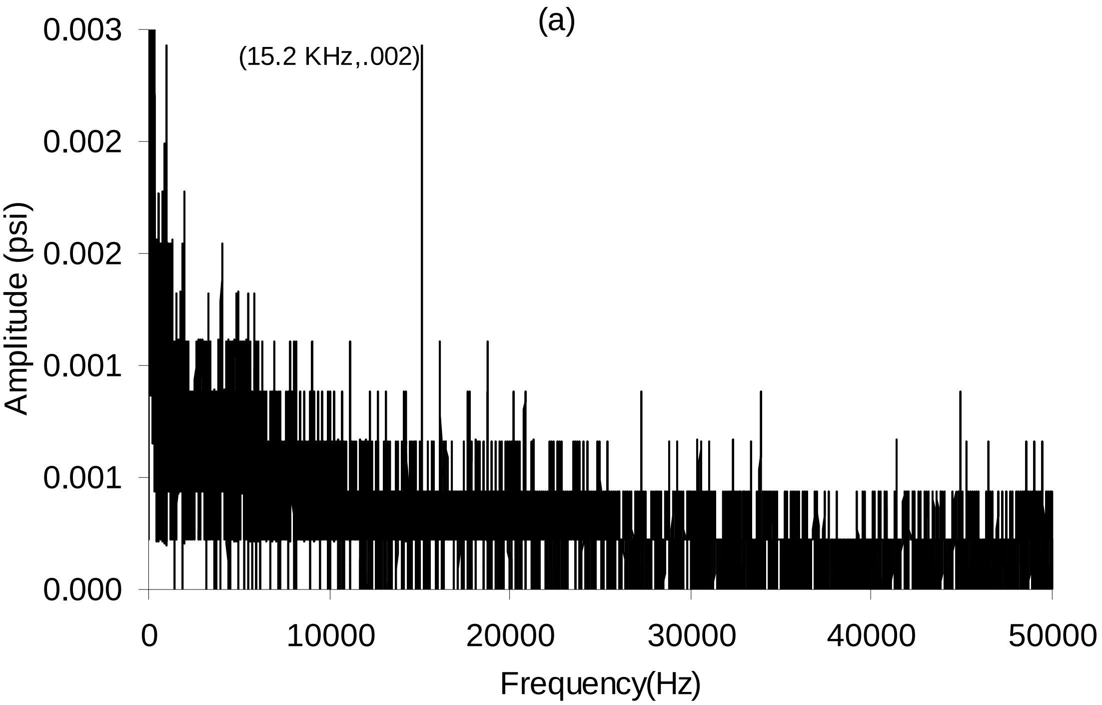

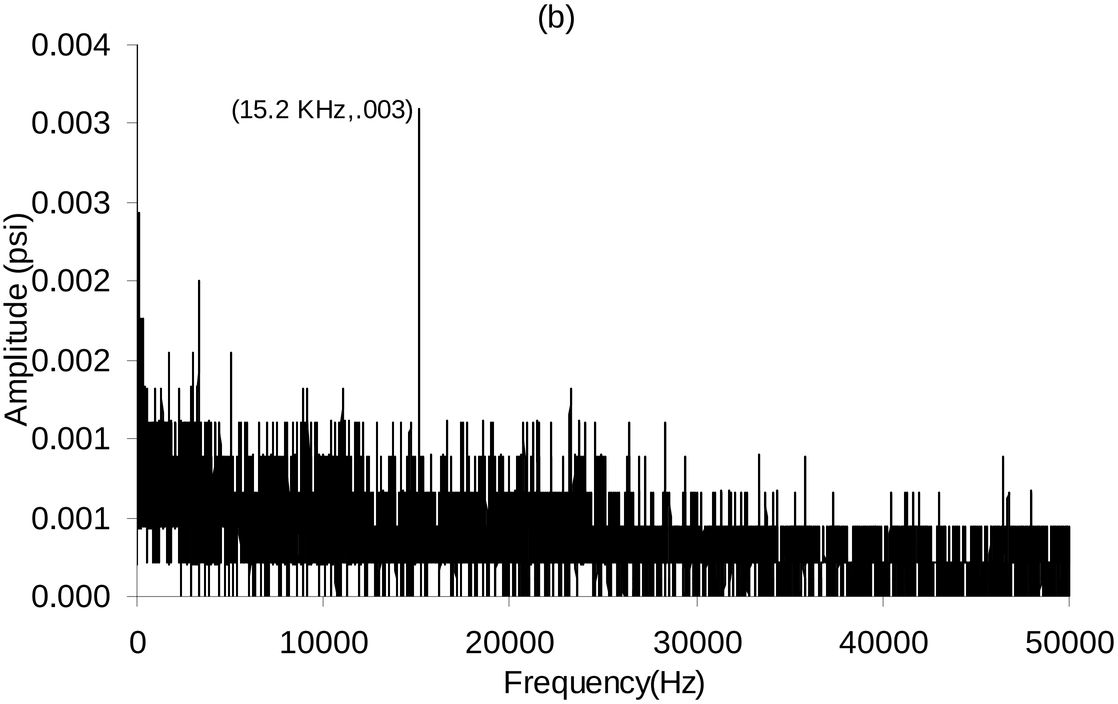

Figure 53(i). L5D1 cavity at upstream stagnation pressures of (a) 30 psi, (b) 35 psi.

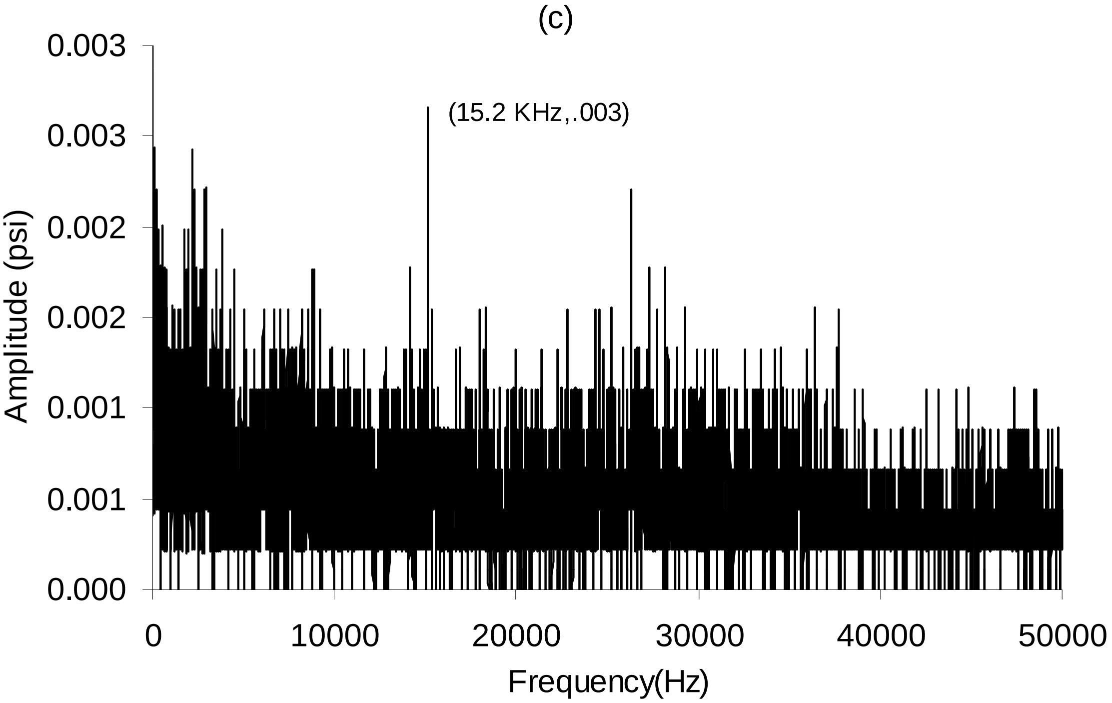

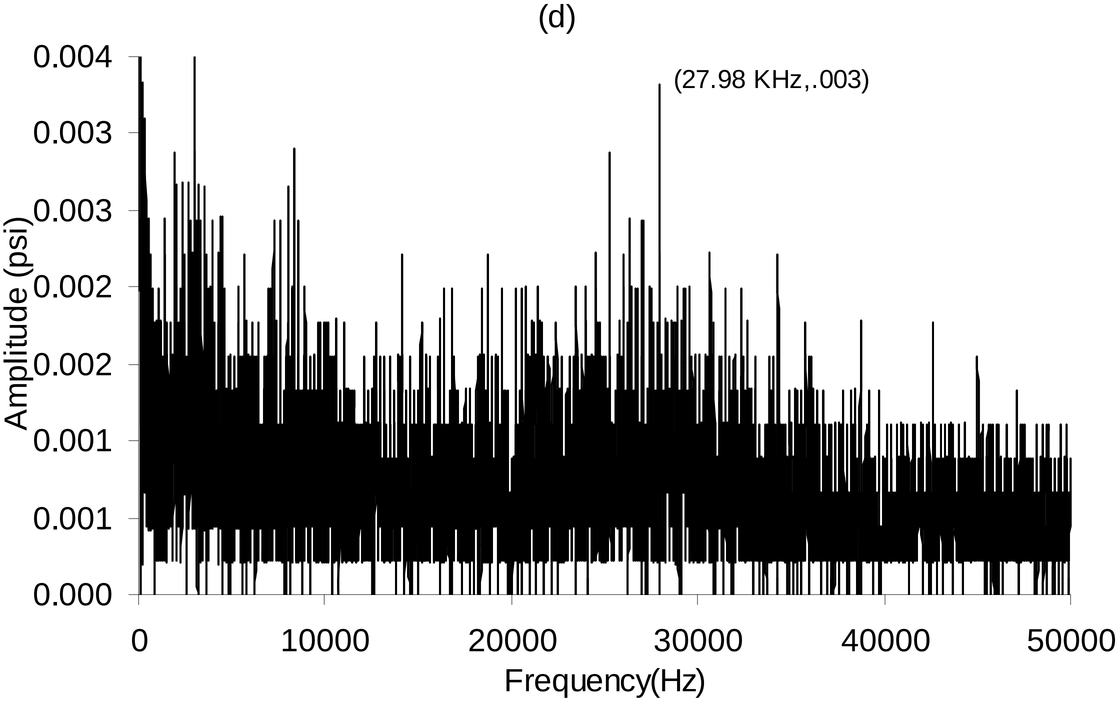

Figure 53(ii). L5D1 cavity at upstream stagnation pressures of (c) 55 psi, (d) 75 psi.

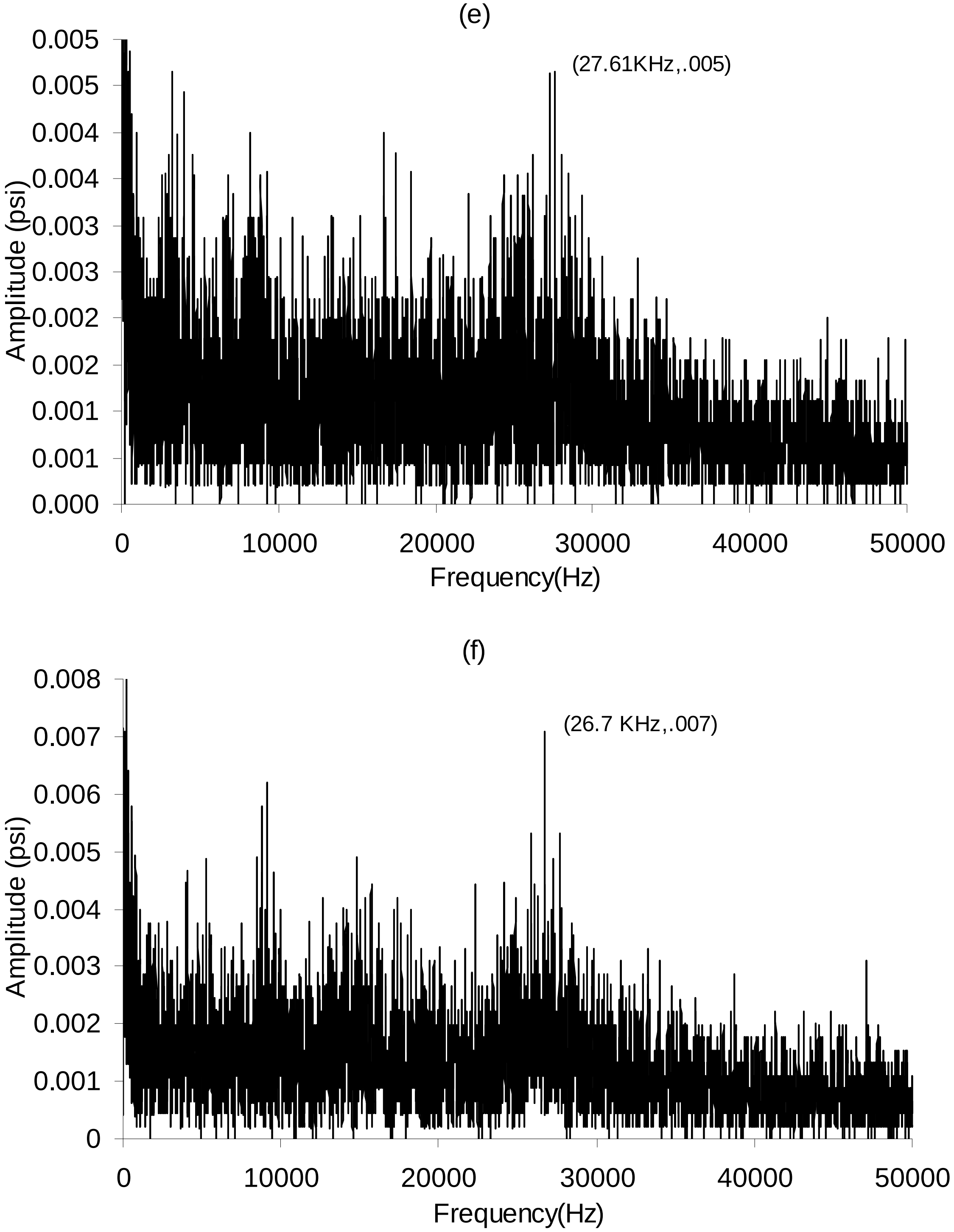

Figure 53(iii). L5D1 cavity at upstream stagnation pressures of (e) 95 psi, (f) 120 psi.

II. Deep cavities.

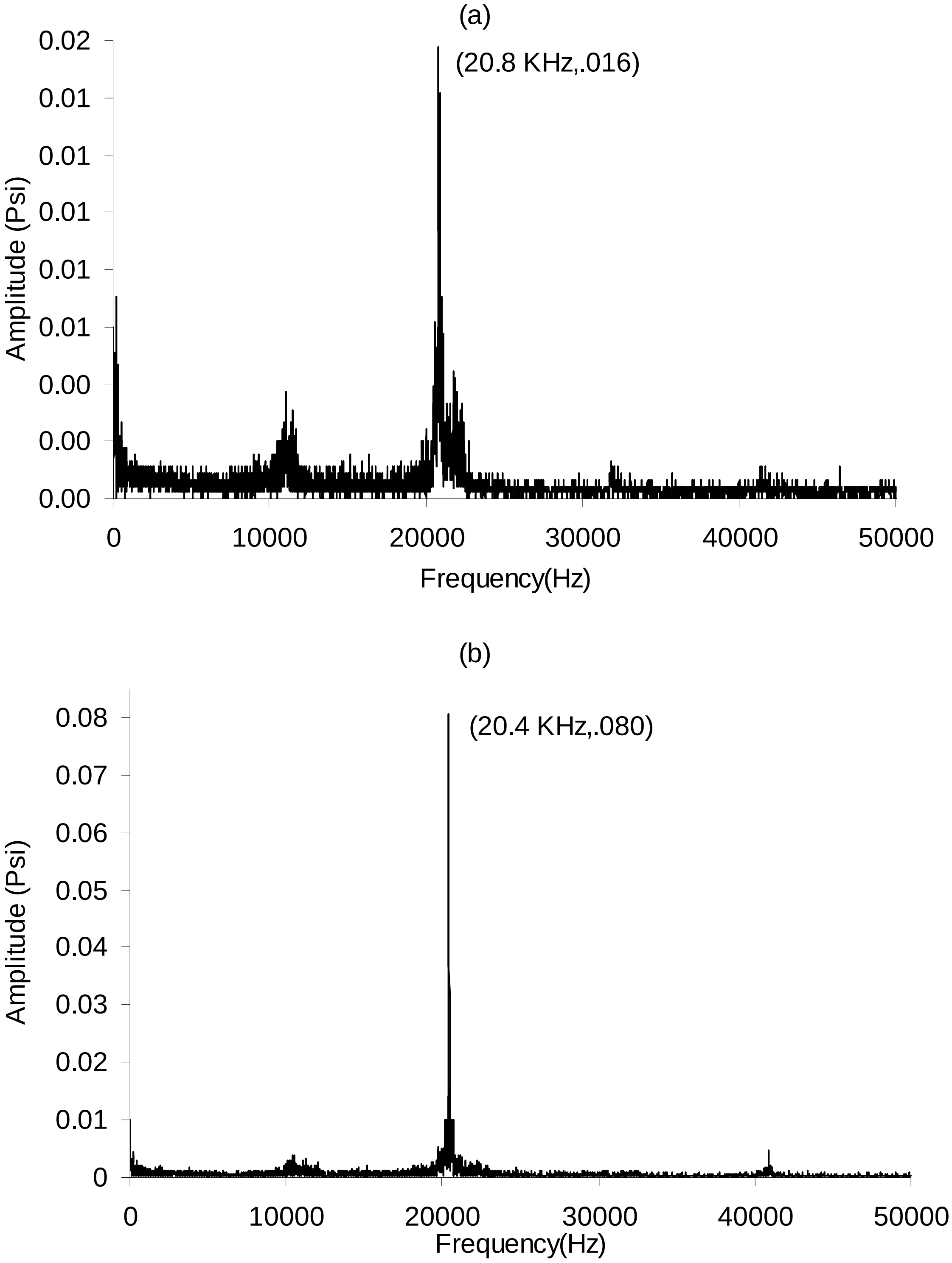

Figure 54(i). L4D2 cavity at upstream stagnation pressures of (a) 30 psi, (b) 35 psi.

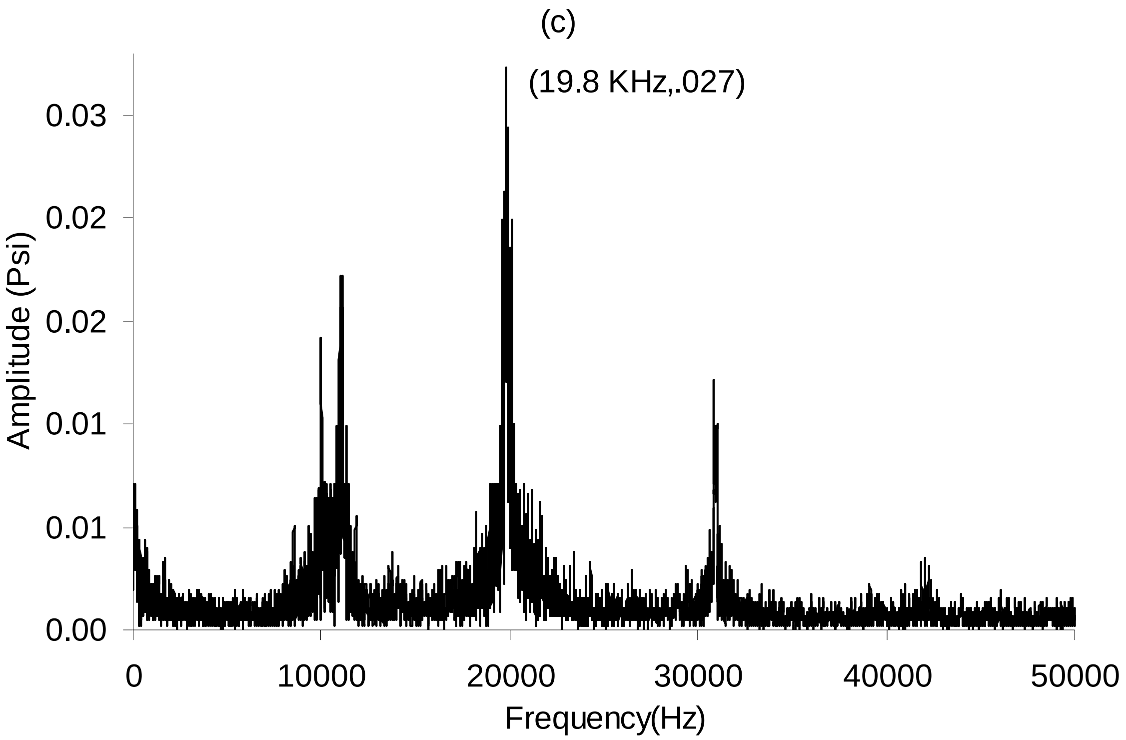

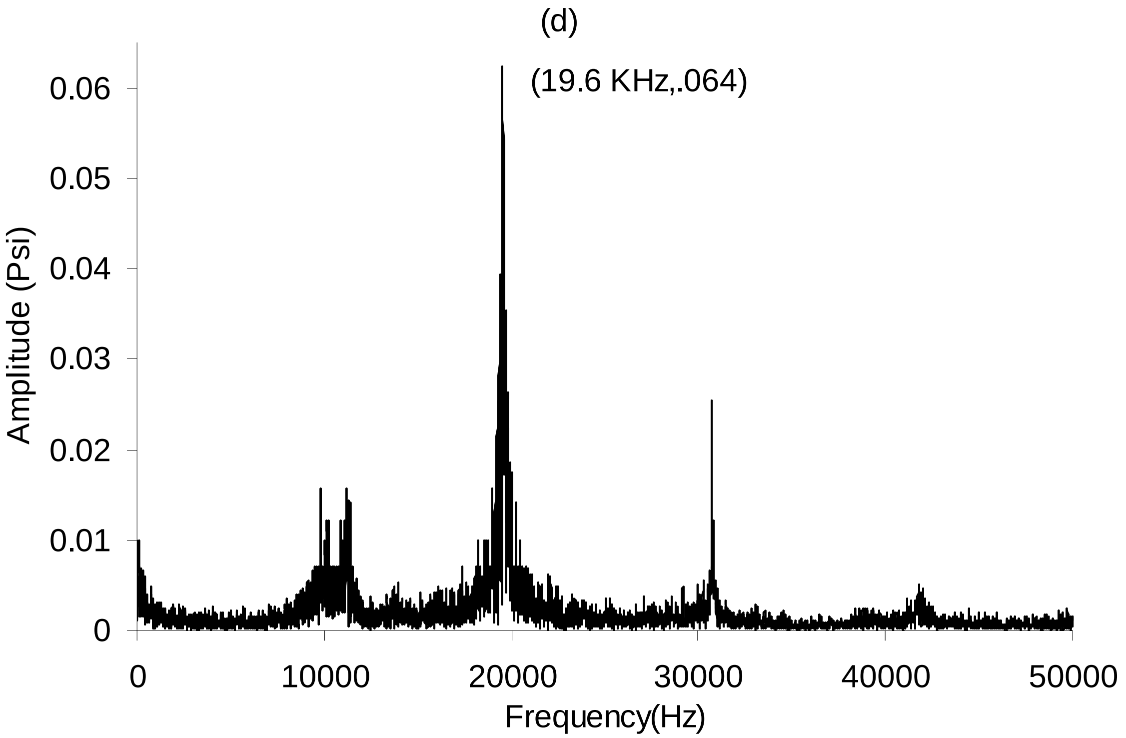

Figure 54(ii). L4D2 cavity at upstream stagnation pressures of (c) 55 psi, (d) 75 psi.

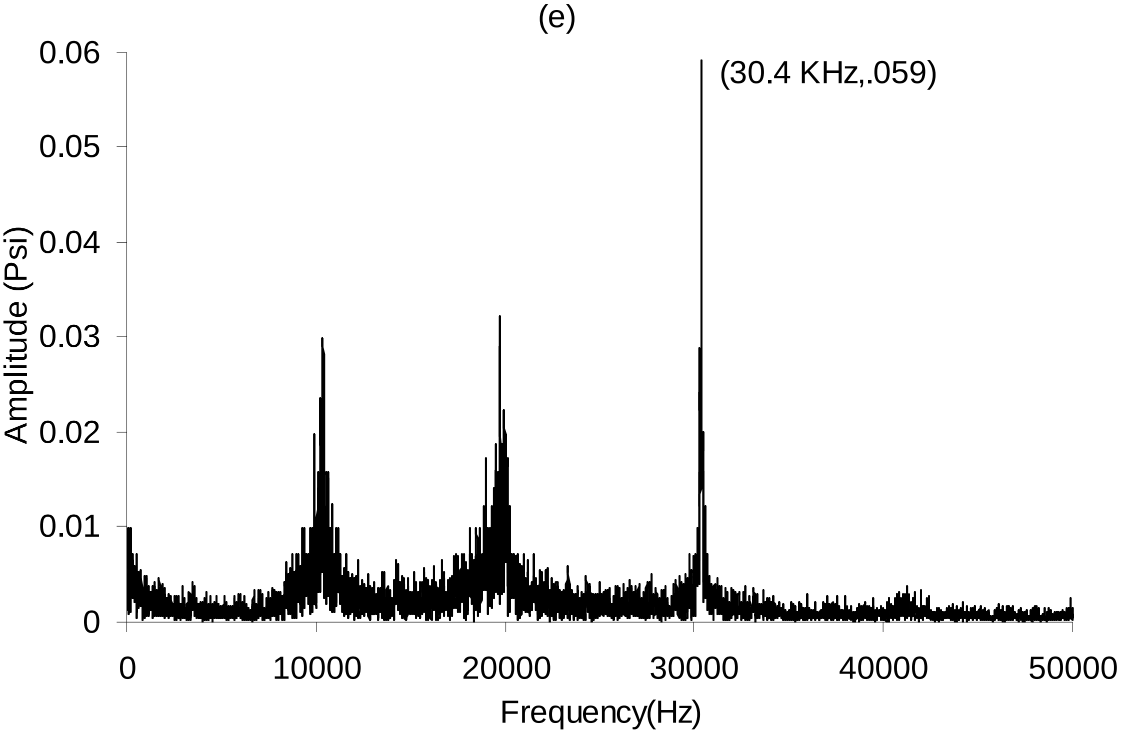

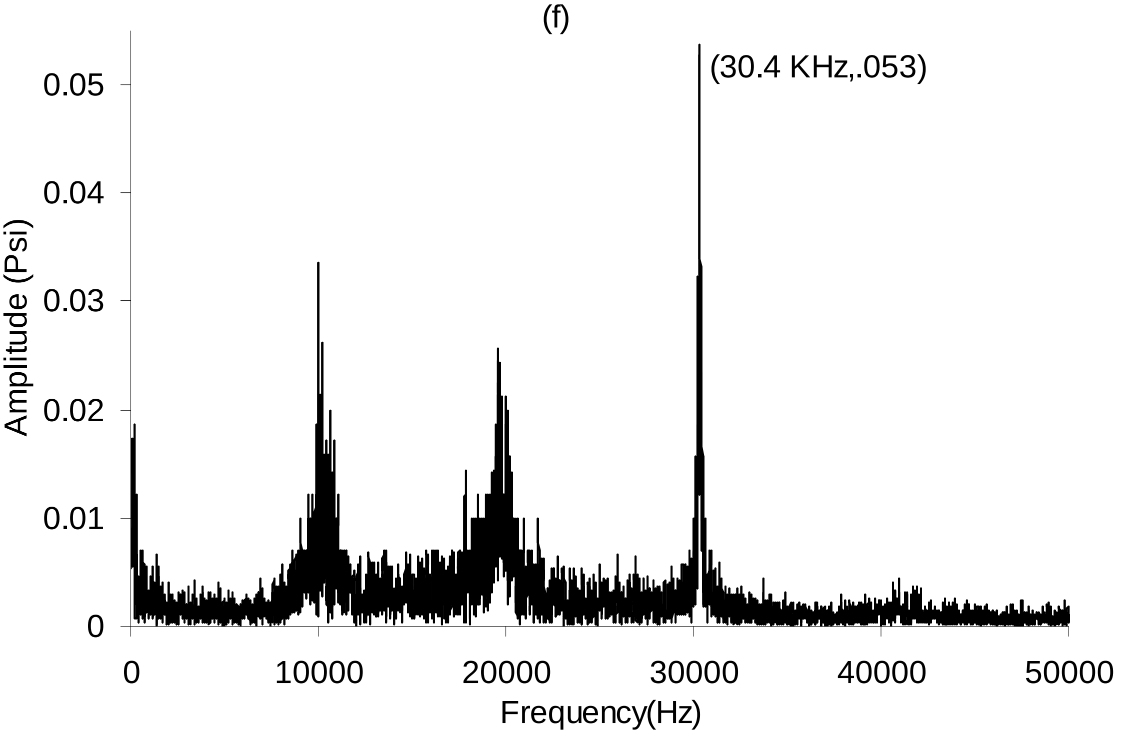

Figure 54(iii). L4D2 cavity at upstream stagnation pressures of (e) 95 psi, (f) 120 psi

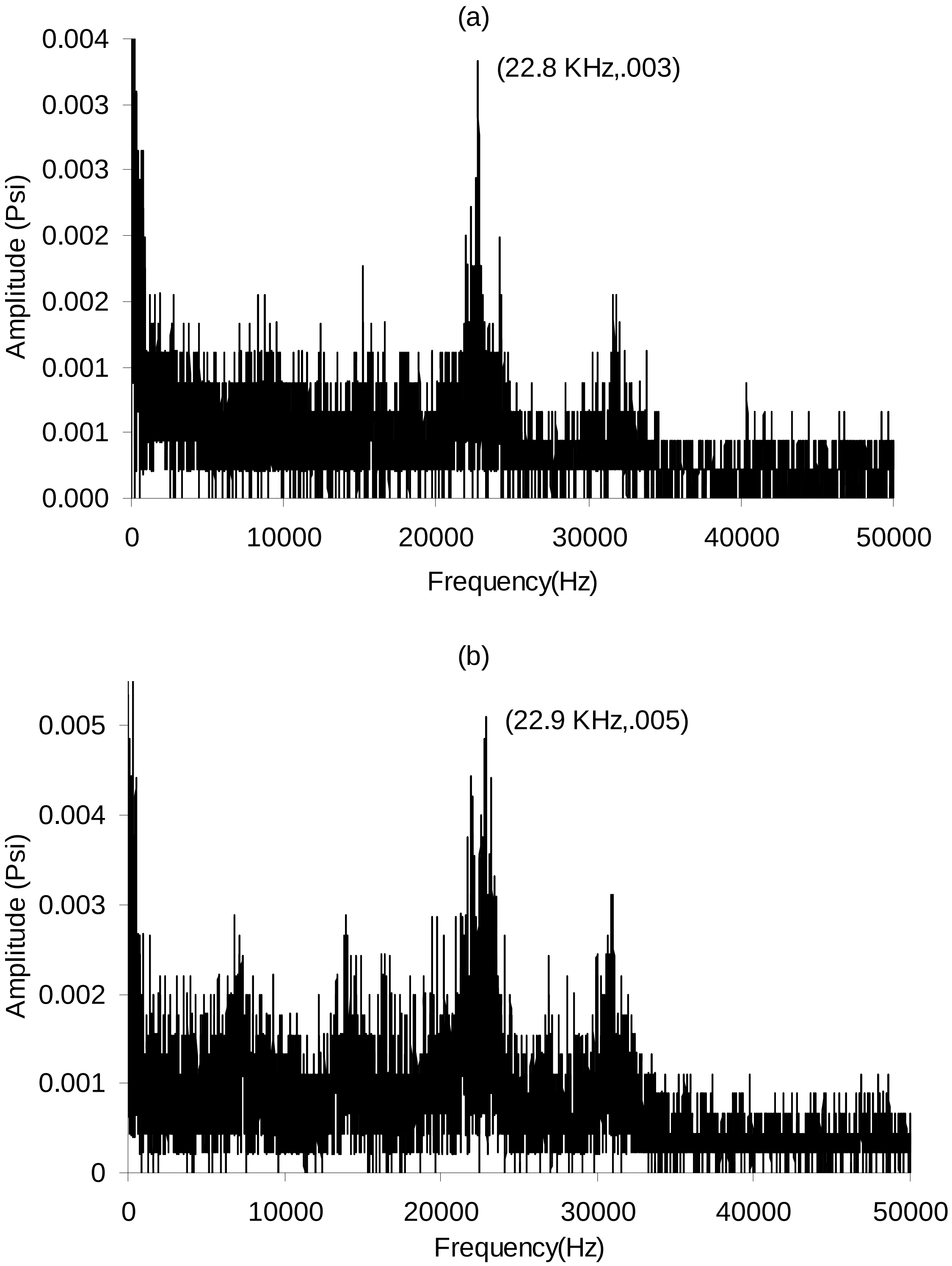

Figure 55(i). L6D2 cavity at upstream stagnation pressures of (a) 30 psi, (b) 35 psi.

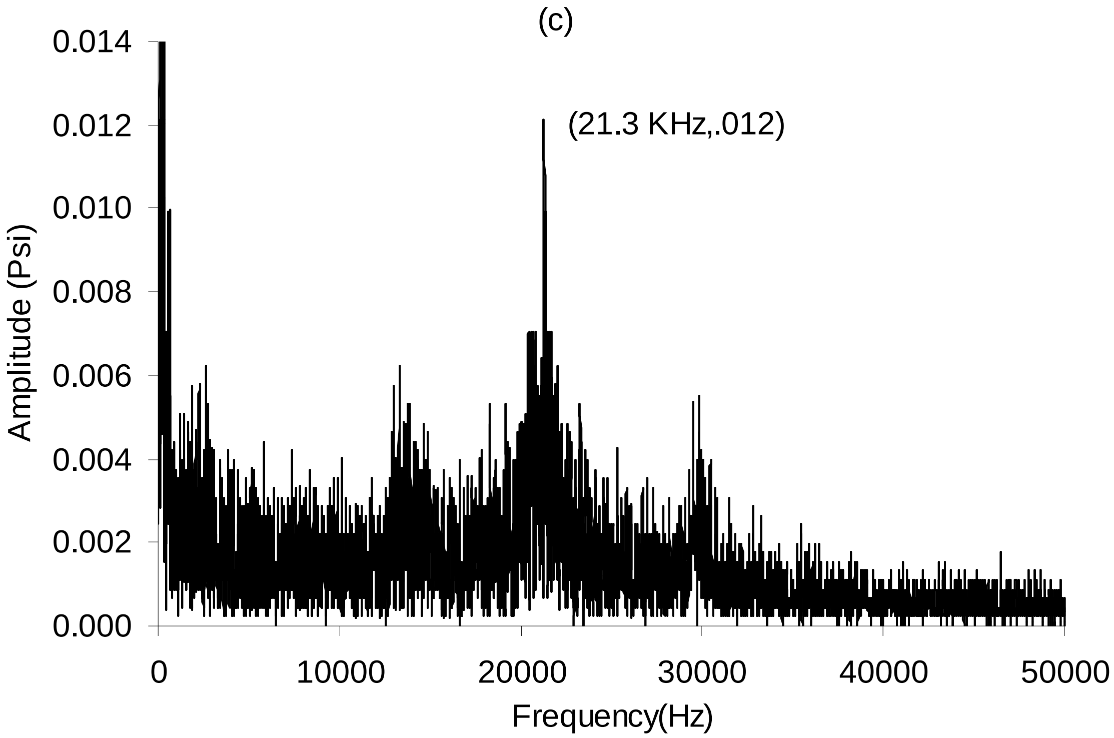

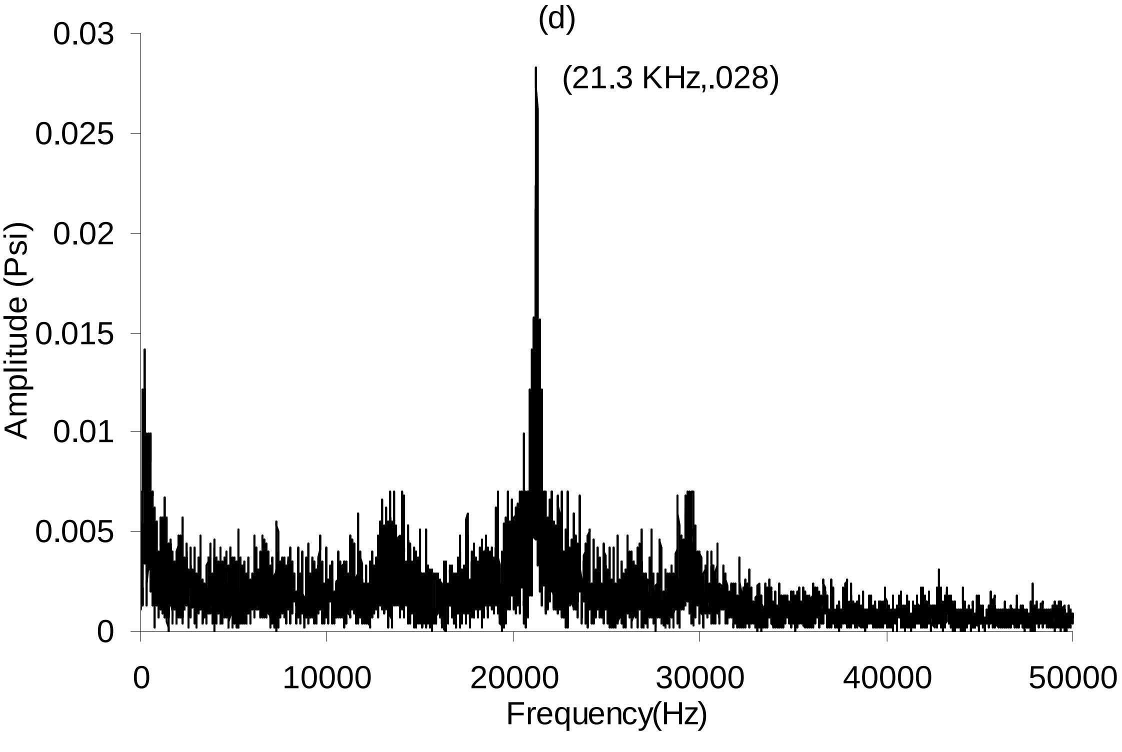

Figure 55(ii). L6D2 cavity at upstream stagnation pressures of (c) 55 psi, (d) 75 psi

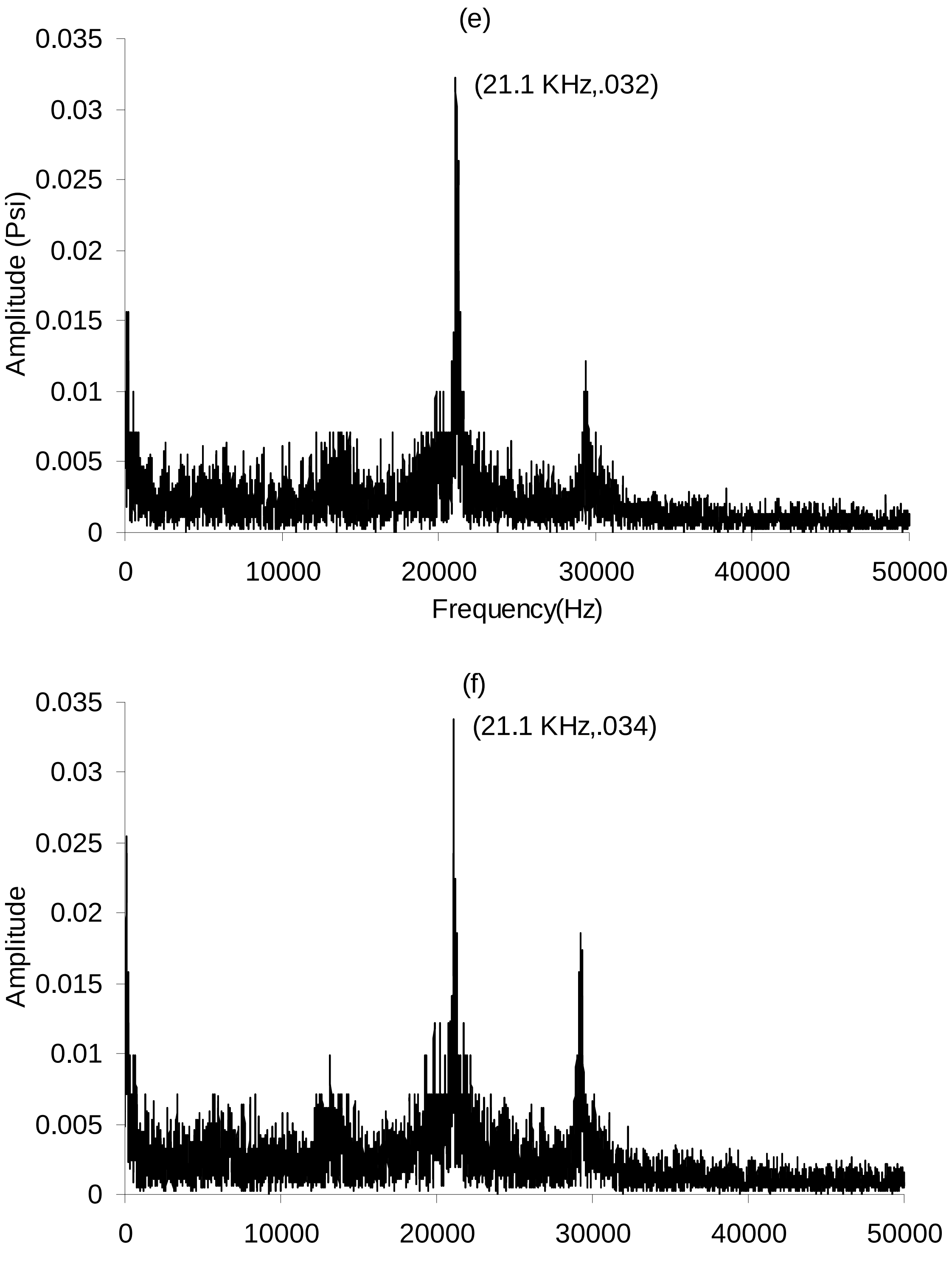

Figure 55(iii). L6D2 cavity at upstream stagnation pressures of (e) 95 psi, (f) 120 psi.

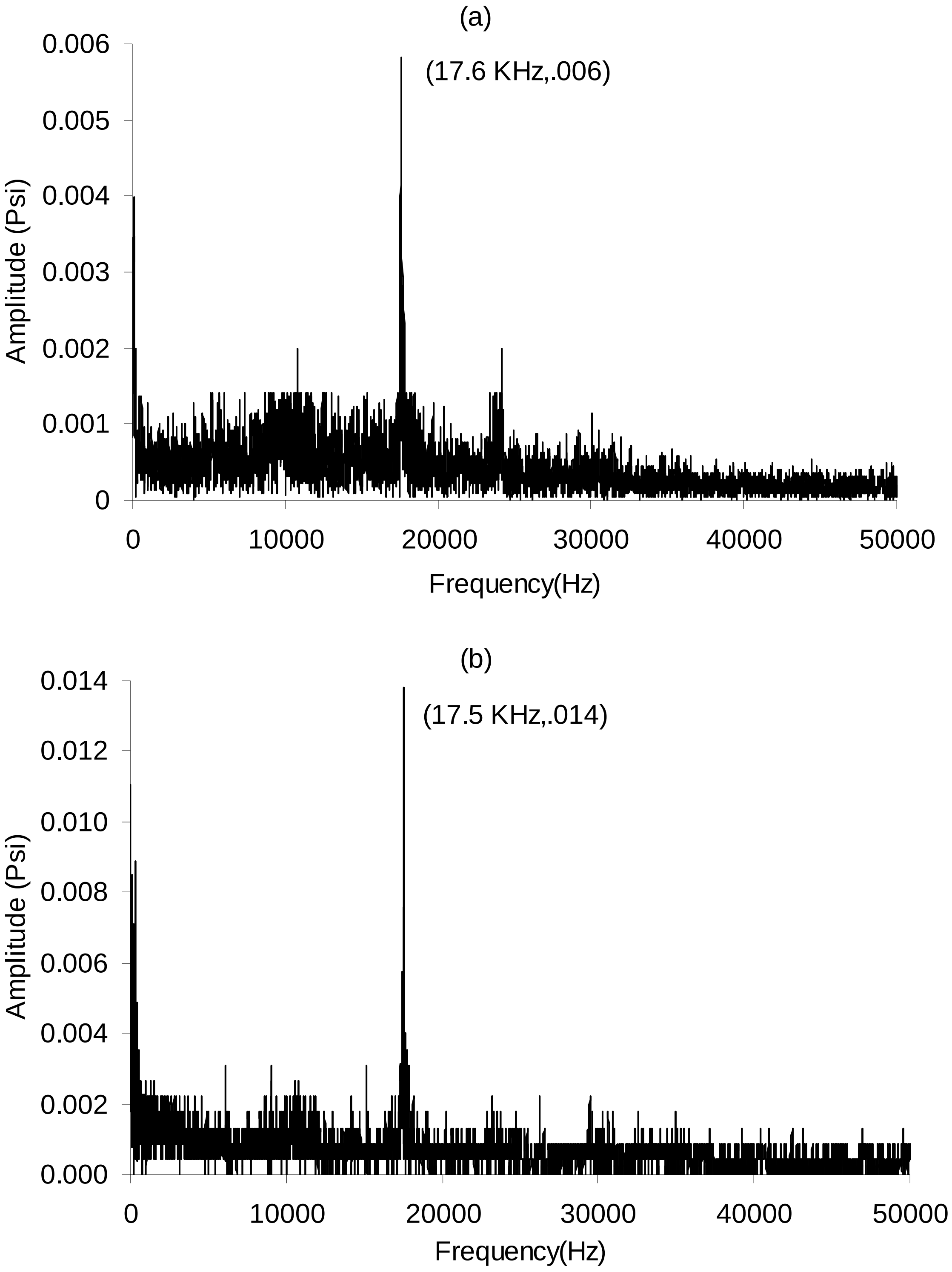

Figure 56(i). L8D2 cavity at upstream stagnation pressures of (a) 30 psi, (f) 35 psi.

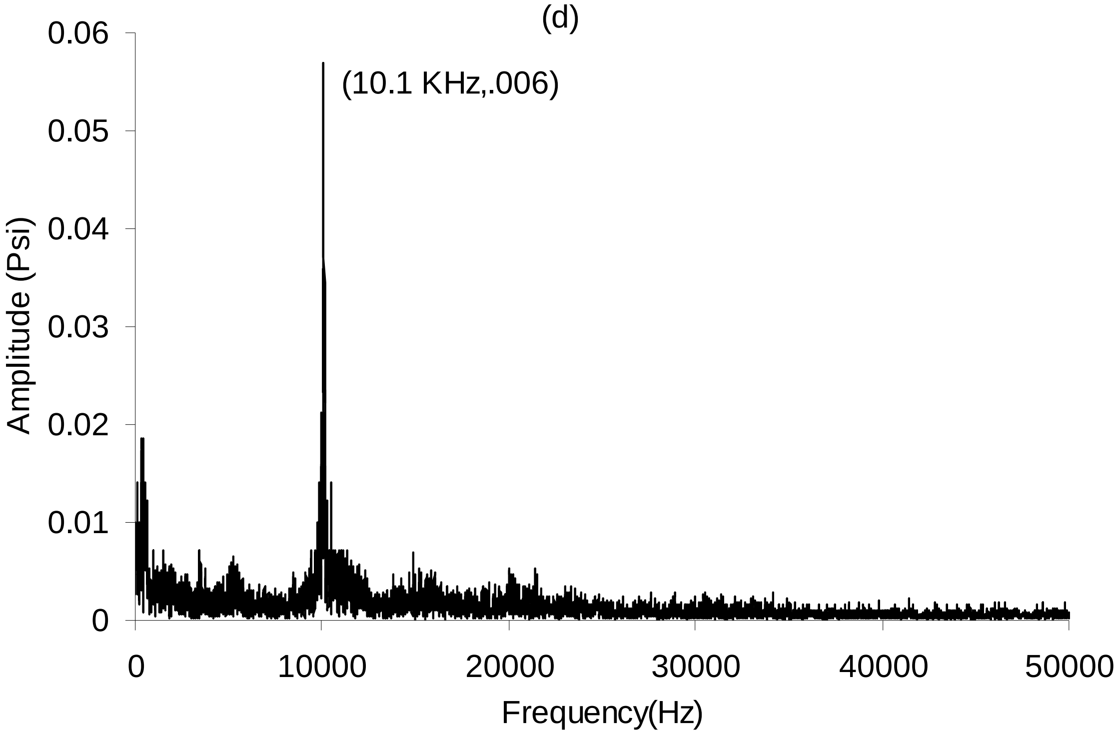

Figure 56(ii). L8D2 cavity at upstream stagnation pressures of (c) 55 psi, (d) 75 psi.

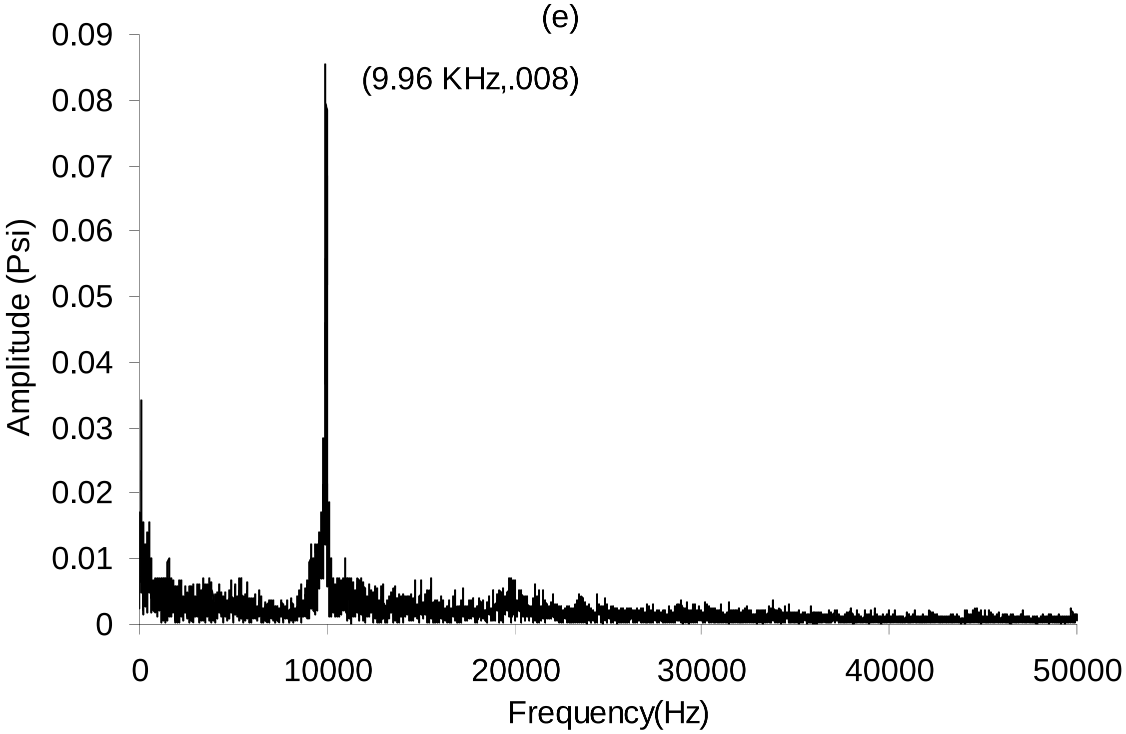

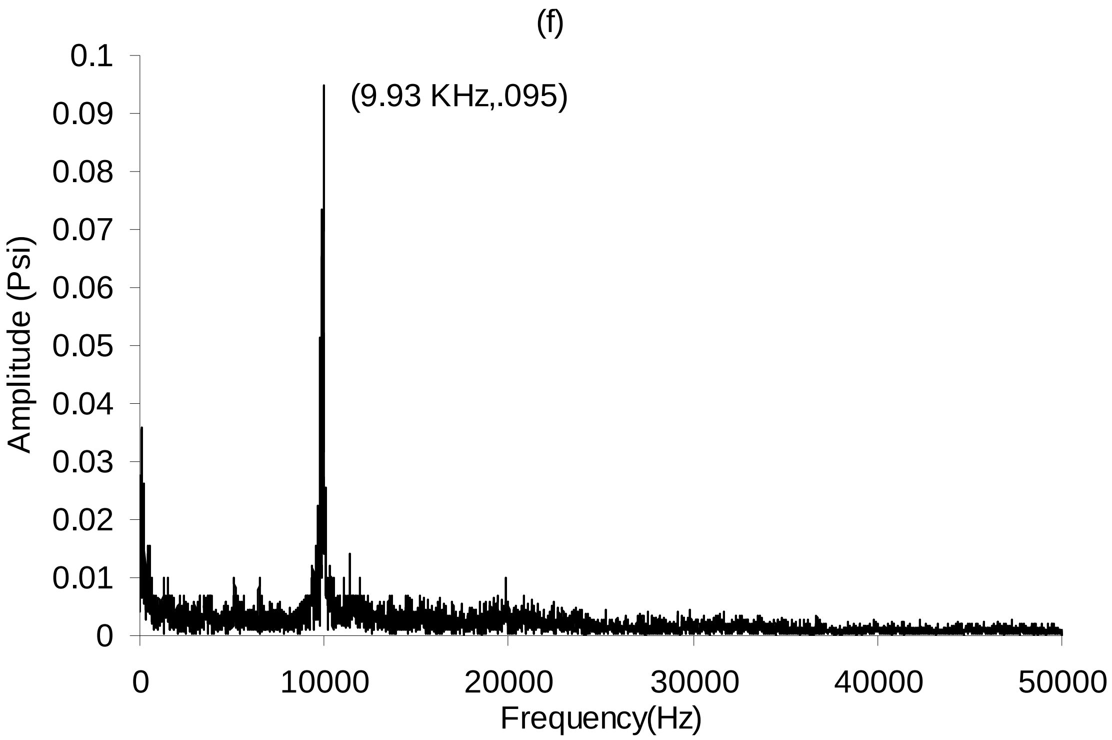

Figure 56(iii). L8D2 cavity at upstream stagnation pressures of (e) 95 psi, (f) 120 psi.

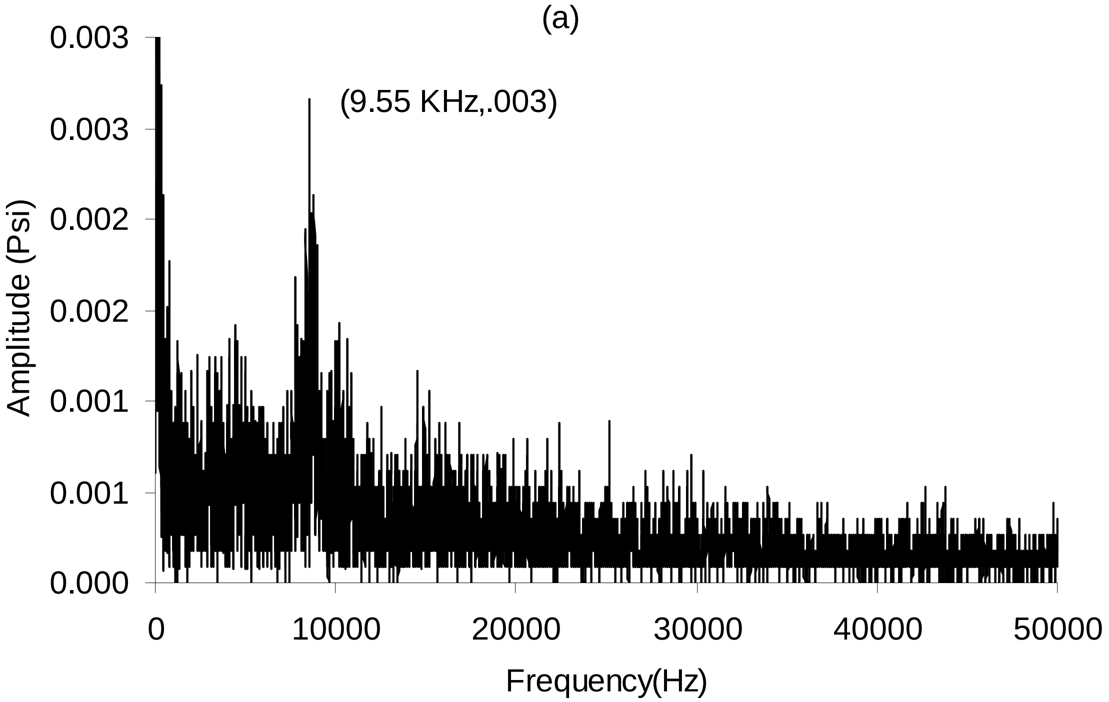

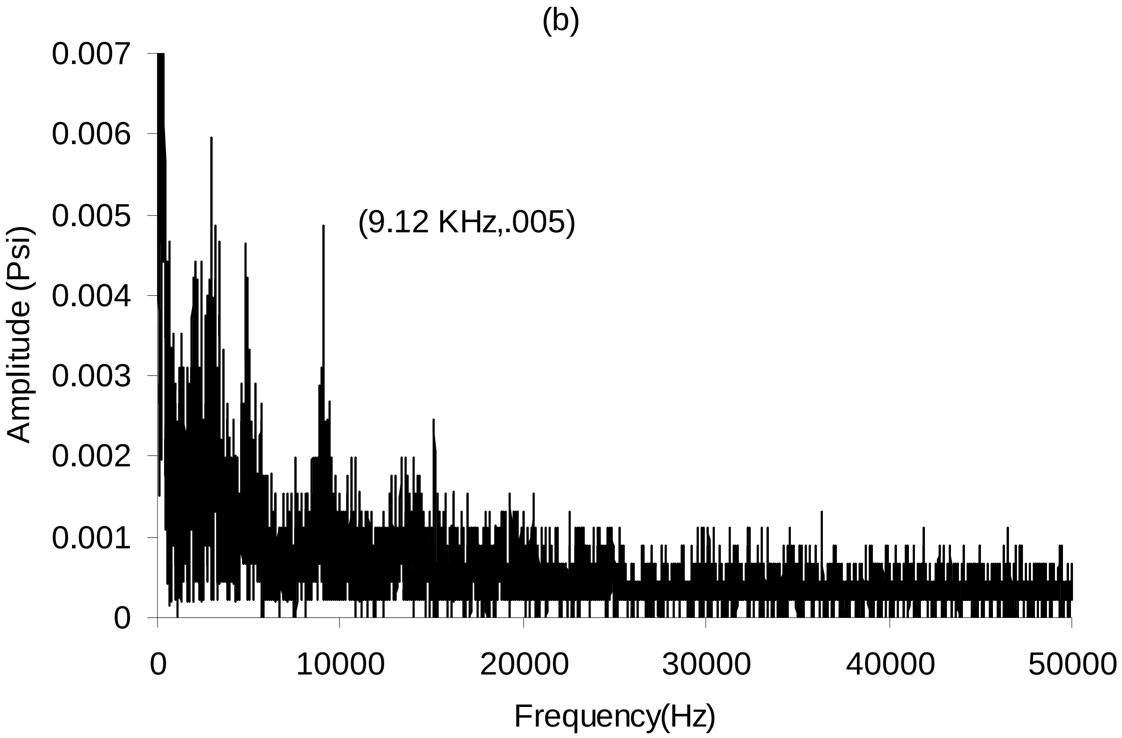

Figure 57(i). L10D2 cavity at upstream stagnation pressures of (a) 30 psi, (b) 35 psi

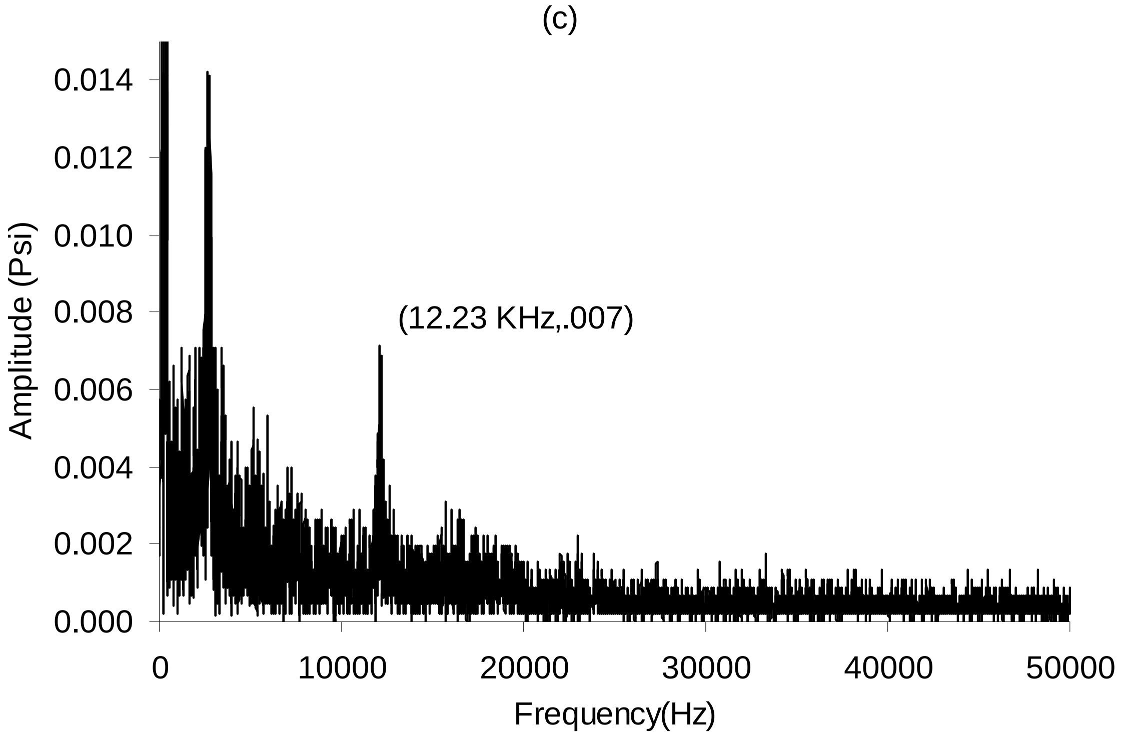

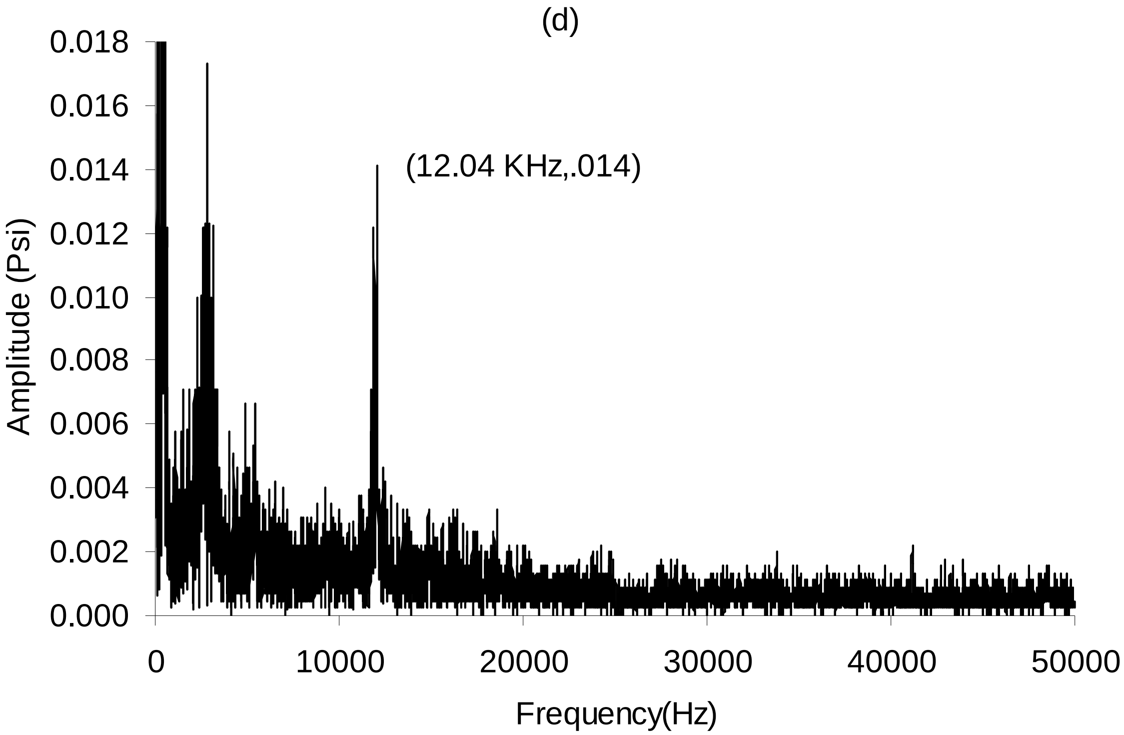

Figure 57(ii). L10D2 cavity at upstream stagnation pressures of (c) 55 psi, (d) 75 psi

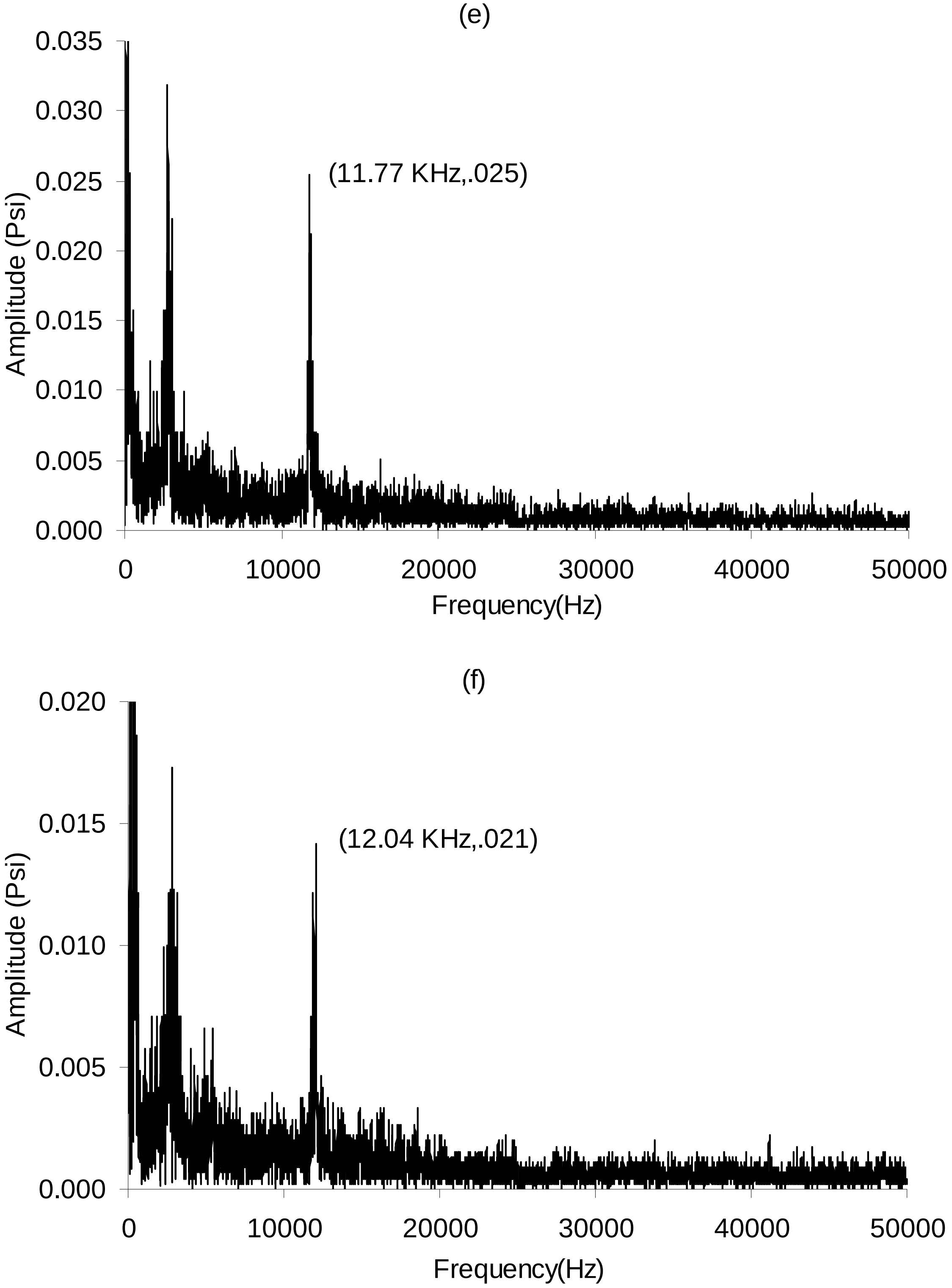

Figure 57(iii). L10D2 cavity at upstream stagnation pressures of (e)95 psi, (f)120 psi.

Appendix B – Comparison with Modified Rossiter results

I. Shallow cavities

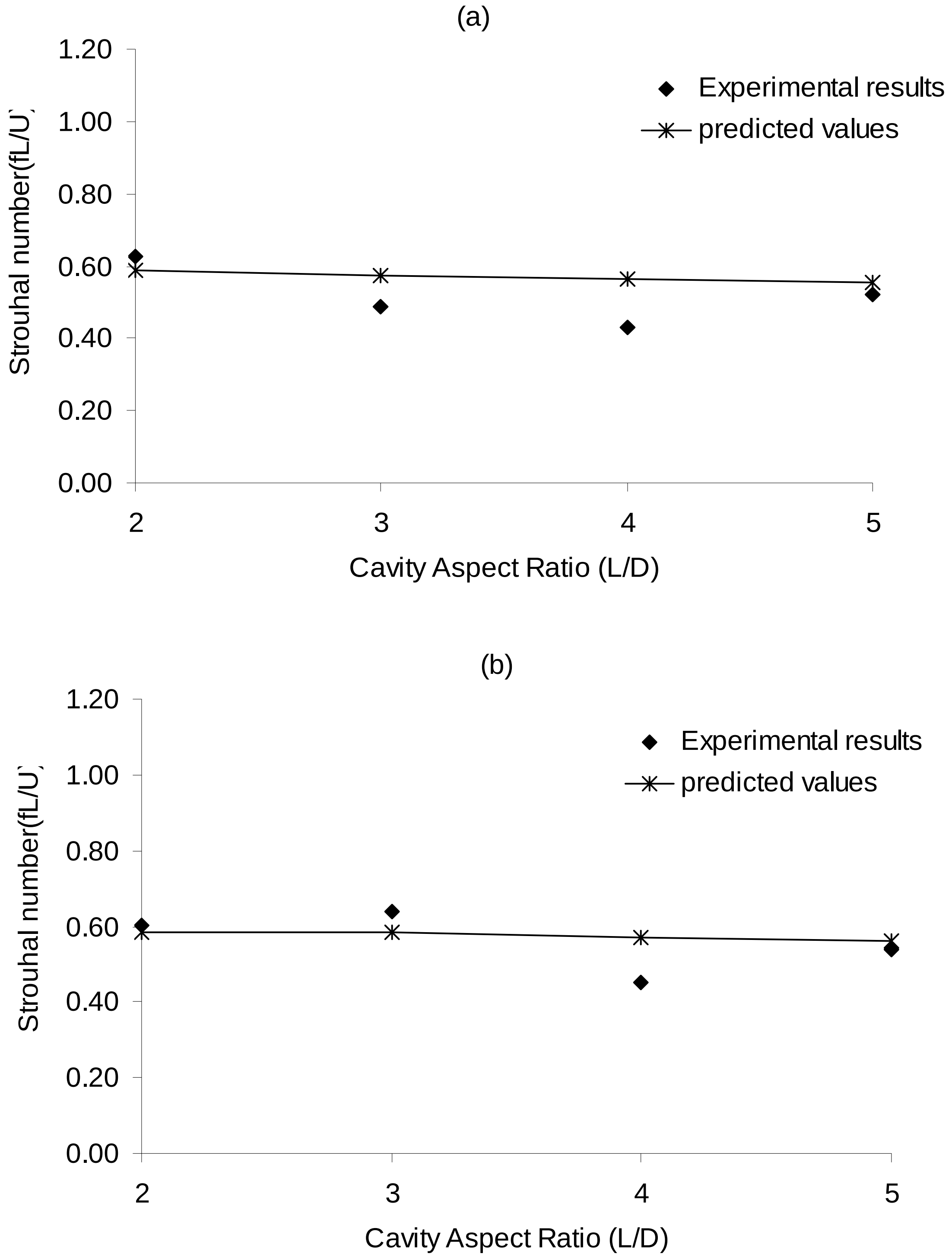

Figure 58(i). Comparison with modified Rossiter predicted values at (a)35 psi, (b)55 psi.

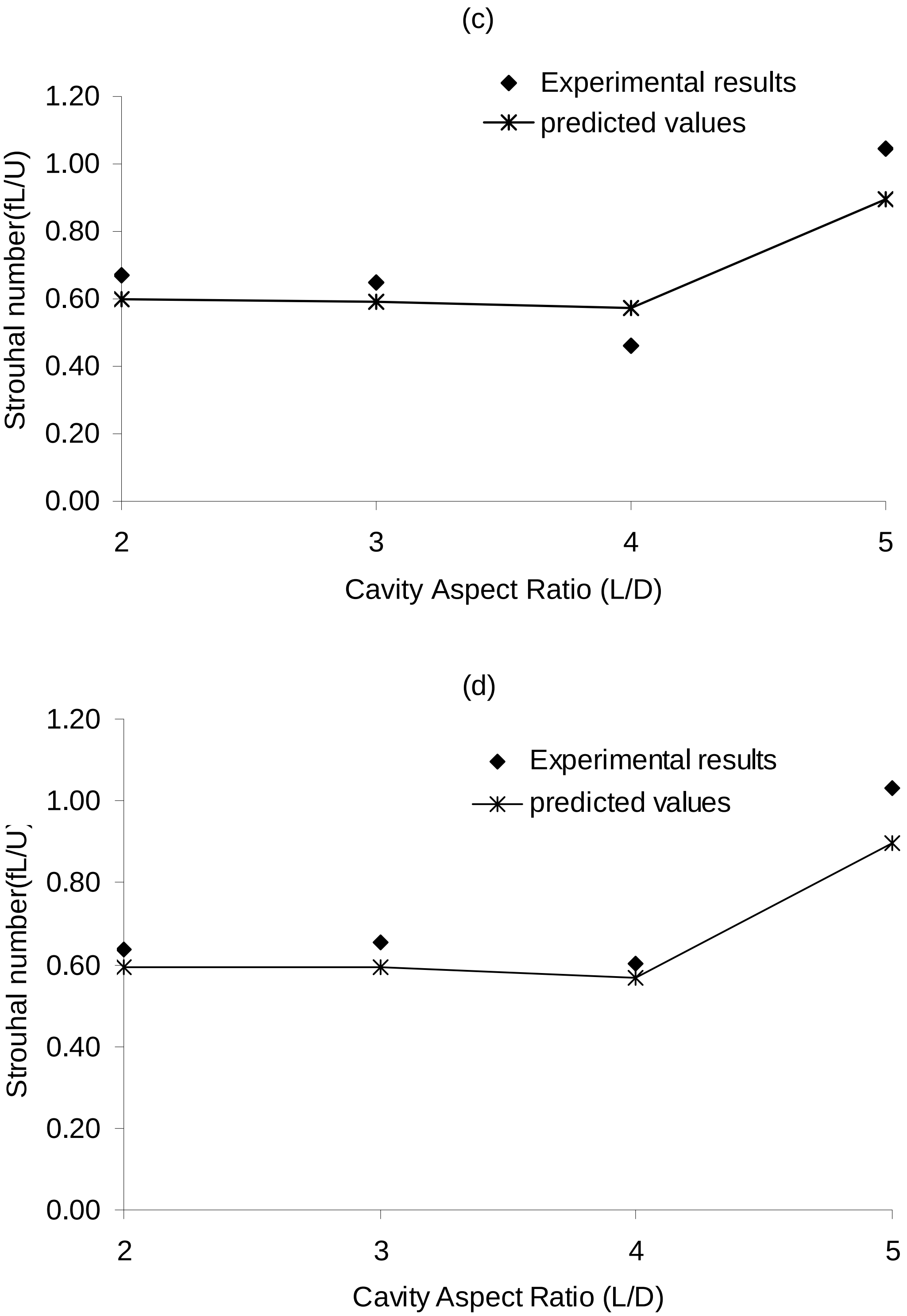

Figure 58(ii). Comparison with modified Rossiter predicted values at (c)75 psi, (d)95 psi.

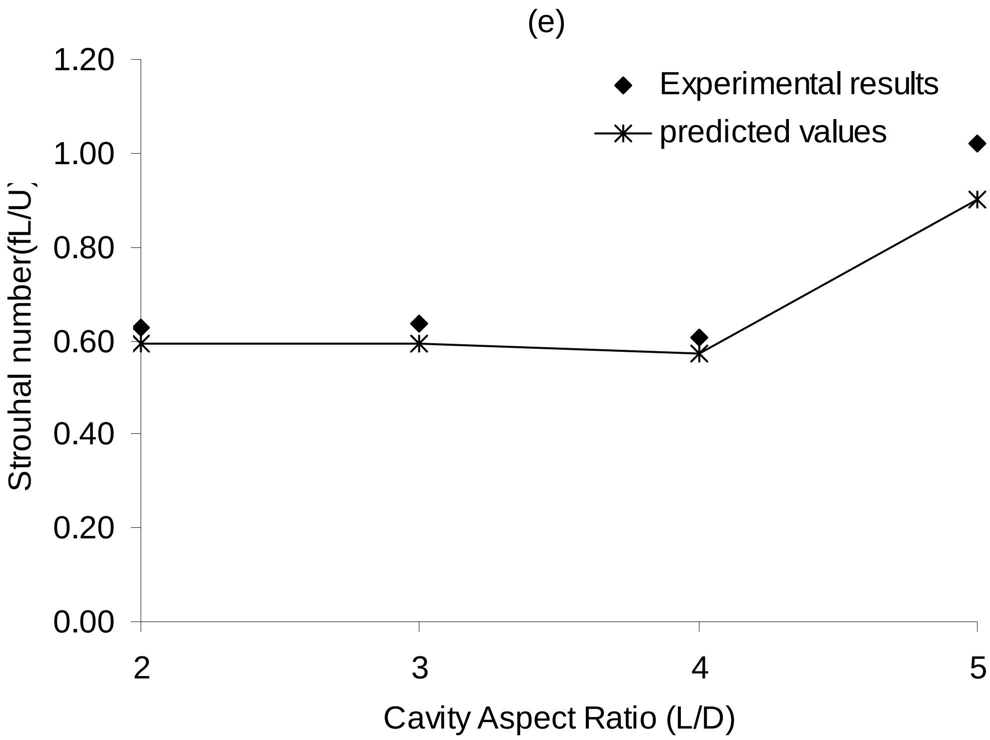

Figure 58(iii). Comparison with modified Rossiter predicted values at (e) 120 psi.

II. Deep cavities

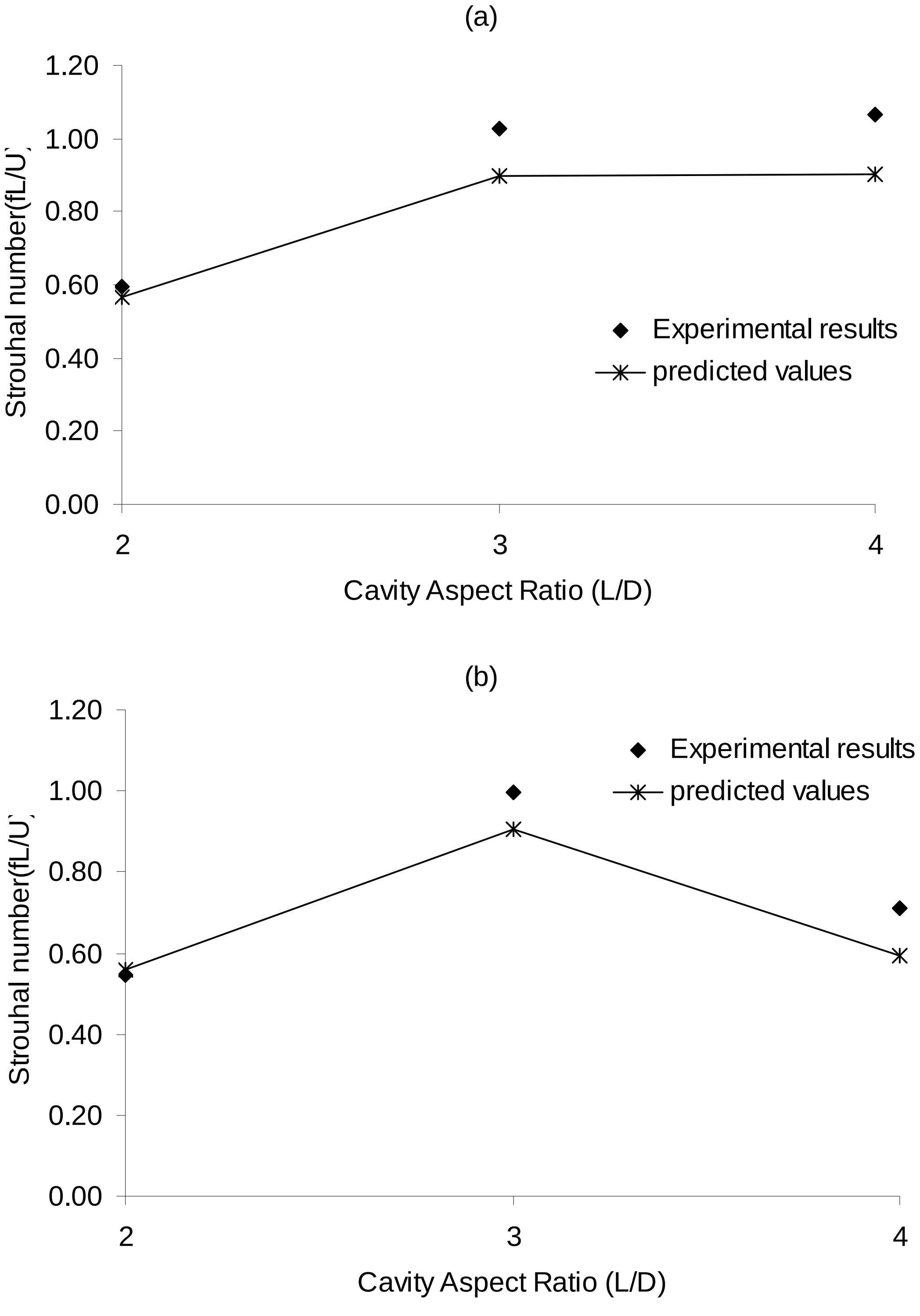

Figure 59(i). Comparison with modified Rossiter predicted values at (a)35 psi, (b)55 psi.

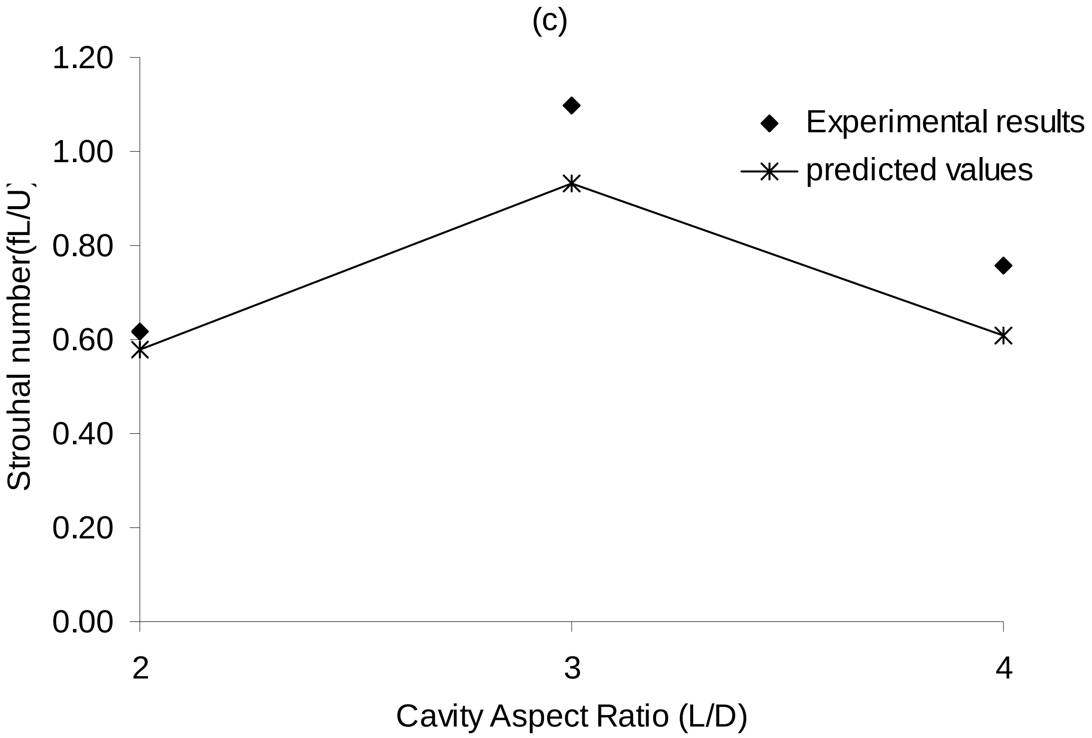

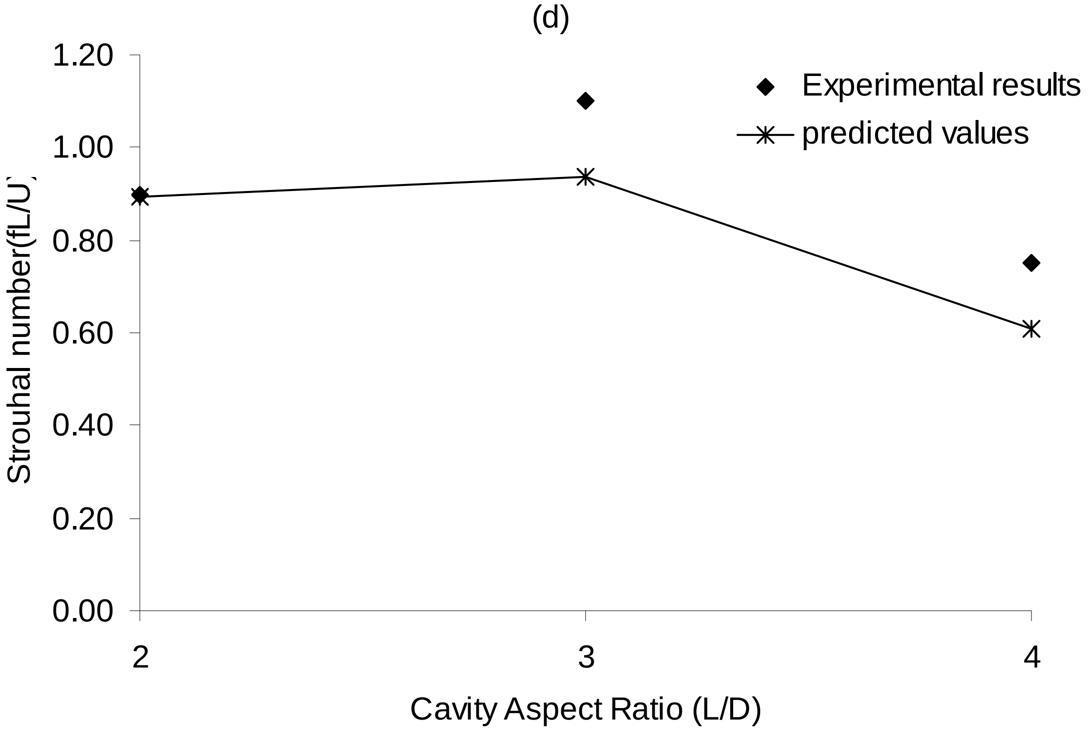

Figure 55(ii). Comparison with modified Rossiter predicted values at (c)75 psi, (d)95 psi.

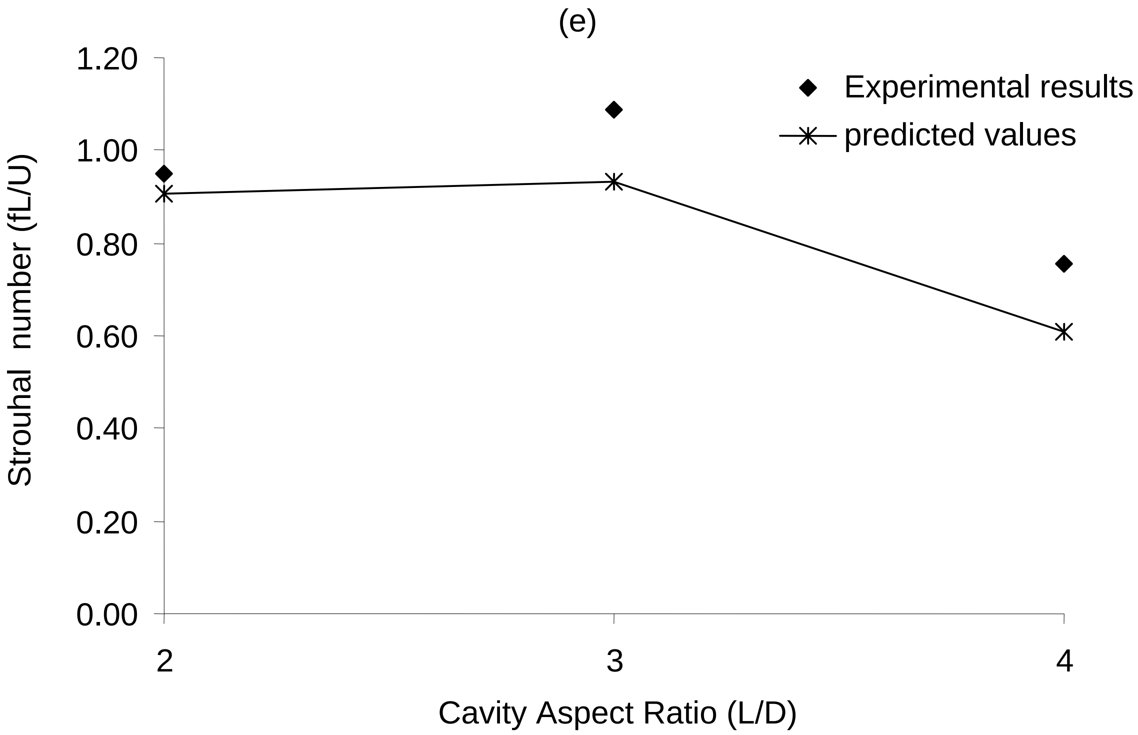

Figure 55(iii). Comparison with modified Rossiter predicted values at (e)120 psi.

7. References

[1] Ben-Yakar, A., and Hanson, R.K., “Cavity Flameholders for Ignition and Flame Stabilization in Scramjets - Review and Experimental Study,” AIAA Paper 98-3122, July 1998.

[2] Ben-Yakar, A., and Hanson, R.K., “Cavity Flame-Holders for Ignition and Flame Stabilization in Scramjets: An Overview,” *Journal of Propulsion and Power*, Vol. 17, No. 4, 2001.

[3] Bogdanoff, D.W., “Advanced Injection and Mixing Techniques for Scramjet Combustors,” *Journal of Propulsion and Power*, Vol. 10, No. 2, 1994.

[4] Brown, G.L., and Roshko, A., “On Density Effects and Large Structure in Turbulent Mixing Layers,” *Journal of Fluid Mechanics*, Vol. 64, Pt. 4, 1974, pp. 775–816.

[5] Brown, G.L., “The Entrainment and Large Structure in Turbulent Mixing Layers,” *Fifth Australian Conference on Hydraulics and Fluid Mechanics,* 1974, pp. 352-359.

[6] Burnes, R., Wilson, K.J., Parr, T.P., and Yu, K., "Investigation of Supersonic Mixing Control Using Cavities: Effect of Fuel Injection Location," AIAA Paper 2000-3618, July 2000.

[7] Cattafesta III, L. N., Garg, S., Kegerise, M.A., and Jones, G.S., “Experiments on Compressible Flow-Induced cavity Oscillations,” AIAA-98-2912, June 1998.

[8] Curran, E.T., Heiser, W.H., and Pratt, D.T., “Fluid Phenomena in Scramjet Combustion Systems”, *Annual Review of Fluid Mechanics,* Vol. 28, 1996, pp.323-360.

[9] Curran, E.T., “Scramjet Engines: The First Forty Years,” *Journal of Propulsion and Power*, Vol. 17, No.6, Nov-Dec 2001, pp. 1138-1148.

[10] Coats, C.M., “Coherent Structures in Combustion,” *Progress in Energy and Combustion Sciences*, Vol. 22, 1996, pp. 427-509.

[11] Dimotakis, P.E., “Two-Dimensional Shear-Layer Entrainment,” *AIAA Journal*, Vol. 24, No. 11, 1986, pp. 1791-1796.

[12] Dimotakis, P.E., “Turbulent Free Shear Layer Mixing and Combustion,” *High Speed Flight Propulsion Systems*, edited by Murthy, S.N.B., and Curran, E.T., Progress in Astronautics and Aeronautics Series, Vol. 137, AIAA, Washington, DC, 1991, pp. 265–340.

[13] Dimotakis, P.E., “The Mixing Transition in Turbulent Flows,” *Journal of Fluid Mechanics,* Vol. 9, 2000, pp. 69-98.

[14] Dimotakis, P.E., “Recent Advances in Turbulent Mixing,” Caltech ASCI technical Report 065, September 2000.

[15] Drummond, P.J., Carpenter, M.H., and Riggins, D.W., “Mixing and Mixing Enhancement in Supersonic Reacting Flowfields,” *High Speed Flight Propulsion Systems*, edited by Murthy, S.N.B., and Curran, E.T., Progress in Astronautics and Aeronautics Series, Vol. 137, AIAA, Washington, DC, 1991, pp. 383–455.

[16] Drummond, P.J., Diskin, G.S. and Cutler, A.D., “Fuel-Air Mixing and Combustion in Scramjets,” AIAA Paper 2002-3878, July 2002.

[17] Fernando, E.M., and Menon, S., “Mixing Enhancement in Compressible Mixing Layers: An Experimental Study,” *AIAA Journal*, Vol. 31, No. 2, February 1993.

[18] Ferri, A., "Review of Problems in Application of Supersonic Combustion," *Journal of The Royal Aeronautical Society*, Vol. 68, Sep. 1964, P. 575-597.

[19] Ferri, A., "Mixing-Controlled Supersonic Combustion," *Annual Review of Fluid Mechanics*, Vol. 5, 1973, pp. 301-338.

[20] Gruber, M.R., Baurle, R.A., Mathur, T., and Hsu, K.Y., "Fundamental Studies of Cavity-Based Flameholder Concepts for Supersonic Combustors," *Journal of Propulsion & Power*, Vol. **17**, No. 1, 2001, pp. 146-153.

[21] Gutmark, E.J., Schadow, K.C., and Wilson, K.J., "Effect of Convective Mach Number on Mixing of Coaxial Circular and Rectangular Jets," *Physics of Fluids A*, Vol. 3, No. 1, 1991, pp. 29-36.

[22] Gutmark, E.J., Schadow, K.C. and Yu, K.H., "Mixing Enhancement in Supersonic Free Shear Flows," *Annual Review of Fluid Mechanics*, Vol. 27, 1995, pp.375-417.

[23] Heiser, W.H., Pratt, D.T. et al., *Hypersonic Airbreathing Propulsion*, AIAA Education series, AIAA, 1994.

[24] Heller, H.H., and Bliss, D.B., "Physical Mechanism of Flow-Induced Pressure Fluctuations in Cavities and Concepts for Their Suppression", AIAA Paper 75-491, 1975.

[25] Kegerise, M.A., "An Experimental Investigation of Flow-Induced Cavity Oscillations", PhD Dissertation, Syracuse University, 1999.

[26] Mathur, T., and Billig, F., "Supersonic Combustion Experiments with a Cavity-Based Fuel Injector," *Journal of Propulsion and Power*, Vol. 17, No. 6, 2001.

[27] Murray, R.C., and Elliott, G.S., "Characteristics of the Compressible Shear Layer Over a Cavity", *AIAA Journal*, Vol. 39, No.5, May 2000, pp. 846-856.

[28] Murthy, S.N.B., and Curran, E.T., *Scramjet Propulsion*, American Institute of Aeronautics and Astronautics, Reston, VA, 2000.

[29] Nenmeni, V.A., and Yu, K.H., “Cavity-Induced Mixing Enhancement in Confined Supersonic Flows,” AIAA Paper 2002-1010, January 2002.

[30] Papamouschou, D., “Structure of the Compressible Turbulent Shear Layer,” *AIAA Journal*, Vol. 29, No. 5, May 1991, pp. 680-681.

[31] Rockwell, D., and Naudascher, E., “Review-Self-Sustaining Oscillations of Flow Past Cavities,” *Journal of Fluids Engineering*, Vol. 100, June 1978, pp. 152-165.

[32] Papamouschou, D., and Roshko, A., “The Compressible Turbulent Shear Layer: An Experimental Study,” *Journal of Fluid Mechanics*, Vol. 197, 1988, pp. 453–477.

[33] Rossiter, J.E., “Wind Tunnel Experiments on the Flow Over Rectangular Cavities at Subsonic and Transonic Speeds,” *British Aeronautical Research Council*, Reports and Memoranda 3488, London, Oct 1964.

[34] Rossman, T., “An Experimental Investigation of High Compressibility Mixing Layers,” PhD Dissertation, Stanford University, Stanford, December 2001.

[35] Schlichting, H., *Boundary Layer Theory*, McGraw-Hill Inc., 1979.

[36] Seiner, J.M., Dash, S.M., and Kenzakowski, D.C., “Historical Survey on Enhanced Mixing in Scramjet Engines,” *Journal of Propulsion and Power*, Vol. 17, No. 6, 2001, pp. 1273-1286.

[37] Settles, G.S., *Schlieren and shadowgraph techniques - Visualizing phenomena in transparent media*, Springer, 2001.

[38] Shapiro, A.H., *The Dynamics and Thermodynamics of Compressible Fluid Flow, Volume I,* The Ronald Press Company, NY, 1953.

[39] Slessor, M.D., Bond, C.L., and Dimotakis, P.E., "Turbulent Shear-Layer Mixing at High Reynolds Numbers: Effects of Inflow Conditions," *Journal of Fluid Mechanics*, Vol. 376, 1998, pp. 115-138.

[40] Strykowski, P.J., and Krothapalli, A., "The Countercurrent Mixing Layers: Strategies for Shear-Layer Control," AIAA Paper 93-3260, 1993.

[41] Swithenbank, J., Eames, I.W., Chin, S.B., Ewan, B.C.R., Yang, Z., Cao, J., and Zhao, X., "Turbulent Mixing in Supersonic Combustion Systems", *High-Speed Flight Propulsion Systems*, edited by Murthy, S.N.B, and Curran, E.T., Vol. 137, Progress in Astronautics and Aeronautics, AIAA, Washington, DC, 1991, pp. 341-381.

[42] Tischkoff, J.M., Drummond, J.P., Edwards, T., and Nejad, A.S., "Future Directions of Supersonic Combustion Research: Air Force/NASA Workshop on Supersonic Combustion," AIAA Paper 97-1017, January 1997.

[43] Tracy, M.B., and Plentovich, E.B., "Cavity Unsteady-Pressure Measurements at Subsonic and Transonic Speeds," NASA Technical Paper 3669, NASA Langley Research Center, Hampton, Va, December 1997.

[44] Vuillermoz, P., and Oran, E.S., "Mixing Regimes in a Spatially Confined Two-Dimensional Compressible Mixing Layer," *Proceedings of the Royal Society of London A*, Vol. 449, 1995, pp. 351-380.

[45] Wu, Y., and Fu, S., "Detection of Velocity Distribution of a Flow Field Using Sequences of Schlieren Images," *Optical Engineering,* Vol. 40, No. 8, August 2001, pp. 1661-1666.

[46] Yu, G., Li, J.G., Chang, X.Y., Chen, L.H., and Sung, C.J., “Investigation of Kerosene Combustion Characteristics with Pilot Hydrogen in Model Supersonic Combustors,” *Journal of Propulsion & Power*, Vol. 17, No. 6, 2001, pp. 1259-1263.

[47] Yu, K.H., Kraeutle K.H., Wilson, K.J., Parr, T.P., Smith, R.A., et al., “Supersonic Flow Mixing and Combustion using Ramp Nozzle”, AIAA Paper 92-3840, 1992.

[48] Yu, K.H., Parr, T.P., and Schadow, S.C., “Planar Mie Scattering Visualization of Reacting and Non-Reacting Supersonic Coaxial Jets,” *Third International Symposium on Special Topics in Chemical Propulsion*, Session R-8, Paper No. 1, May 10-14, 1993.

[49] Yu, K.H., Gutmark, E.J., Smith, R.A., and Schadow, K.C., “Supersonic Jet Excitation using cavity-actuated Forcing,” AIAA Paper 94-0185, 1994.

[50] Yu, K.H., Wilson, K.J., and Schadow, K.C., “Effect of Flame-Holding Cavities on Supersonic Combustion Performance,” *Journal of Propulsion & Power*, Vol. 17, No. 6, 2001, pp. 1287-1295.

[51] Yu, K.H. and Schadow, K.C., "Role of Large Coherent Structures in Turbulent Compressible Mixing," *Experimental Thermal and Fluid Science*, Vol. 14, 1997, pp. 75-84.

[52] Yu, K.H., “Lectures on: Special Problems on Ramjets, Scramjets, PDEs and Their Control,” ENAE 661, Advanced Propulsion-I, University of Maryland.

[53] Zhang, X., and Edwards, J.A., “An Investigation of Supersonic Oscillatory Cavity Flows Driven by Thick Shear Layers,” *Aeronautical Journal*, December 1990, pp. 355-364.

[54] Zhang, X., “Compressible Cavity Flow Oscillation Due to Shear Layer Instabilities and Pressure Feedback,” *AIAA Journal*, Vol. 33, No. 8, August 1995.